Electron Counting Statistics of Open Quantum Systems

Richard Stones

A dissertation submitted in partial fulfillment

of the requirements for the degree of

Doctor of Philosophy

of

University College London.

Department of Physics and Astronomy

University College London

April 6, 2018

I, Richard Stones, confirm that the work presented in this thesis is my own. Where information has been derived from other sources, I confirm that this has been indicated in the work.

Abstract

Electron transport through organic molecules is a process fundamental to life and plays a central role in the emerging field of molecular electronics. This thesis presents an investigation of electron transport through molecular systems from the perspective of full counting statistics. An extension of a Markovian counting statistics framework to a non-perturbative setting is presented which allows for an exact treatment of the phonon bath. This framework is applied to a theoretical photocell device inspired by the photosystem II reaction centre. It is demonstrated that the asymmetric coupling of excitation and charge transfer states to a structured spectral density rather than a smooth low energy background has the effect of reducing the output current along with an associated reduction in the current fluctuations. The insights gained from this are discussed in terms of design principles for pigment-protein complexes used in nano-electronic devices and their relevance for biological function *in vivo*. Finally, the asymmetric coupling of excitation and charge transfer states to their vibrational environment is investigated more closely through the dynamics of a dimer model and the effect of the output current statistics of a prototype photocell.

Impact Statement

The contents of this thesis have the potential to be of beneficial use in areas both inside and outside of academia.

The immediate impact of the results in this thesis will be inside academia. The novel non-perturbative method for electron counting statistics presented in Chapter 3 will be applicable to studying electron transport through molecular junctions and solid-state nano-electronic devices, as well as for gaining new insights into photosynthetic electron transport processes. The proposal of applying counting statistics methods to photosynthetic electron transfer in Chapter 4 may inspire new experiments on bio-molecular electron transfer systems that complement spectroscopy, and lead to a more complete picture of the role quantum effects have in photosynthesis in particular. Finally, a deeper understanding of electron transfer in photosynthetic reaction centres based on the study in Chapter 5 could stimulate the construction of novel artificial photovoltaic devices based on design principles found in Nature. The impact will be brought about by disseminating the work in academic journals.

Over the long term, the design of more efficient photovoltaic devices could have a huge impact on our ability to generate clean electricity and therefore greatly impact the state of the climate and environment. Furthermore, a better understanding of electron transport through nano-scale systems may lead to the commercial development of novel electronics that could make its way into a range of devices. The contribution of this thesis towards these goals is very much incremental and will require a large amount of further work to develop the ideas put forward here.

Public outreach projects, in part based on the work in this thesis, have also had

an impact in raising the idea of interdisciplinarity within the sciences among school children and adults. In the future, problems in the traditional fields of physics, chemistry and biology will overlap more and more with each other and it is important that the next generation of scientists understand the importance of gaining some understanding of all these areas. The application of quantum physics to biological systems was a particularly interesting topic to engage the general public for maximum impact.

Acknowledgements

Firstly I'd like to thank my supervisor Alexandra for all her help over the last five years. I'd also like to thank the other members of the research group that I have worked with: Francesca Fassioli, Edward O'Reilly, Hoda Hossein-Nejad, David Holdaway, Valentina Notararigo, Guiseppe Argentieri and Stefan Siwiak-Jaszek. They have all contributed to this thesis in some way. Finally I want to thank my family and friends that had to put up with me during the long process of writing this thesis. In particular, I need to thank my parents who encouraged my interest in science from an early age. When I was a child my dream was to become a mad scientist so I'd to think my ten year old self is happy with what I've achieved so far!

Contents

List of Figures

List of Tables

Chapter 1

Introduction

Photosynthesis is the solar energy conversion process found in plants, algae and certain bacteria [1]. It begins with the capture of energy from sunlight by light-harvesting antennae proteins. These antennae transport the energy on ultra-fast time scales to a specialised pigment-protein complex called the reaction centre where a charge separation event is initiated. Here the energy is converted to an electrochemical form and stored across a membrane in a similar way to a battery. This stored energy is then used to synthesise ATP and ultimately create food for the organism [1].

These photosynthetic energy and charge transfer processes are of interest to physicists for several reasons. Primarily, the observation of population oscillations in the 2D electronic spectra of light-harvesting antennae [2, 3, 4, 5, 6] and the photosystem II reaction centre [7, 8] indicates the influence of quantum mechanical effects on energy transfer and primary charge separation. Since these processes occur at physiological temperatures and in contact with a noisy environment it is surprising that quantum coherence lasts long enough to have any effect on the electronic dynamics. Thus far, research has mostly focused on energy transfer and the possible vibrational contribution to the long lasting electronic coherences [9, 10, 11, 12, 13, 14]. Although there have been some experimental studies on photosynthetic reaction centres demonstrating similar vibrational influence on electron transport [7, 8], the zero oscillator strength of charge transfer states in the reaction centre makes it difficult to study charge separation in the same way [7]. Charge

transfer states have different properties to excited states [15] so the insight gained from the study of light-harvesting antennae does not necessarily carry over. One of the goals of this research is to achieve a deeper understanding of these pigment-protein complexes in order to inspire the design of artificial photovoltaic devices built on similar principles [16, 17, 18, 19].

Beyond spectroscopy, it is also possible to measure the electron conduction and photocurrent through photosynthetic proteins by incorporating them into electric circuits. The current through immobilised layers of photosystem I [20], photosystem II [21, 22, 23] and bacterial reaction centres [24] has been measured experimentally. More interesting however are measurements of the photocurrent through individual photosystem I [25, 26] and photosystem II [27] units which may open up new possibilities to study the electronic dynamics of charge separation in photosynthesis.

Moving slightly away from biological systems, there is also great interest in gaining a deeper understanding of molecular electron transport for the design of novel nanoscale electronic devices [28, 29] such as diodes, switches and transistors. Molecular junctions can exhibit a much richer behaviour than similar semiconductor based devices in part due to the strong interaction between electronic and vibrational components of the molecules [28].

Having access to the current through an individual reaction centre or a molecular junction could allow for measurement of the current fluctuations and higher order moments of the current at a single system level. The moments contain dynamical information about the electron transfer and crucially, don't depend on the ability of charge transfer states to interact with light. The theory of full counting statistics [30, 31, 32, 33] provides a framework with which to generate these moments of the current. It was originally developed in the optics community for photon counting [34] but was later applied to electron transfer through mesoscopic condensed matter systems such as quantum dots [32] and nano-electromechanical systems [35]. The theory has already been applied to electron transfer through molecular junctions in the presence of a discrete vibrational mode [36, 37, 38] but not yet to charge transfer

through photosynthetic reaction centres. Generating the full counting statistics in this latter case involves certain challenges related to the vibrational environments found in biomolecular systems. The vibrational degrees of freedom often contain many discrete modes which may be non-Markovian in nature and strongly coupled to the electronic dynamics. Since the counting statistics of electron transport was first applied to solid state mesoscopic systems, the present theories may not be suitable for application to these vibrational environments.

The work in this thesis will attempt to address this issue and hopefully take a step towards a deeper understanding of the effect of the vibrational interactions on charge separation in organic molecules, in particular in the photosystem II reaction centre.

The rest of this thesis is arranged as follows. Chapter 2 provides an overview of the theoretical tools used to carry out the research presented later on. We discuss the theory of open quantum systems with regard to both perturbative and non-perturbative approaches. In particular, the theories used for calculations are presented in more detail along with a discussion of their respective limitations. The theory of Markovian electron counting statistics is also outlined. We show the approximations used in arriving at a typical counting statistics setup consisting of a system weakly connected to leads.

The signatures of quantum coherence displayed in the current fluctuations for a simple toy model are presented in Chapter 3. We follow this with the development of a non-perturbative method of electron counting statistics. We demonstrate the application of this method using a molecular dimer system and comparing the results to a perturbative approach. Some features of the effect of vibrational dynamics on the current statistics are then examined.

Further application of this non-perturbative method is shown in Chapter 4. We develop a photocell model based on the photosystem II reaction centre and compare the non-perturbative method to a Markovian treatment of the counting statistics. Characterisation of the output current from the perspective of both the mean and fluctuations is used to investigate the effect of different vibrational environments on

photocell performance.

Chapter 5 focuses on the increased reorganisation energy of charge transfer states relative to excitation states. Firstly, the effect of this asymmetry is investigated for the dynamics of a dimer model with parameter regimes of two different charge separation pathways in the photosystem II reaction centre. Then the performance of a photocell model incorporating this reorganisation energy asymmetry is investigated in terms of the output current statistics.

Chapter 2

Theory of Counting Statistics in Open Quantum Systems

The theoretical tools necessary for a full appreciation of the research presented in this thesis are outlined below. The systems of interest are organic molecules such as photosynthetic pigment-protein complexes which undergo excited state energy and charge transfer dynamics. Generally the aim is to obtain equations describing the dynamics of the electronic degrees of freedom under the influence of a vibrational environment. For electron counting statistics, a description of the coupling of electronic degrees of freedom to fermionic reservoirs is also required. Firstly the theory of open quantum systems is outlined concentrating on the various approximations used in later chapters. In particular, the second order Born-Markov master equation and the hierarchical equations of motion are discussed. The theory of electron counting statistics is then derived from a Markovian master equation which sets the scene for an extension of this framework into a non-perturbative setting in the next chapter.

2.1 Open Quantum Systems Approaches

In the quantum mechanical description of molecular charge and energy transfer processes there are too many degrees of freedom involved to carry out an exact calculation of the full system dynamics. Open quantum systems approaches are useful for these types of problems as they allow us to approximate the effect of

many environmental degrees of freedom on the dynamics of a relevant system of interest [39]. Typically we partition the total system so the Hamiltonian can be written

$$H = H_S + H_B + H_{SB} \tag{2.1}$$

where H_S is the isolated system Hamiltonian, H_B is the Hamiltonian of the isolated environment or 'bath' and H_{SB} describes the interaction between the two. The interaction between the system and environment allows energy exchange as well as the emergence of correlations between the sub-systems. Consequently, the reduced system dynamics becomes dissipative and is no longer fully coherent. For a general quantum system with the Hamiltonian given in Eq. (2.1) the Liouville-von Neumann equation for the total system density matrix $W(t)$ in the Schrödinger picture is

$$\dot{W}(t) = -i[H, W(t)] \tag{2.2}$$

In order to obtain an equation of motion for the reduced density matrix $\rho(t) = \mathrm{tr}_B\{W(t)\}$, we can follow various schemes utilising different approximations depending on the parameters of the system under study. The resulting equations fall broadly into two categories: (i) Markovian: memory-less environment which relaxes on time scales much faster than characteristic system time scales. The perturbatively derived Lindblad [39] equation uses a Markovian bath approximation. (ii) Non-Markovian: memory effects come into play such that the system dynamics depends on the past state of the bath. Generalised master equations [39] derived in a perturbative way fall into this category as well as non-perturbative theories such as the hierarchical equations of motion [40, 41] and TEDOPA [42].

In the following the fundamental constant $\hbar$ will be set equal to 1 to simplify the notation.

2.1.1 Description of Electronic and Vibrational Degrees of Freedom

In bio-molecular systems, the electronic degrees of freedom interact with nuclear motions of the molecules themselves as well as those of the surrounding protein

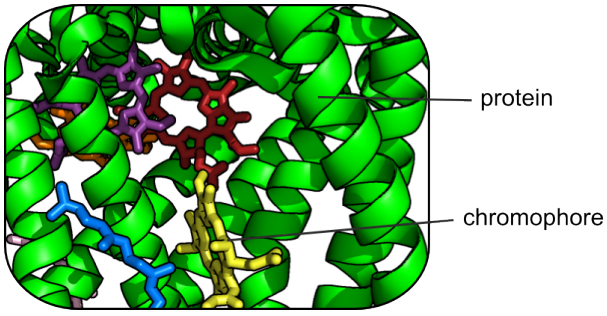

Figure 2.1: Photosynthetic pigment-protein complex. Protein alpha helices are shown in green while chromophores (pigments) are coloured differently.

or solvent environments [43]. The intra-molecular motions can have a particularly strong influence on the electronic system since their energies are often larger than the thermal energy such that we require a full quantum mechanical description to properly capture their behaviour. They can also be on resonance with electronic energy gaps which enhances coherent energy exchange between the electronic and vibrational degrees of freedom. A photosynthetic pigment-protein complex is presented in Fig. 2.1 showing chromophores held in a specific arrangement by the surrounding protein.

We will generally be interested in the movement of electronic energy and charge density through bio-molecular systems. It therefore makes sense to concentrate on the electronic degrees of freedom as our system of interest in an open quantum systems framework. We can describe these systems in the single excited state manifold using the Hamiltonian

$$H_S = \sum_i \varepsilon_i |i\rangle\langle i| + \sum_{i \neq j} J_{ij}(|i\rangle\langle j| + |j\rangle\langle i|) \tag{2.3}$$

where the state $|i\rangle$ represents a localised state of the system, either a single excited state of a chromophore or a charge transfer state. ε_i is the energy of state $|i\rangle$ while J_{ij} is the coupling between states $|i\rangle$ and $|j\rangle$. Coupling between excitation states originates from dipole-dipole interactions while coupling between excited states and charge transfer states depends on wavefunction overlap [15]. The ground state of the system at zero energy is implicitly included in the Hamiltonian above. Ex-

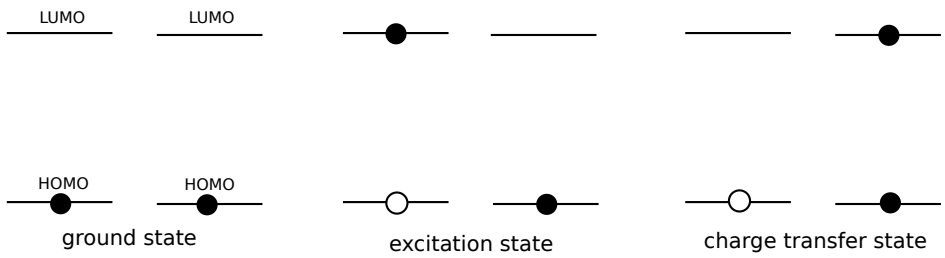

Figure 2.2: Representation of ground, excited and charge transfer states in terms of occupation of the HOMO and LUMO for neighbouring chromophores. The type of state depends on the occupation of the highest occupied molecular orbital (HOMO) in the ground state configuration and the lowest unoccupied molecular orbital (LUMO) for neighbouring chromophores shown here as two level systems. Electrons are represented by solid circles and holes by empty circles.

cited states are formed by the transition of an electron from the highest occupied molecular orbital (HOMO) to the lowest unoccupied molecular orbital (LUMO) of the chromophore. In this case the electron and hole are localised on the same chromophore. Charge transfer states involve a separation of the electron and hole across different chromophores. This is represented schematically in Fig. 2.2. We will not explicitly model the various possible configurations of electrons and holes on each chromophore for the ground, excited and charge transfer states. This type of modelling has previously been applied to photosystem II reaction centre models [44, 45] but increases the size of the state space of the system and adds complexity to the problem. Instead we will treat the charge transfer states as localised electronic states as in Refs. [46, 47]. This type of model has successfully been used to reproduce experimental spectra.

We will treat the nuclear motions as the degrees of freedom of our bath. In order to understand their effect on the electronic system, we first need to construct a description of these vibrations. We consider a bosonic bath formed of independent normal modes [43] with the Hamiltonian

$$H_B = \sum_q \omega_q \left(b_q^\dagger b_q + \frac{1}{2} \right) \tag{2.4}$$

Using a general form of the interaction Hamiltonian $H_{SB} = \sum_j V_j \otimes B_j$, we can com-

pletely describe the influence on the electronic system using a correlation function of the bath coupling operators $C_{jj}(t) = \langle B_j(t)B_j(0)\rangle_B = tr_B\{B_j(t)B_j(0)B_0\}$ where B_0 is a reference state of the bath. Notice that we have used the auto-correlation function $C_{jj}(t)$ since only independent, uncorrelated baths coupled to localised electronic sites will be considered throughout the rest of this thesis. The subscripts on the correlation function will also be dropped to simplify the notation. For a bosonic bath the interaction takes the form $B = \sum_q g_q(b_q^\dagger + b_q)$ [43] such that the correlation function can be expressed

$$\begin{aligned} C(t) =& \sum_q g_q^2[(1+n_q(\omega))e^{-i\omega_q t} + n_q(\omega)e^{i\omega_q t}] \\ =& \frac{1}{\pi}\int_0^\infty d\omega J(\omega)[\coth\frac{\beta\omega}{2}\cos\omega t - i\sin\omega t] \end{aligned} \tag{2.5}$$

where $n(\omega) = (e^{\beta\omega}-1)^{-1}$ is the Planck distribution for inverse temperature $\beta = \frac{1}{k_B T}$. The function $J(\omega)$ is known as the spectral density, which quantifies the coupling strength of the bath frequency continuum to the electronic system. It has the general form

$$J(\omega) = \pi\sum_q g_q^2\delta(\omega-\omega_q) \tag{2.6}$$

Typically in bio-molecular systems such as photosynthetic pigment-protein complexes the effect of the vibrational environment is well described by combinations of Brownian oscillator spectral densities

$$J_D(\omega) = \frac{2\lambda_D\Omega_D\omega}{\omega^2+\Omega_D^2}, \tag{2.7}$$

$$J_q(\omega) = \frac{2\lambda_q\omega_q^2\gamma_q\omega}{(\omega^2-\omega_q^2)^2+\gamma_q^2\omega^2} \tag{2.8}$$

The Drude spectral density $J_D(\omega)$ describes a low frequency phonon bath having reorganisation energy λ_D and cutoff frequency Ω_D, in general originating from interactions with slow protein motions and the solvent environment [48]. $J_q(\omega)$ describes interaction with a discrete vibrational mode q with frequency ω_q, reorganisation energy λ_q and damping constant γ_q. Usually the full spectral density will be

a summation of several components $J(\omega) = J_D(\omega) + \sum_q J_q(\omega)$.

A useful property of these spectral densities is they can be decomposed into sums of exponential functions [49]. For the Drude spectral density in Eq. (2.7) the correlation function can be expanded as

$$C_D(t) = c_D^{(0)} e^{-\Omega_D t} + \sum_{k=1}^{\infty} c_D^{(k)} e^{-\nu_k t}, \tag{2.9}$$

where $c_D^{(0)} = \Omega_D \lambda_D (\cot(\frac{\beta\Omega_D}{2}) - i)$, $c_D^{(0)} = \frac{4\lambda_D \Omega_D}{\beta} \frac{\nu_k}{\nu_k^2 - \Omega_D^2}$ and the Matsubara frequencies $\nu_k = \frac{2\pi k}{\beta}$. For the underdamped Brownian oscillator in Eq. (2.8) the correlation function expansion is

$$C_q(t) = c_q^+ e^{-\nu_q^+ t} + c_q^- e^{-\nu_q^- t} + \sum_{k=1}^{\infty} c_q^{(k)} e^{-\nu_k t}, \tag{2.10}$$

where $c_q^{\pm} = \pm i \frac{\lambda_q \omega_q^2}{2\zeta_q} (\cot(\frac{\nu_q^{\pm}\beta}{2}) - i)$, $c_q^{(k)} = -\frac{4\lambda_q \gamma_q \omega_q^2}{\beta} \frac{\nu_k}{(\omega_q^2 + \nu_k^2)^2 - \gamma_q^2 \nu_k^2}$, $\nu_q^{\pm} = \frac{\gamma_q}{2} \pm i\zeta_q$ and $\zeta_q = \sqrt{\omega_q^2 - \frac{\gamma_q^2}{4}}$.

A further property of the bath is the reorganisation energy $\lambda = \frac{1}{\pi} \int_0^{\infty} d\omega J(\omega)/\omega$ which quantifies the total strength of the system-bath interaction [46].

2.1.2 Perturbative Master Equations

2.1.2.1 The Lindblad Equation

By partitioning the Hamiltonian such that system-bath interaction H_{SB} acts as a perturbation to the free Hamiltonian $H_0 = H_S + H_B$, Eq. (2.2) can be transformed into the interaction picture. This picture adds an implicit time evolution due to H_0 on operators O such that $\tilde{O} = e^{iH_0 t} O e^{-iH_0 t}$. This puts the focus on the dynamics due to H_{SB}. The interaction picture Liouville-von Neumann equation is

$$\dot{\tilde{W}}(t) = -i[\tilde{H}_{SB}(t), \tilde{W}(t)] \tag{2.11}$$

Formal integration and substitution back into the original equation of motion gives

$$\dot{\tilde{W}}(t) = -i[\tilde{H}_{SB}(t), W(0)] - \int_0^t dt' [\tilde{H}_{SB}(t), [\tilde{H}_{SB}(t'), \tilde{W}(t')]] \tag{2.12}$$

which is still exact but now in a form which lends itself to various approximations such that it can be simplified into a tractable expression. Tracing over the bath degrees of freedom to obtain the reduced density matrix $\rho(t)$ gives

$$\dot{\tilde{W}}(t) = -i\mathrm{tr}_B\Big\{[\tilde{H}_{SB}(t), W(0)]\Big\} - \int_0^t dt' \mathrm{tr}_B\Big\{[\tilde{H}_{SB}(t), [\tilde{H}_{SB}(t'), \tilde{W}(t')]]\Big\} \tag{2.13}$$

The first term can always be made to equal zero through a redefinition of the system Hamiltonian leaving

$$\dot{\tilde{W}}(t) = -\int_0^t dt' \mathrm{tr}_B\Big\{[\tilde{H}_{SB}(t), [\tilde{H}_{SB}(t'), \tilde{W}(t')]]\Big\} \tag{2.14}$$

Assuming the interaction between the system and the bath to be weak and that the bath is very large such that its state is essentially unaffected by coupling to the system, we can make the *Born approximation* [39]. This involves splitting the total density matrix into the system density matrix and a reference state of the bath $W(t) = \rho(t) \otimes B_0$, and assuming this is valid for all times. This amounts to neglecting all potential system-bath correlations. The equation of motion is now

$$\dot{\tilde{W}}(t) = -\int_0^t dt' \mathrm{tr}_B\Big\{[\tilde{H}_{SB}(t), [\tilde{H}_{SB}(t'), \tilde{\rho}(t') \otimes B_0]]\Big\} \tag{2.15}$$

At this point an explicit expression for the system-bath interaction is required. This may take various forms depending on the statistics of the bath and the nature of its interaction with the system. For now we use a general form $\tilde{H}_{SB}(t) = \sum_i \tilde{V}_i(t) \otimes \tilde{B}_i(t)$ where the operators V_i act on the system and B_i act on the bath. Inserting this into Eq. (2.15) and rearranging gives

$$\begin{aligned}\dot{\tilde{\rho}}(t) = \; & - \sum_{ij} \int_0^t dt' \Big[\langle \tilde{B}_i(t)\tilde{B}_j(t')\rangle_B \Big(\tilde{V}_i(t)\tilde{V}_j(t')\tilde{\rho}(t') - \tilde{V}_j(t')\tilde{\rho}(t')\tilde{V}_i(t)\Big) \\ & + \langle \tilde{B}_j(t')\tilde{B}_i(t)\rangle_B \Big(\tilde{\rho}(t')\tilde{V}_j(t')\tilde{V}_i(t) - \tilde{V}_i(t)\tilde{\rho}(t')\tilde{V}_j(t')\Big)\Big]\end{aligned} \tag{2.16}$$

If the bath can be assumed to relax on time scales much faster than characteristic time scales of the system, the *Markov approximation* can be applied [39]. This

means $\langle \tilde{B}_j(t)\tilde{B}_j(t')\rangle_B \propto \delta(t-t')$ as well ensuring that the future dynamics of the system density matrix depends only on the current state of the system rather than past states. This justifies the substitution $\rho(t') \to \rho(t)$ in Eq. (2.16). The most general form of the second order master equation in the Born-Markov approximation is then

$$\begin{aligned}\dot{\tilde{\rho}}(t) = \; & - \sum_{ij} \int_0^t dt' \Big[\langle \tilde{B}_i(t)\tilde{B}_j(t')\rangle_B \Big(\tilde{V}_i(t)\tilde{V}_j(t')\tilde{\rho}(t) - \tilde{V}_j(t')\tilde{\rho}(t)\tilde{V}_i(t) \Big) \\ & + \langle \tilde{B}_j(t')\tilde{B}_i(t)\rangle_B \Big(\tilde{\rho}(t)\tilde{V}_j(t')\tilde{V}_i(t) - \tilde{V}_i(t)\tilde{\rho}(t)\tilde{V}_j(t') \Big) \Big] \end{aligned} \tag{2.17}$$

The exact form of the correlation functions depends on the nature of the bath (see Section 2.1.1).

The second order Born-Markov master equation can be expressed in the Lindblad form by making the secular approximation [39], which guarantees positive definite time evolution of the system density matrix. In the Schrödinger picture this equation is

$$\dot{\rho}(t) = -i\Big[H_S, \rho(t)\Big] + \mathcal{D}[\rho(t)] \tag{2.18}$$

where the dissipator $\mathcal{D}[\rho(t)]$ has the form

$$\mathcal{D}[\rho(t)] = \sum_j \Gamma_j \Big[A_j \rho(t) A_j^\dagger - \frac{1}{2} A_j^\dagger A_j \rho(t) - \frac{1}{2} \rho(t) A_j^\dagger A_j \Big] \tag{2.19}$$

The rates Γ_j are associated with the Lindblad operators A_j which describe transitions between quantised states of the system mediated by the environment.

2.1.2.2 Modified Redfield Theory

In deriving the Lindblad equation, the whole system-bath interaction Hamiltonian is treated as a perturbation which restricts the range of validity to the case of weak system-bath coupling relative to the inter-site couplings J_{ij}. A variation on this called Modified Redfield Theory (MRT) [50, 51] treats only the off-diagonal elements of the interaction Hamiltonian in the system eigenstate basis as the perturbation, making it applicable for a wider range of system-bath coupling strengths in

certain parameter regimes. Diagonalising the system Hamiltonian in Eq. (2.3) gives the Hamiltonian in the electronic eigenstate basis $H_S = \sum_a E_a|a\rangle\langle a|$ where the states $|a\rangle$ represent delocalised excitation and charge transfer states which we will call excitons. MRT describes population-to-population transfer among these excitons taking into account strong coupling to the phonon bath. The perturbation Hamiltonian is $H' = \sum_{a\neq b} H_{SB}^{(ab)}|a\rangle\langle b|$ where the system-bath coupling matrix elements are given by $H_{SB}^{(ab)} = \sum_{j=1}^{N} \Phi_{ab}(j)V_j$ and $\Phi_{ab}(j) = \phi_a(j)\phi_b(j)$ is the spatial overlap of excitons $|a\rangle$ and $|b\rangle$ at site j. MRT works well for systems in which there are quasi-localised excitons (ie. when the overlap $\Phi_{ab}(j)$ is small). The transfer rate between excitons a and b is given by the expression [51]

$$k_{ab} = 2\int_0^\infty dt \exp(i\omega_{ab}t - i(\lambda_{aaaa} + \lambda_{bbbb} - 2\lambda_{bbaa})t - g_{aaaa}(t) - g_{bbbb}(t) + 2g_{bbaa}(t)) \times (\ddot{g}_{baba}(t) - (\dot{g}_{babb} - \dot{g}_{baaa} + 2i\lambda_{babb})^2) \tag{2.20}$$

where the exciton reorganisation energies and line broadening functions are given by $\lambda_{pqrs} = \sum_j \phi_p(j)\phi_q(j)\phi_r(j)\phi_s(j)\lambda_j$ and $g_{pqrs}(t) = \sum_j \phi_p(j)\phi_q(j)\phi_r(j)\phi_s(j)g_j(t)$. $\phi_p(j)$ is the amplitude of exciton p on site j, λ_j is the reorganisation energy of site j and $g_j(t)$ is the line broadening function for site j.

The reorganisation energies and line broadening functions depend on the interaction between the electronic system and the vibrational environment defined through the spectral density $J(\omega)$. The general expression for the line broadening function is [46]

$$\begin{aligned} g(t) &= \int_0^t ds \int_0^s ds' C(s') \\ &= -\frac{1}{\pi}\int_0^\infty d\omega \frac{J(\omega)}{\omega^2}\left[\coth\frac{\beta\omega}{2}(\cos\omega t - 1) - i(\sin\omega t - \omega t)\right] \end{aligned} \tag{2.21}$$

When evaluated for a Drude spectral density the line broadening function has the form

$$g_D(t) = \frac{c_D^{(0)}}{\Omega_D^2}\left(e^{-\Omega_D t} + \Omega_D t - 1\right) + \sum_{k=1}^{\infty}\frac{c_D^{(k)}}{\nu_k^2}\left(e^{-\nu_k t} + \nu_k t - 1\right) \tag{2.22}$$

while for an underdamped Brownian oscillator the line broadening function is

$$g_q(t) = \sum_{+,-} \frac{c_q^{\pm}}{\nu_q^{\pm 2}}(e^{-\nu_q^{\pm} t} + \nu_q^{\pm} t - 1) + \sum_{k=1}^{\infty} \frac{c_q^{(k)}}{\nu_k^2}(e^{-\nu_k t} + \nu_k t - 1) \tag{2.23}$$

The coefficients $c_D^{(0)}$, $c_D^{(k)}$, $c_q^{\pm}$ and $c_q^{(k)}$ are the expansion coefficients of the associated correlation function and are defined in Section 2.1.1. The total line broadening function for a site coupled to a Drude spectral density and several underdamped modes is defined $g(t) = g_D(t) + \sum_q g_q(t)$. In principle the summations over Matsubara frequencies ν_k in Eqs. (2.22) and (2.23) run to infinity but must be truncated for practical purposes. A suitable value of k allowing for convergence of the series must be chosen depending on the temperature.

2.1.2.3 Förster Theory

For regimes in which the inter-site couplings J_{ij} are weak relative to the system-bath coupling the theories described above will breakdown. In this case a rate equation must be derived in which the inter-site coupling is treated as the perturbation. This perturbation Hamiltonian can be written $H' = \sum_{i \neq j} H_S^{(ij)} |i\rangle\langle j|$ where the states $|i\rangle$ are localised excited states or charge transfer states. The resulting Förster rates [52, 51] describe the population transfer between weakly coupled donor and acceptor states

$$K_{ij} = \frac{1}{2\pi} |V_{ij}|^2 \int_{-\infty}^{\infty} d\omega \bar{D}_i(\omega) D_j(\omega) \tag{2.24}$$

where $\bar{D}_i(\omega)$ and $D_j(\omega)$ are the donor "fluorescence" and acceptor "absorption" line shapes respectively. We must emphasise here that the terms "fluorescence" and "absorption" line shapes are not used in the strict sense when referring to transitions between charge transfer states. These states have a zero transition dipole moment so do not interact with the electromagnetic field. Nevertheless considering the overlap of these line shapes is a useful conceptual tool, even for charge transfer states, since it quantifies the energetic overlap of the donor and acceptor states.

The application of Förster theory to excited state charge transfer can be made more transparent by expressing Eq. (2.24) in terms of the reorganisation energies

and line broadening functions of the donor and acceptor states which depend on the spectral density $J(\omega)$ and not on spectroscopic quantities [53, 47]

$$K_{ij} = 2|V_{ij}|^2 \int_0^\infty dt e^{i\omega_{ij}t} e^{-i(\lambda_i+\lambda_j)t} e^{-(g_i(t)+g_j(t))} \tag{2.25}$$

The reorganisation energies λ_i and line broadening functions $g_i(t)$ are defined in the previous section. Compared to Marcus or Levich-Jortner theories, which are often used to describe charge transfer processes, Eq. (2.25) allows a complete quantum mechanical description of the vibrational environment rather than approximating some or all of the vibrational modes as classical oscillators [54].

Förster theory can also be generalised to describe incoherent transfer between weakly coupled delocalised states. A typical scenario would involve two clusters of chromophores, a donor cluster D and an acceptor cluster A. There is strong coupling within the clusters such that delocalised states can form, but weak coupling between the clusters. In this case the electronic coupling between delocalised states in D and A is a weighted sum of the site couplings $V_{ab} = \sum_{i\in D, j\in A} \phi_a(i)\phi_b(j)V_{ij}$. Here the label a (b) indicates a delocalised state in cluster D (A) while the quantity $\phi_k(n)$ is the amplitude of the delocalised state k at site n. The reorganisation energies and line broadening functions for the delocalised states are also weighted sums of the site quantities described in the previous section.

2.1.3 Hierarchical Equations of Motion

In contrast to the formalisms already discussed, the hierarchical equations of motion (HEOM) involve a non-perturbative description of the dynamics for the total system [40]. This allows for treatment of an arbitrary system-bath coupling strength which means we can use the HEOM to interpolate between perturbative theories valid in different regimes [41]. This comes at the cost of increased numerical effort in order to solve the equations and restricts the size of the systems that can feasibly be studied. The HEOM have been successfully applied to describe excitation energy transfer in photosynthetic systems [41, 55] as well as electron transfer reactions [56, 57].

Starting from the Liouville-von Neumann equation in the interaction picture, Eq. (2.11), an exact solution for the reduced density matrix of the system can be obtained as

$$\tilde{\rho}(t) = \tilde{\mathcal{U}}(t)\tilde{\rho}(0) \tag{2.26}$$

where the time propagator $\tilde{\mathcal{U}}(t)$ is defined

$$\tilde{\mathcal{U}}(t) = \mathrm{tr}_B\Big\{T_+ \exp[-i\int_0^t ds\tilde{\mathcal{L}}_I(s)]\rho_B\Big\} \tag{2.27}$$

$\tilde{\mathcal{L}}_I(t)$ is the super-operator describing the system-bath coupling in the interaction picture and T_+ is the time ordering operator. Using the path integral formalism, this time propagator can be written in terms of the Feynman-Vernon influence functional $\mathcal{F}_{FV}$ [58] which contains terms describing the effect of the bath on the system of interest

$$\tilde{\mathcal{U}}[q_f(t), q_i(t)] = \int_{q_i(t)}^{q_f(t)} Dq e^{iS[q]}\mathcal{F}_{FV}[q(t)]e^{-iS[q]} \tag{2.28}$$

where the influence functional can be written explicitly as

$$\mathcal{F}_{FV}[q(t)] = \exp\Big\{-\sum_j \int_{t_i}^t d\tau V_j^\times[q(\tau)]\tilde{V}_j^\times[q(\tau)]\Big\} \tag{2.29}$$

V_j is the part of the system-bath coupling operator that acts on the system and the notation $V^\times \bullet = V\bullet - \bullet V^\dagger$ has been introduced. Taking successive derivatives of the influence functionals and introducing auxiliary influence functionals leads to a hierarchy of equations containing the nth-tier influence functional

$$\mathcal{F}_{\mathbf{n}}[q(t)] = \Pi_{jk}(-i\tilde{V}_j^\times[q(t)])^{n_{jk}}\mathcal{F}_{FV}[q(t)] \tag{2.30}$$

This scheme relies on an exponential form of the bath correlation functions such as those applicable for Brownian oscillator spectral densities (see Eqs. (2.7) and (2.8)). Following on from this, defining the auxiliary propagator

$$\mathcal{U}_{\mathbf{n}}[q_f(t), q_i(0)] = \int_{q_i(0)}^{q_f(t)} Dq e^{iS[q]}\mathcal{F}_{\mathbf{n}}[q(t)]e^{-iS[q]} \tag{2.31}$$

leads to the definition of the auxiliary density matrices

$$\sigma_{\mathbf{n}}(t) = \mathcal{U}_{\mathbf{n}}[q_f(t), q_i(0)]\sigma(0) \tag{2.32}$$

Equations of motion for these auxiliary density matrices then have the general form

$$\begin{aligned}\dot{\sigma}_{\mathbf{n}}(t) = [\mathcal{L} &- \mathbf{n}.\nu]\sigma_{\mathbf{n}}(t) \\ &+ i\sum_{j}^{N}\sum_{k}^{K} V_j^{\times}\sigma_{\mathbf{n}_{jk}^{+}}(t) \\ &+ i\sum_{j}^{N}\sum_{k}^{K} n_{jk}(c_{jk}V_j)^{\times}\sigma_{\mathbf{n}_{jk}^{-}}(t)\end{aligned} \tag{2.33}$$

The auxiliary density matrices contain information about the state of the bath and are inter-dependent with the system density matrix $\rho(t) = \sigma_{\mathbf{0}}(t)$. The vector $\mathbf{n} = \{n_{10}, ..., n_{1k}, ..., n_{j0}, ..., n_{jk}, ..., n_{N0}, ..., n_{Nk}\}$ indexes each term k in the exponential expansion of the correlation function for each site j. The notation $\mathbf{n}_{jk}^{\pm}$ indicates the vector $\mathbf{n}$ with element $n_{jk} \rightarrow n_{jk} \pm 1$. Equation (2.33) is written in a general form for harmonic baths described by a correlation function that may be composed of the exponential expansions of an arbitrary sum of independent Drude and underdamped Brownian oscillator baths [59]. The expansion coefficients c_{jk} appearing in Eq. (2.33) are defined in Section 2.1.1.

2.1.3.1 Improving Convergence

In principle, the hierarchy of equations extends to infinity, however for practical purposes it must be truncated at some tier N_{trunc} giving solutions that have converged close to the exact results. The number of auxiliary density matrices for a given truncation level is $\mathcal{N} = \sum_{n=0}^{N_{trunc}} \frac{(n+K)!}{n!K!}$ where $(K+1)$ is the number of exponential terms in the correlation function expansion across all sites [60]. A major limitation of the HEOM is therefore its numerical cost. Since the number of auxiliary density matrices increases rapidly with the number of tiers as well as the number of expansion coefficients of the correlation functions, it can be difficult to obtain converged results for systems composed of more than a handful of sites.

Various improvements to the hierarchical equations of motion in Eq. (2.33) have been made in order to reduce the number of tiers required for convergence. By rescaling the auxiliary density matrices as $\tilde{\sigma}_{\mathbf{n}}(t) = (\Pi_k n_k! |c_k|^{n_k})^{-\frac{1}{2}} \sigma_{\mathbf{n}}(t)$ [60], such that the amplitude of auxiliary density matrices at higher tiers decay to zero, less tiers are needed for convergence. Additionally a Markovian truncation scheme can be applied by replacing terms proportional to correlation functions in the tier above N_{trunc} by a delta function $\delta(t)$ [61]. This reduces the number of Matsubara terms needed for converged results which is particularly important at low temperatures. The rescaled equations including the Markovian truncation term Ξ are

$$\begin{aligned}\dot{\sigma}_{\mathbf{n}}(t) = [\mathcal{L} &- \mathbf{n}.\nu - \Xi]\sigma_{\mathbf{n}}(t) \\ &+ i\sum_{j}^{N}\sum_{k}^{K}\sqrt{(n_{jk}+1)c_{jk}}V_j^{\times}\sigma_{\mathbf{n}_{jk}^{+}}(t) \\ &+ i\sum_{j}^{N}\sum_{k}^{K}\sqrt{\frac{n_{jk}}{|c_{jk}|}}(c_{jk}V_j)^{\times}\sigma_{\mathbf{n}_{jk}^{-}}(t)\end{aligned} \tag{2.34}$$

The Markovian truncation term has the form

$$\Xi = \sum_{j}^{N}\sum_{k=K}^{\infty}\Psi_{jk}V_j^{\times}V_j^{\times} \tag{2.35}$$

where $\sum_{k=1}^{\infty}\Psi_{jk} = \frac{2\lambda_D - \beta\Omega_D\lambda_D\cot(\frac{\beta\Omega_D}{2})}{\beta\Omega_D} + \frac{\lambda_0}{2\zeta_0}\left(\frac{\sin(\frac{\beta\gamma_0}{2}) + \gamma_0\sinh(\beta\zeta_0)}{\cos(\frac{\beta\gamma_0}{2}) - \cosh(\beta\zeta_0)}\right) + \frac{2\gamma_0}{\beta\omega_0^2}$ for a spectral density consisting of a Drude bath plus an underdamped Brownian oscillator.

2.2 Electron Counting Statistics

Electron counting statistics provides a framework in which to characterise the dynamical properties of electron transport systems through the probability distribution of the number of charges transferred to an collector in a given time period. More specifically, it is the moments or cumulants of the probability distribution that can give an insight into the electron transport behaviour. They can provide information on quantum coherence [62], energy level structure [63] and vibrational environment [64] which may be inaccessible through other means. A technique originat-

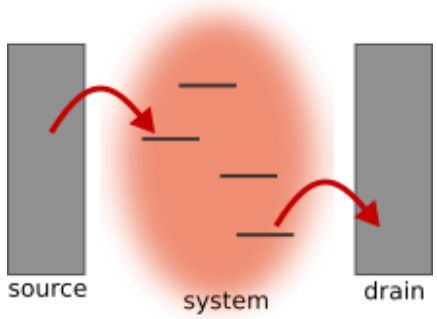

Figure 2.3: A typical counting statistics setup. A mesoscopic system consisting of several discrete energy levels and a heat bath is coupled to source and drain leads.

ing from the field of optics [65], the counting statistics of electron transport was first formulated using a scattering theory approach [30, 31]. It has since been extended such that the counting statistics can be calculated using both Markovian and non-Markovian master equation approaches [32, 33, 66, 67, 68]. Finite-frequency formulations of the theory [69, 33] which can access dynamical system information on different time scales have also been developed. Both zero-frequency and finite-frequency statistics have been measured experimentally in solid state systems [70, 62, 71, 72, 73]. A typical counting statistics setup involves a mesoscopic system attached to source and drain leads which supply and remove electrons from the system respectively. This is illustrated schematically in Fig. 2.3.

2.2.1 Markovian Theory of Electron Counting Statistics

The starting point for the derivation of the zero-frequency current cumulants is a Markovian quantum master equation for the reduced density matrix of the system where the leads have been traced out. The Hamiltonian for the system and leads will typically take the form of Eq. (2.1) with the fermionic source and drain leads (See Fig. 2.3) described by $H_B = \sum_{\alpha=\{L,R\}} \sum_p \varepsilon_{\alpha,p} d^\dagger_{\alpha,p} d_{\alpha,p}$ where $d^{(\dagger)}_{\alpha,p}$ annihilates (creates) an electron in the pth energy level of lead α having energy $\varepsilon_{\alpha,p}$. The operators $d^{(\dagger)}_{\alpha,p}$ obey the fermionic commutation relation $[d_{\alpha,p}, d^\dagger_{\beta,q}] = \delta_{\alpha\beta}\delta_{pq}\mathcal{I}$ The system-lead interaction has the form

$$H_{SB} = \sum_{\alpha=L,R} \sum_p (V_{\alpha,p} d^\dagger_{\alpha,p} s_\alpha + h.c.) \tag{2.36}$$

where the strength of the coupling is $V_{\alpha,p}$ and the operator s_α causes a transition between system energy levels as an electron tunnels into lead α. With weak system-lead coupling and fast decaying lead correlation functions, use of the Born-Markov master equation [74, 75] is justified which puts the focus on coherent electron transport within the system. Substituting the interaction Hamiltonian of Eq. (2.36) into Eq. (2.17) and assuming a constant density of states for the leads [76, 75] we obtain a master equation of the form

$$\begin{aligned}\dot{\rho}(t) = -i[H_S, \rho(t)] + \frac{\Gamma_L}{2}(1-f_L)\mathcal{D}(s_L^\dagger) + \frac{\Gamma_L}{2} f_L \mathcal{D}(s_L) \\ + \frac{\Gamma_R}{2}(1-f_R)\mathcal{D}(s_R^\dagger) + \frac{\Gamma_R}{2} f_R \mathcal{D}(s_R)\end{aligned} \tag{2.37}$$

where $f_\alpha = (e^{\beta\varepsilon_\alpha}+1)^{-1}$ is the Fermi function of lead α and $\Gamma_\alpha = 2\pi\sum_p |V_{\alpha,p}|^2 \delta(E - \varepsilon_{\alpha,p})$ is the rate of transfer to or from lead α. $D(s_\alpha^{(\dagger)})$ is a Lindblad dissipator describing the coupling to the leads and having the form given in Eq. (2.19). In the remainder of this thesis the infinite bias limit [75, 33, 74] is used which ensures unidirectional transport through the system from the source (L) to the drain (R) lead. Physically this rests on an assumption that the bias window between the source and drain leads is larger than other energy scales in the system while analytically it amounts to setting $f_L = 1$ and $f_R = 0$. A further approximation that can often be justified based on the details of the system of interest is the Coulomb blockade regime [32, 33]. The system Hamiltonian can include a term for double occupation of the system with an energy U, the Coulomb repulsion between the two electrons. If this energy scale is very large then the state space of the system can be restricted to the empty state and those states where only a single excess electron is present in the system.

The master equation for the system dynamics under the influence of the leads may be written in the form $\dot{\rho}(t) = \mathcal{L}\rho(t)$ where the Liouvillian $\mathcal{L}$ is a superoperator describing both the coherent and incoherent dynamical processes of the system. From here there are several ways to proceed, including the n-resolved density matrix approach to express the current cumulants in terms of a generating function [33],

or using the characteristic polynomial of the Liouvillian [68]. Instead, we construct a recursive scheme using Rayleigh-Schrödinger perturbation theory to generate the current cumulants to arbitrary order [66, 67]. This makes numerical calculation much easier compared to the generating function approach which involves repeated differentiation.

The generator of the system dynamics can be written $\mathcal{L} = \mathcal{L}_0 + \mathcal{L}_J$ where the time evolution of the system between counting transitions is described by $\mathcal{L}_0$ and the incoherent counting transitions are described by the jump operator $\mathcal{L}_J$. Reinterpreting the jump operator as a perturbation with exponential parameter $e^{i\chi}$, the generator becomes

$$\mathcal{L}(\chi) = \mathcal{L} + \Delta\mathcal{L}(\chi) \tag{2.38}$$

where $\Delta\mathcal{L}(\chi) = \mathcal{L}_J(e^{i\chi} - 1)$. The current cumulants are obtained from the maximal eigenvalue $\lambda_0(\chi)$ of $\mathcal{L}(\chi)$ which becomes $\lambda_0(0) = 0$ and solves the eigenvalue problem

$$\mathcal{L}(\chi)|0(\chi)\rangle\rangle = \lambda_0(\chi)|0(\chi)\rangle\rangle \tag{2.39}$$

$|0(\chi)\rangle\rangle$ being the steady state left-eigenvector of $\mathcal{L}(\chi)$. The eigenvalue can be written

$$\lambda_0(\chi) = \langle\langle\tilde{0}|\Delta\mathcal{L}(\chi)|0(\chi)\rangle\rangle \tag{2.40}$$

where the properties $\langle\langle\tilde{0}|\mathcal{L} = 0$ (steady state right-eigenvector acting on unperturbed generator) and $\langle\langle\tilde{0}|0(\chi)\rangle\rangle = 1$ (normalisation) were used.

Using the projectors $\mathcal{P} = \mathcal{P}^2 = |0\rangle\rangle\langle\langle\tilde{0}|$ (projects onto the steady state subspace of the system) and $\mathcal{Q} = \mathcal{Q}^2 = I - \mathcal{P}$ (projects onto the space orthogonal to the steady state) the steady state can be written

$$|0(\chi)\rangle\rangle = |0\rangle\rangle + \mathcal{Q}|0(\chi)\rangle\rangle \tag{2.41}$$

Additionally using $\mathcal{L} = \mathcal{Q}\mathcal{L}\mathcal{Q}$ the eigenvalue equation can be written

$$\mathcal{Q}\mathcal{L}(\chi)\mathcal{Q}|0(\chi)\rangle\rangle = [\lambda_0(\chi) - \Delta\mathcal{L}(\chi)]|0(\chi)\rangle\rangle \tag{2.42}$$

Introducing the pseudo-inverse $\mathcal{R} = \mathcal{Q}\mathcal{L}^{-1}\mathcal{Q}$ which is well defined since it is performed in the subspace orthogonal to the steady state (more precisely this is the Drazin group generalised inverse [77]). We then have

$$\mathcal{Q}|0(\chi)\rangle\rangle = \mathcal{R}[\lambda_0(\chi) - \Delta\mathcal{L}(\chi)]|0(\chi)\rangle\rangle \tag{2.43}$$

which on substituting in Eq. (2.41) gives us

$$|0(\chi)\rangle\rangle = |0\rangle\rangle + \mathcal{R}[\lambda_0(\chi) - \Delta\mathcal{L}(\chi)]|0(\chi)\rangle\rangle \tag{2.44}$$

Equations (2.40) and (2.44) are the starting points for the recursive scheme. Expanding the zero eigenvalue $\lambda_0(\chi)$, steady state $|0(\chi)\rangle\rangle$ and the perturbation $\Delta\mathcal{L}(\chi)$ about $\chi = 0$ gives

$$\lambda_0(\chi) = \sum_{n=1}^{\infty} \frac{(i\chi)^n}{n!}\langle\langle I^n\rangle\rangle \tag{2.45}$$

$$|0(\chi)\rangle\rangle = \sum_{n=0}^{\infty} \frac{(i\chi)^n}{n!}|0^{(n)}\rangle\rangle \tag{2.46}$$

$$\Delta\mathcal{L}(\chi) = \sum_{n=1}^{\infty} \frac{(i\chi)^n}{n!}\mathcal{L}^{(n)} \tag{2.47}$$

Substituting these expansions into Eqs. (2.40) and (2.44) gives the following expressions to calculate the cumulant to any order ($n = 1, 2, 3, \ldots$)

$$\langle\langle I^n\rangle\rangle = \sum_{m=1}^{n} \binom{n}{m} \langle\langle\tilde{0}|\mathcal{L}^{(n)}|0^{(n-m)}\rangle\rangle \tag{2.48}$$

$$|0^{(n)}\rangle\rangle = \mathcal{R}\sum_{m=1}^{n} \binom{n}{m} [\langle\langle I^m\rangle\rangle - \mathcal{L}^{(m)}]|0^{(n-m)}\rangle\rangle \tag{2.49}$$

The first and second order cumulant which are used to obtain the numerical results later on are explicitly shown below

$$\langle\langle I^1\rangle\rangle = \langle\langle\tilde{0}|\mathcal{L}^{(1)}|0\rangle\rangle \tag{2.50}$$

$$\langle\langle I^2\rangle\rangle = \langle\langle\tilde{0}|\mathcal{L}^{(2)} - 2\mathcal{L}^{(1)}\mathcal{R}\mathcal{L}^{(1)}|0\rangle\rangle \tag{2.51}$$

It is useful to note that $\mathcal{L}^{(n)} = \mathcal{L}_J$ in the above since $\frac{\partial^n}{\partial(i\chi)^n}\Delta\mathcal{L}(\chi)|_{\chi=0} = \frac{\partial^n}{\partial(i\chi)^n}\mathcal{L}_J(e^{i\chi}-1)|_{\chi=0}$.

In principle $\mathcal{L}$ can generate any time-local dynamics, no assumption needs to be made above about the exact form as long as the counting transition is an incoherent jump process. $\mathcal{L}$ is further constrained to describe the dynamics of a fully connected system such that there is only a single steady state.

2.2.2 Fano Factor

A useful quantity with which to characterise current fluctuations is the second order Fano factor (or relative noise strength) [78]. It is defined as the ratio of the second order current cumulant to the mean current.

$$F^{(2)} = \frac{\langle\langle I^2 \rangle\rangle}{\langle\langle I \rangle\rangle} \tag{2.52}$$

For $F^{(2)} = 1$ the waiting times between subsequent electron counting events are uncorrelated such that the statistics is Poissonian. A Fano factor less than 1 indicates sub-Poissonian statistics where the electron transport becomes more ordered and the relative noise is reduced. Conversely a Fano factor greater than 1 indicates super-Poissonian statistics with disordered, irregular electron transport with an increase in relative noise.

Chapter 3

Non-Perturbative Electron Counting Statistics

Electron transport through organic molecules is a process fundamental to life and plays a crucial role in single molecule junctions. Full characterisation of the steady state transport process involves determining higher order moments beyond the mean using the theory of full counting statistics. Most theoretical frameworks used to obtain higher order moments of the current rely on perturbative approximations with respect to either the electron-phonon coupling or the electronic tunnelling coupling within the system of interest. These frameworks are not generally well suited to describing electron transfer through molecules since these couplings are often on the same order of magnitude. In the following chapter, the electron counting statistics of a double quantum dot is investigated to understand the signatures coherence might leave in the current fluctuations. Then a non-perturbative approach to electron counting statistics is developed which permits an analysis of the effect of non-equilibrium phonons on the current fluctuations. This approach is demonstrated by comparison with a perturbative theory for a simple dimer system coupled to a phonon bath.

Some of the work in this chapter is taken from: *Non-perturbative electron counting statistics*, R. Stones and A. Olaya-Castro (2017) arXiv:1705.02320

3.1 Counting Statistics of a Double Quantum Dot

Double quantum dots (DQDs) are excellent test systems for investigating the role of quantum effects in electron transport through mesoscopic systems. The first few moments of the current passing through quantum dot systems fabricated as semiconductor devices have been measured experimentally using quantum point contacts [70, 62, 71, 72]. Furthermore a large number of theoretical studies have used DQDs as model systems to demonstrate new advances in the field [69, 66, 67, 79, 80]. We will first try to understand some of the main features that quantum coherence may leave in the current fluctuations in order to lay the foundations for a discussion of the effect of electron-phonon coupling in a molecular dimer system.

A typical counting statistics setup is shown in Fig. 2.3. In the case of a DQD, the system consists of two electronic levels having the Hamiltonian

$$H_S = \frac{\varepsilon}{2}(|L\rangle\langle L| - |R\rangle\langle R|) + T_c(|L\rangle\langle R| - |R\rangle\langle L|) \tag{3.1}$$

where ε is the energy bias between the dots and T_c is the electronic tunnelling coupling between them. The states $|L\rangle$ and $|R\rangle$ represent an excess electron occupying either the left or right dot respectively. There is also an unoccupied state of the system $|0\rangle$ such that the electronic identity operator is $I = |0\rangle\langle 0| + |L\rangle\langle L| + |R\rangle\langle R|$. This restriction of the electronic state space enforces the Coulomb blockade regime [32]. The Hamiltonian for the fermionic leads has the form

$$H_L = \sum_{\alpha=L,R}\sum_{p} \varepsilon_p d^\dagger_{\alpha,p} d_{\alpha,p} \tag{3.2}$$

while the system-lead interaction is

$$H_{LS} = \sum_{\alpha=L,R}\sum_{p} V_{\alpha,p} d_{\alpha,p} s^\dagger_\alpha + V^*_{\alpha,p} d^\dagger_{\alpha,p} s_\alpha \tag{3.3}$$

where $V_{\alpha,p}$ describes the coupling strength between energy level p of lead α and dot α, $d^{(\dagger)}_{\alpha,p}$ is the annihilation (creation) operator for an electron in energy level p of lead α and $s^{(\dagger)}_\alpha$ is the annihilation (creation) operator of an electron on dot

α. Following from several assumptions about the leads including weak coupling to the electronic system, constant density of states and Fermi energies $f_L(\varepsilon_p) = 1$ and $f_R(\varepsilon_p) = 0$ (see Section 2.2.1), we can derive a master equation for the electronic system [76, 75]

$$\dot{\rho}_S(t) = -i[H_S, \rho_S(t)] + \sum_{\alpha=L,R} \Gamma_\alpha \left[s_\alpha \rho_S s_\alpha^\dagger - \frac{1}{2}\{s_\alpha^\dagger s_\alpha, \rho_S\} \right] \tag{3.4}$$

where ρ_S is the system density matrix and coupling to the leads in described by a dissipator having Lindblad form so that $s_L = |L\rangle\langle 0|$ and $s_R = |0\rangle\langle R|$ are Lindblad operators coupling the left and right dots to the left and right leads respectively. Transport is unidirectional such that the left lead acts as a source or emitter, while the right lead acts as a drain or collector. Using Eqs. (2.50) and (2.51) we can then calculate the first two current cumulants. This requires rewriting Eq. (3.4) in Liouville space $\dot{\rho}_S(t) = \mathcal{L}\rho(t)$ to obtain the time generator $\mathcal{L}$. In particular, we will investigate the current statistics for electrons tunnelling from the system into the drain lead so the jump operator used in the calculations is simply s_R expanded into Liouville space. We will use the second order Fano factor $F^{(2)}(0)$, given in Eq. (2.52) to quantify the current correlations. $F^{(2)}(0) = 1$ indicates uncorrelated transport while deviations from unity may indicate sub- ($F^{(2)}(0) < 1$) or super- ($F^{(2)}(0) > 1$) Poissonian transport.

While Eqs. (2.50) and (2.51) can be easily evaluated numerically, analytic results often give more insight into the physics of a problem. To understand the role played by coherence in the behaviour of the DQD an expression for the second order Fano factor in terms of the stationary state populations and coherences was derived from Eq. (2.51)

$$\begin{aligned} F^{(2)}(0) = 1 + \frac{2}{\frac{1}{4}\Gamma_R^2\Gamma_L + 2T_c^2\Gamma_L + 4\varepsilon^2\Gamma_L + T_c^2\Gamma_R} \Big[& -T_c^2\Gamma_R\rho_{LL} \\ & - \left(\frac{1}{4}\Gamma_R^2\Gamma_L + T_c^2\Gamma_R + 4\varepsilon^2\Gamma_L\right)\rho_{RR} \\ & + 4T_c\varepsilon\Gamma_L \mathrm{Re}(\rho_{LR}) + T_c\Gamma_R\Gamma_L \mathrm{Im}(\rho_{LR}) \Big]. \end{aligned} \tag{3.5}$$

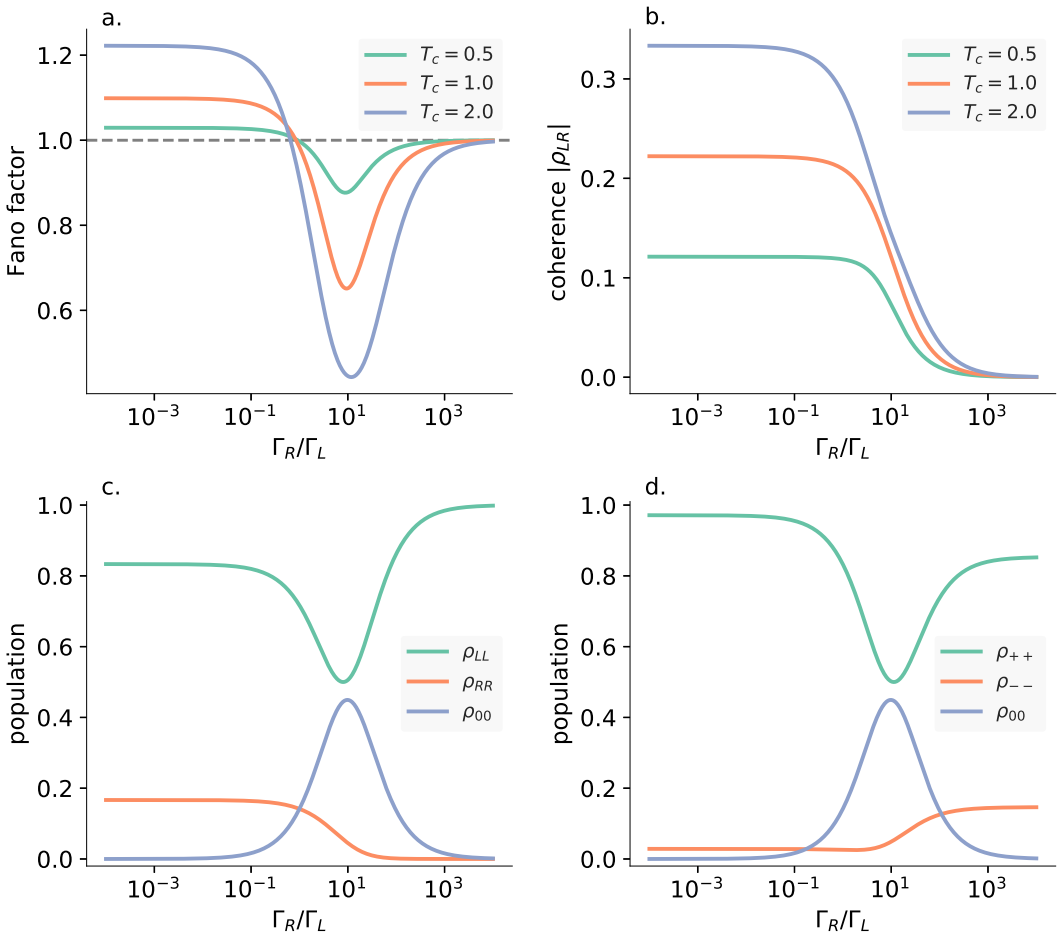

Figure 3.1: Behaviour of a double quantum dot varying drain lead tunnelling rate Γ_R. (a) Fano factor and (b) absolute value of inter-dot coherence in the site basis for different values of inter-dot coupling T_c. (c) Stationary state populations in the site basis for an inter-dot coupling $T_c = 2$. (d) Stationary state populations in the eigenstate basis for an inter-dot coupling $T_c = 2$. Other parameters used in all figures are $\Gamma_L = 1$ and $\varepsilon = 4$.

The Fano factor is sensitive to both steady state populations and coherences with the contribution of the coherences dropping off as the energy bias becomes large. The Fano factor as a function of Γ_R is shown in Fig. 3.1 (a). There are three regimes worth pointing out: Firstly, for values of Γ_R comparable to other parameters in the system, transport through the DQD is sub-Poissonian, which reflects a reduction in current fluctuations compared to the uncorrelated Poissonian case. Secondly, when Γ_R is very large the Fano factor tends to 1 and electron transport becomes Poissonian. This is a result of strong dephasing of coherence in the site basis ρ_{LR} as can be seen in Fig. 3.1 (b). This causes localisation of the system in the left dot, as shown in Fig. 3.1 (c), and an almost complete blockage of current flowing through

the system such that waiting times between subsequent electrons tunnelling into the drain are extremely long. Finally, for very small Γ_R a transition to super-Poissonian statistics can be observed. This is behaviour reminiscent of the dynamical channel blockade [62, 79] and coincides with an increase in the stationary state coherence in the site basis ρ_{LR} shown in Fig. 3.1 (b). In fact, we can see in Eq. (3.5) that in the limit $\Gamma_R \ll 1$ the Fano factor is proportional to $Re(\rho_{LR})$. In this regime there is very little dephasing and this allows transport to occur through either the symmetric $|+\rangle$ or anti-symmetric $|-\rangle$ states in the eigenstate basis of the system. Since the time scales for transport through these two pathways are very different due to the different couplings to the leads, an effective dynamical channel blockade regime is observed. In Fig. 3.1 (d) we can see that for small Γ_R the system spends most of its time in the symmetric state quasi-localised on the left dot. This state has a small transfer rate to the drain lead relative to the anti-symmetric state and blocks the electron flow through the system. On the occasions that an electron occupies the anti-symmetric state, tunnelling into the drain lead will occur relatively quickly.

Now fixing the rate to leave the system as $\Gamma_R = 0.025$, the Fano factor as a function of energy bias is shown in Fig. 3.2 (a). The Fano factor is symmetric about zero bias and drops off to 1 at large energy gaps where the current through the system would drop to zero. The peaks coincide exactly with maxima in the stationary state coherence ρ_{LR} shown in Fig. 3.2 (b) further demonstrating the dependence of the Fano factor on coherence in this regime. The observed symmetry around $\varepsilon = 0$ reflects the coherent evolution between the dots without interruption from dissipative processes.

In the rest of this chapter we will use the parameter regime $\Gamma_R \ll 1$ in order to emphasise the effect of dissipative processes due to a phonon bath on the Fano factor. Since the Fano factor depends strongly on the site basis coherence in this regime we should be able to gain an insight into how coupling to a phonon bath affects coherent transfer through the system.

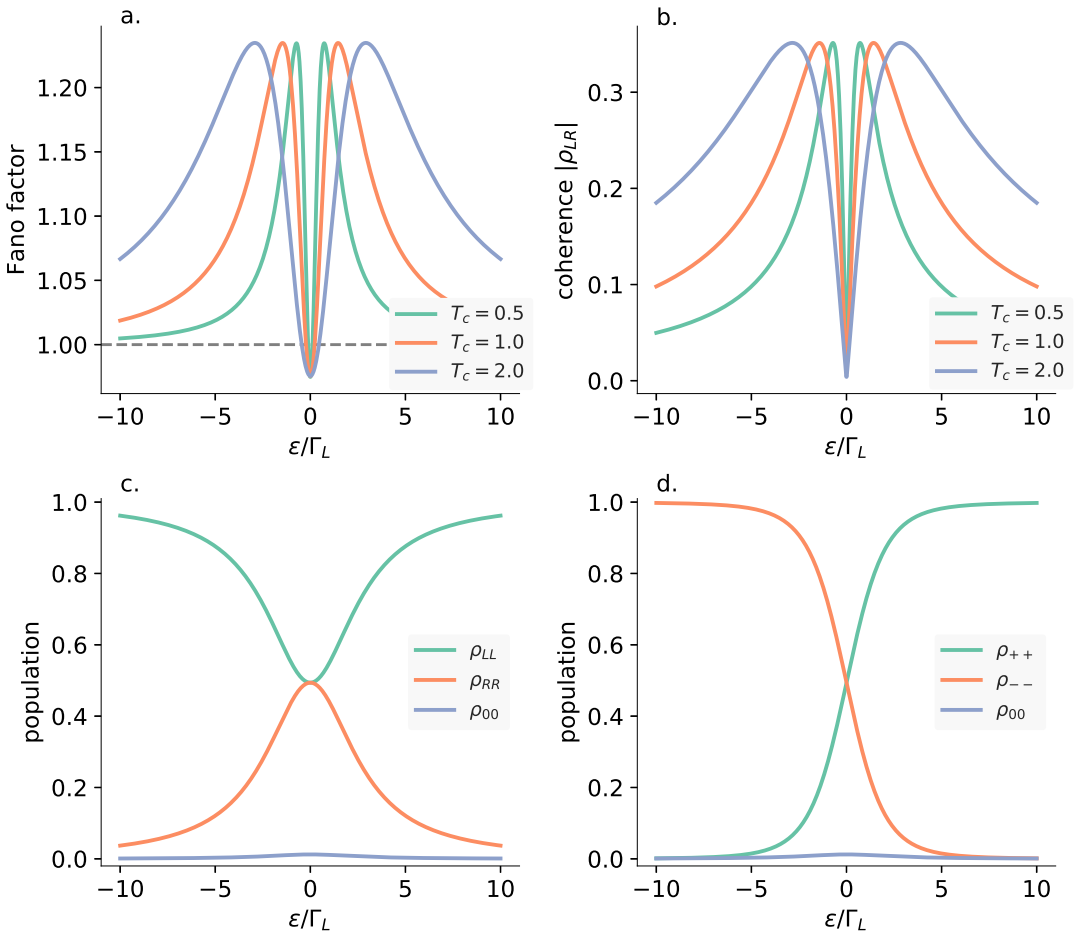

Figure 3.2: Behaviour of a double quantum dot varying energy bias ε. (a) Fano factor and (b) absolute value of inter-dot coherence as a function of energy bias for different values of inter-dot coupling T_c. (c) Stationary state populations in the site basis for an inter-dot coupling $T_c = 2$. (d) Stationary state populations in the eigenstate basis for an inter-dot coupling $T_c = 2$. Other parameters used in all figures are $\Gamma_L = 1$ and $\Gamma_R = 0.025$.

3.2 Non-Perturbative Method for Electron Counting Statistics

Having discussed the counting statistics of an isolated double quantum dot model, we will now introduce coupling to a phonon bath and develop a non-perturbative method of counting statistics in order to calculate cumulants of the current while treating the system-bath dynamics exactly. The method presented here differs from a previous work incorporating the theory of full counting statistics with the hierarchical equations of motion [81] which deals with higher order moments of bath observables rather than the current cumulants we are interested in here. We also note an alternative non-perturbative approach utilising path integrals to generate the full

counting statistics of electron transfer through multi-band conductors via an analysis of transmission coefficients [82]. In comparison ours is restricted to vibrational environments described by sums of Brownian oscillators but this makes it particularly applicable to the problem of electron transfer through organic molecules. To illustrate our method, we will use a dimer molecule coupled to a bosonic bath and fermionic leads. The left and right sites of the dimer are labelled $|L\rangle$ and $|R\rangle$ respectively while the only other electronic state considered is the unoccupied state $|0\rangle$, with the Coulomb blockade enforced similarly to the DQD model. The Hamiltonian for the full system is $H = H_S + H_B + H_L + H_{SB} + H_{SL}$ where

$$H_S = \frac{\varepsilon}{2}(|L\rangle\langle L| - |R\rangle\langle R|) + T_c(|L\rangle\langle R| + |R\rangle\langle L|) \tag{3.6}$$

$$H_B = \sum_q \omega_q b_q^\dagger b_q \tag{3.7}$$

$$H_L = \sum_{\alpha=L,R}\sum_p \varepsilon_{\alpha,p} d_{\alpha,p}^\dagger d_{\alpha,p} \tag{3.8}$$

are the Hamiltonians for the system, bath and leads respectively, with $\hbar = 1$. Here, ε is the energy bias between the left $|L\rangle$ and right $|R\rangle$ dimer sites and T_c is the electronic tunnelling coupling between them. ω_q is the frequency of the qth bosonic mode while $b_q^{(\dagger)}$ annihilates (creates) a phonon in the qth mode. Finally $\varepsilon_{\alpha,k}$ is the energy of an electron in the kth energy level of lead α while $d_{\alpha,k}^{(\dagger)}$ annihilates (creates) an electron in the kth energy level of lead α. The system-bath and system-lead interactions are described by

$$H_{SB} = \sum_{\alpha=L,R}\sum_q g_{\alpha,q} V_\alpha (b_q^\dagger + b_q) \tag{3.9}$$

$$H_{SL} = \sum_{\alpha=L,R}\sum_p t_{\alpha,p} d_{\alpha,p}^\dagger s_\alpha + t_{\alpha,p}^* d_{\alpha,p} s_\alpha^\dagger \tag{3.10}$$

The electron-phonon coupling between site α and phonon mode q is given by $g_{\alpha,q}$ while $V_\alpha = |\alpha\rangle\langle\alpha|$ is the system coupling matrix operator. $t_{\alpha,p}$ is the tunnelling coupling between site α and pth energy level in lead α. The operator $s_\alpha^{(\dagger)}$ annihilates (creates) an electron on site α. A reduced second-order master equation for the electronic system and phonon bath under the influence of the leads is derived in a

similar manner to the DQD model discussed earlier (see Section 2.2.1). This leads to the master equation in the Schrödinger picture

$$\frac{d}{dt}P(t) = -i[H_S + H_B + H_{SB}, P(t)] + \mathcal{D}_L\big(P(t)\big) \tag{3.11}$$

where $P(t) = tr_L\{\rho_{SB}(t) \otimes \rho_L(t)\}$. The dissipator $\mathcal{D}_L\big(P(t)\big)$ describes the action of the leads on the electronic system and has the same Lindblad form as the dissipator in Eq. (3.4) for the DQD model. Here we must mention a potential inconsistency that is yet to be investigated fully. The formalism developed here uses the assumption that the leads couple to the electronic states alone (see Eq. (3.10)), regardless of the strength of the electron-phonon coupling. A more complete formalism would consider coupling of the leads to mixed vibronic states, though the extent to which it would affect the following results needs further analysis.

Starting from Eq. (3.11), we can now derive the hierarchical equations of motion (HEOM) with respect to the electron-phonon coupling (see Section 2.1.3). A hierarchy of auxiliary density matrices is constructed, each having the equation of motion

$$\begin{aligned}\dot{\sigma}_{\mathbf{n}}(t) = [\mathcal{L} \;&-\; \mathbf{n}.\nu]\sigma_{\mathbf{n}}(t) \\ &+\; i\sum_{\alpha=L,R}\sum_{k}^{K} V_\alpha^{\times}\sigma_{\mathbf{n}^+_{\alpha k}}(t) \\ &+\; i\sum_{\alpha=L,R}\sum_{k}^{K} n_{\alpha k}(c_{\alpha k}V_\alpha)^{\times}\sigma_{\mathbf{n}^-_{\alpha k}}(t)\end{aligned} \tag{3.12}$$

A detailed description of this equation is given in Section 2.1.3 but it is important to note here that the electronic system density matrix $\rho_S = \sigma_0(t)$ is at the top of the hierarchy with auxiliary density matrices below it containing information about the state of the phonon bath as well as system-bath correlations. Additionally, the operator $\mathcal{L}\bullet = -i[H_S, \bullet] + \mathcal{D}_L(\bullet)$ appears at every level in the hierarchy and contains the dissipator describing the coupling between the system and leads [83, 74]. The HEOM can be used with Brownian oscillator spectral densities which have been previously used to describe electron transport in organic molecules [57, 84, 59]. To

solve these coupled equations the HEOM may be formulated as a time-local master equation for the vector of auxiliary density matrices $\boldsymbol{\sigma}(t)$

$$\dot{\boldsymbol{\sigma}}(t) = \mathcal{H}\boldsymbol{\sigma}(t) \tag{3.13}$$

where the hierarchy matrix $\mathcal{H}$ generates the dynamics described by Eqs. (3.12).

In an analogous scheme to the Markovian theory of counting statistics (see Section 2.2.1) the hierarchy matrix is split into two parts $\mathcal{H} = \mathcal{H}_0 + \mathcal{H}_J$. $\mathcal{H}_0$ describes the evolution of the system and auxiliary density matrices between electron tunnelling events from the system to the drain lead. $\mathcal{H}_J$ therefore describes these system to drain lead tunnelling events and consists of the part of the dissipator $\mathcal{D}_L$ in Eq. (3.4) containing s_R and acts on the system density matrix such that it appears in the top level of the hierarchy only. The dissipators in the rest of the hierarchy are contained within $\mathcal{H}_0$. Augmenting $\mathcal{H}_J$ with a counting field χ, the current cumulants can be derived by following a recursive formalism set out in Section 2.2.1. Restating the first and second order current cumulants in terms of the non-perturbative equations of motion gives

$$\langle\langle I^1 \rangle\rangle = \langle\langle \tilde{0}|\mathcal{H}^{(1)}|0\rangle\rangle \tag{3.14}$$

$$\langle\langle I^2 \rangle\rangle = \langle\langle \tilde{0}|\mathcal{H}^{(2)} - 2\mathcal{H}^{(1)}\mathcal{R}\mathcal{H}^{(1)}|0\rangle\rangle \tag{3.15}$$

where $|0\rangle\rangle$ and $\langle\langle\tilde{0}|$ are the right and left stationary state eigenvectors of $\mathcal{H}$, the operators $\mathcal{H}^{(n)} = \mathcal{H}_J$ and $\mathcal{R}$ is the pseudo-inverse of $\mathcal{H}$. The left eigenvector is defined analytically, satisfying the normalisation condition $\langle\langle\tilde{0}|0\rangle\rangle = 1$. In practice this means $\langle\langle\tilde{0}|$ is the vector containing 1s for elements corresponding to the position of populations of the system density matrix in the top level of the hierarchy. The normalisation condition is therefore effectively summing over the populations of the system density matrix. These expressions provide a relatively straightforward numerical scheme to calculate the first two current cumulants. For efficient computation of these quantities, sparse data structures must be used and the problem of

calculating the pseudo-inverse $\mathcal{R}$ transformed into the calculation of the solution to a linear matrix equation [77]. In order to obtain converged results using the HEOM, the hierarchy must be truncated at a suitable tier N_{trunc} and a sufficient number of Matsubara terms K must be included. This is discussed in more detail along with some additional techniques to improve the convergence in Section 2.1.3.1. In particular, for calculations in the remainder of this chapter we use a rescaling of the auxiliary density matrices [60] and a Markovian truncation [61].

3.2.1 Drude Spectral Density

To demonstrate the application of this non-perturbative method, we compare the electron counting statistics of our dimer system with a model using a weak coupling approximation (WCA) for the system-bath interaction [85, 62]. The time generator for the WCA in the basis $\{\rho_{00}, \rho_{LL}, \rho_{RR}, Re(\rho_{LR}), Im(\rho_{LR})\}$ reads [62]

$$\mathcal{L} = \begin{pmatrix} -\Gamma_L & 0 & \Gamma_R e^{i\chi} & 0 & 0 \\ \Gamma_L & 0 & 0 & 0 & 2T_c \\ 0 & 0 & -\Gamma_R & 0 & -2T_c \\ 0 & \gamma_+ & -\gamma_- & -\frac{\Gamma_R}{2} - \gamma & -\varepsilon \\ 0 & -T_c & T_c & \varepsilon & -\frac{\Gamma_R}{2} - \gamma \end{pmatrix} \tag{3.16}$$

where

$$\gamma = \frac{2\pi T_c^2}{\Delta^2} J(\Delta) \coth\left(\frac{\beta\Delta}{2}\right) \tag{3.17}$$

$$\gamma_\pm = -\frac{\pi\varepsilon T_c}{2\Delta^2} J(\Delta) \coth\left(\frac{\beta\Delta}{2}\right) \mp \frac{\pi T_c}{2\Delta} J(\Delta) \tag{3.18}$$

are the general expressions for the dephasing rates with an arbitrary spectral density $J(\Delta)$ evaluated at the energy splitting between electronic eigenstates $\Delta = \sqrt{\varepsilon^2 + 4T_c^2}$. As with the models presented earlier in this chapter ε is the energy bias between left and right molecules and T_c is the tunnelling coupling between the molecules while the rates Γ_L and Γ_R represent the coupling to the left (source) and right (drain) leads. The Drude spectral density $J_D(\omega) = \frac{2\lambda_D \Omega_D \omega}{\omega^2 + \Omega_D^2}$ is used here where λ_D is the reorganisation energy of the bath quantifying the system-bath coupling

strength, and Ω_D is the cutoff frequency quantifying the bath relaxation time. This form of the spectral density has been successfully used in combination with the hierarchical equations of motion to describe electron transfer in organic molecules [57, 84]. Notice the addition of the counting field χ in an element of the WCA time generator Eq. (3.16). This defines the jump operator describing the transition where an electron tunnels from the system to the drain lead. This is the transition across which we investigate the statistics. The counting statistics for this model are calculated using the Markovian expressions Eqs. (2.50) and (2.51) and the Fano factor Eq. (2.52).

As previously discussed, we use a small value for Γ_R in order to focus on the effect of the system-bath interaction on coherent electron transport, without significant dephasing due to the leads. In an isolated double quantum dot model this parameter regime would exhibit super-Poissonian current statistics indicating the dynamical channel blockade regime (see Fig. 3.1 (a)).

As before, the central quantity used to quantify the current fluctuations is the Fano factor $F^{(2)}(0)$ which we show as a function of energy bias ε for a small reorganisation energy $\lambda_D = 0.015$ in Fig. 3.3 (a) and (b). Compared to the isolated DQD model, there are two main features to notice on the introduction of coupling to a phonon bath with both the weak coupling and non-perturbative models. Firstly, there is a reduction in the Fano factor relative to the isolated DQD model. This is related to a reduction of the steady state coherence due to the extra dephasing processes introduced by the phonon bath which we can see in Fig. 3.3 (c) and (d). Secondly, there is an asymmetry of the Fano factor in the cases of positive and negative bias. This arises due to the difference in the dephasing processes for phonon emission and absorption. At positive biases, forward electron transfer occurs primarily through both stimulated and spontaneous phonon emission coinciding with downhill transfer between the electronic eigenstates. Conversely at negative biases, forward electron transfer occurs through uphill transfer between electronic eigenstates mediated by stimulated phonon absorption only. Now comparing the Fano factor for the weak coupling (Fig. 3.3 (a)) and non-perturbative methods (Fig. 3.3

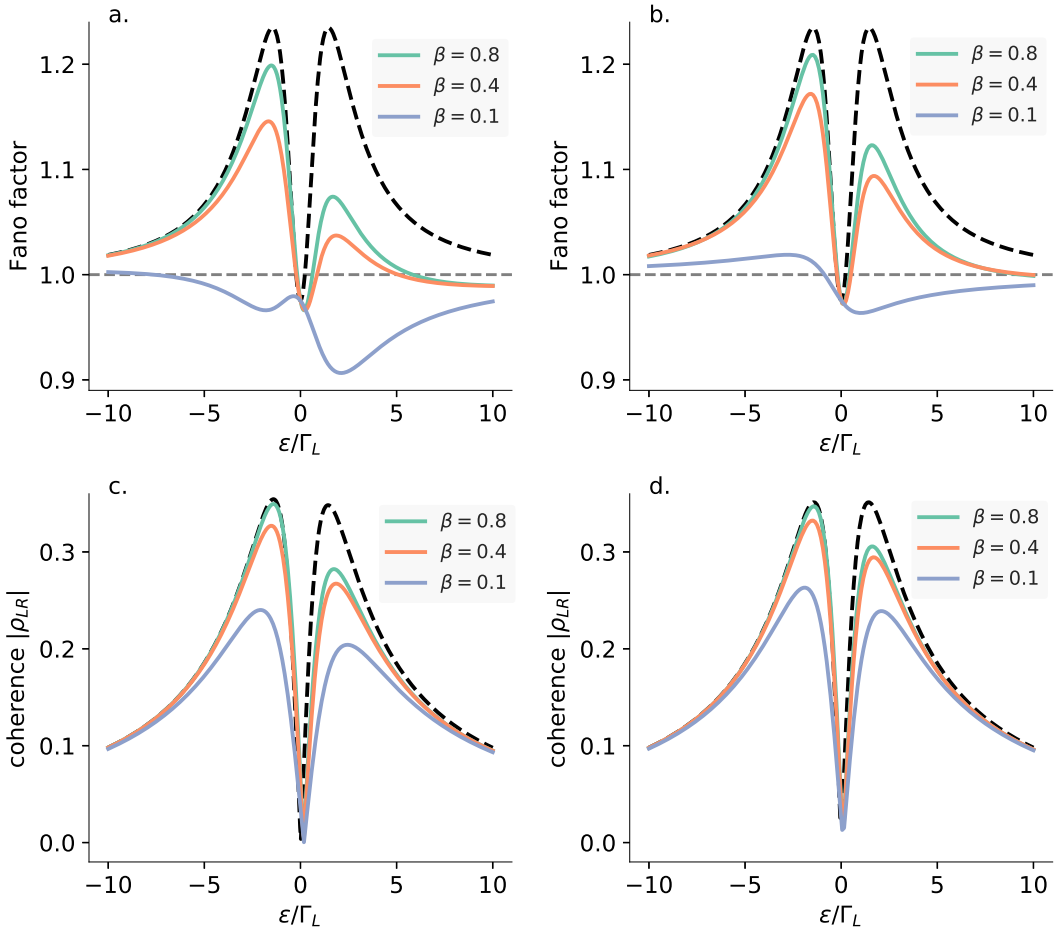

Figure 3.3: Fano factor and coherence as a function of energy bias for a dimer coupled to a Drude bath. (a) Fano factor as a function of energy bias ε for the weak coupling approximation. (b) Fano factor as a function of energy bias ε for the non-perturbative method. (c) Stationary state site basis coherence for the weak coupling approximation. (d) Stationary state site basis coherence for the non-perturbative method. The parameter $\beta = \frac{1}{k_B T}$ is the inverse temperature. Other parameters used are $T_c = 1$, $\Gamma_L = 1$, $\Gamma_R = 0.025$, $\lambda_D = 0.015$, $\Omega_D = 50$. Non-perturbative calculations were truncated at level $N = 6$ and using $K = 6$ Matsubara terms. The black dashed lines are for the double quantum dot system without coupling to a phonon bath.

(b)), it is interesting that even with a small reorganisation energy there are significant differences in the predictions of the two theories. The Fano factor is greater for the non-perturbative method as is the stationary state coherence. This indicates that an exact, non-Markovian description of the system-bath dynamics takes into account recurrences of coherence in the electronic system as well as dephasing processes. This is particularly pronounced for the high temperature case with $\beta = 0.1$. At negative biases the character of the electron statistics is sub-Poissonian for the weak coupling approximation while it is super-Poissonian for the non-perturbative

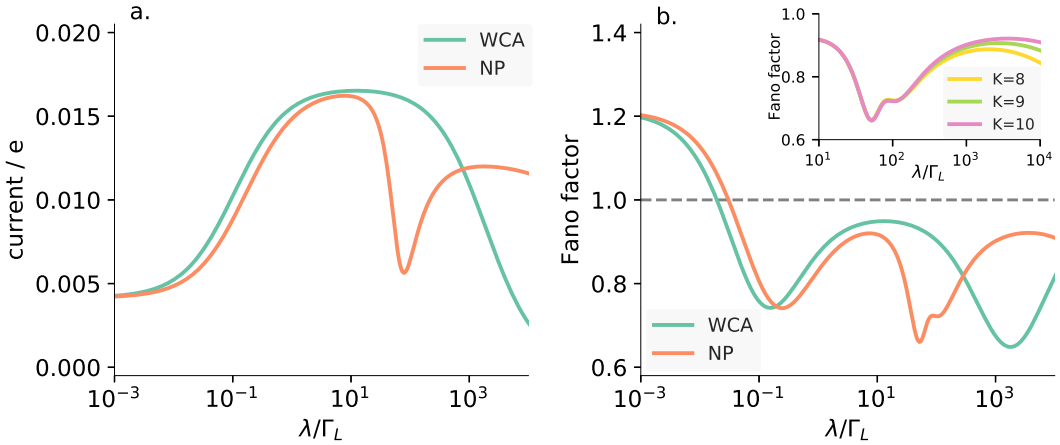

Figure 3.4: Mean current and Fano factor as a function of reorganisation energy for a dimer system coupled to a Drude bath. (a) Mean current and (b) Fano factor as a function of reorganisation energy for the weak coupling approximation and the non-perturbative method. The non-perturbative calculations truncate the hierarchy at $N = 6$ including $K = 10$ Matsubara terms. The inset in (b) shows the convergence of the Fano factor with number of Matsubara terms. Parameters used are $\beta = 0.4$, $\varepsilon = 2$, $T_c = 1$, $\Gamma_L = 1$, $\Gamma_R = 0.025$, $\Omega_D = 50$.

approach.

The current and Fano factor as a function of reorganisation energy λ_D at inverse temperature $\beta = 0.4$, is shown in Fig. 3.4 for the weak coupling and non-perturbative methods. For small reorganisations energies, where the bath has only a slight influence on the electronic system, the weak coupling approximation and the non-perturbative theory give consistent results in both the first two current cumulants. As the reorganisation energy becomes the largest energy scale in the system, qualitative differences start to emerge in the predictions of both theories which signals the breakdown of the weak coupling approximation. However, due to the low temperature regime we have used the results are unconverged for reorganisation energies greater than around $\lambda_D = 10^2$. At low temperatures a large number of Matsubara terms need to be included in the correlation function expansion in order to capture the quantum behaviour of the bath. The inset of Fig. 3.4 (b) demonstrates the convergence of the Fano factor with an increasing number Matsubara terms. Unfortunately with such a number of Matsubara terms it becomes numerically infeasible to simultaneously converge the hierarchy in the number of tiers. The larger the reorganisation energy becomes the more important the effect of the system-bath correlations and hence more tiers are required to properly describe the system be-

haviour. The behaviour of the current and Fano factor above $\lambda_D \approx 10^2$ in Fig. 3.4 is therefore an artifact of the unconverged hierarchy.

In order to demonstrate converged results for the current and Fano factor as a function of reorganisation energy we also present results using parameters representative of the photosynthetic systems we are interested in. In this parameter regime using temperature $T = 300K$ we can obtain converged results for very large reorganisation energies because no Matsubara terms are required. The number of tiers required for convergence varies depending on the value of the reorganisation energy but we have used up to $N = 100$ for the largest reorganisation energy calculations. Fig. 3.5 shows the current and Fano factor as a function of reorganisation energy for electron transport across a photosynthetic dimer. Similarly to Fig. 3.4 the current and Fano factor are constant for small reorganisation energies with the Fano factor showing super-Poissonian statistics. The weak coupling approximation and non-perturbative method compare well in this regime. However as the reorganisation energy increases we start to see a divergence in the behaviour of the two methods. With the non-perturbative method the current increases to a maximum before dropping towards zero at very large reorganisation energies. At moderate reorganisation energies, the maximum in the current is a consequence of dephasing processes counteracting reversible coherent transfer allowing localisation of electrons on the right site which can then be transferred to the drain lead. For large reorganisation energies the effect of the bath is to localise the system in the left site before any coherent transfer can take place to the right site and subsequently the drain lead, hence zero current is measured. For the Fano factor, the non-perturbative method exhibits a double minimum before tending towards 1 as the reorganisation energy becomes very large. The origin of the double minimum is not clear but is probably related to renormalisation of electronic states as the system transitions from a dynamical channel blockade regime with delocalised electronic states at small reorganisation energies to a sequential tunnelling regime with localised electronic states at large reorganisation energies.

For future work it will be necessary to compare this non-perturbative method

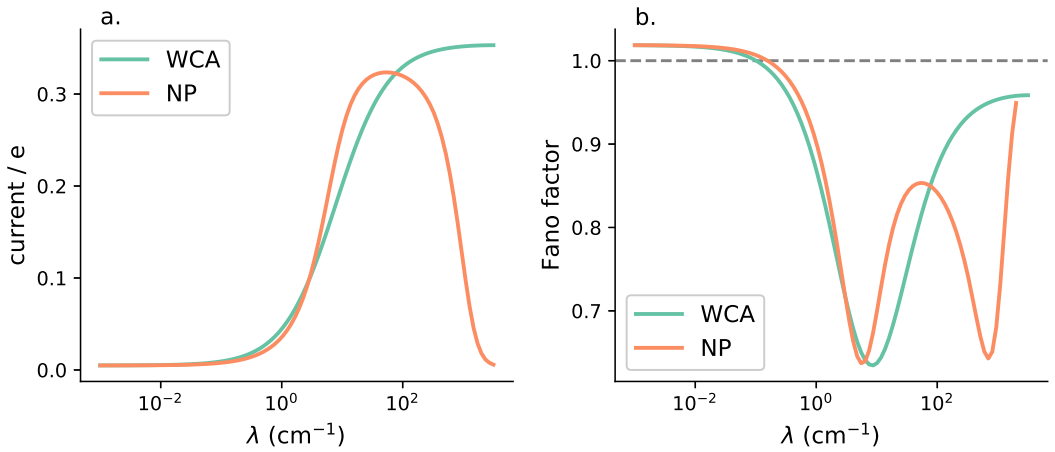

Figure 3.5: Mean current and Fano factor as a function of reorganisation energy for a photosynthetic dimer system coupled to a Drude bath at room temperature. (a) Mean current and (b) Fano factor as a function of reorganisation energy for the weak coupling approximation and the non-perturbative method. The non-perturbative calculations use a variable truncation scheme with up to $N = 100$ tiers used for the largest reorganisation energies. No Matsubara terms are included. Parameters used are $\varepsilon = 200\text{cm}^{-1}$, $T_c = 20\text{cm}^{-1}$, $\Gamma_L = 20\text{cm}^{-1}$, $\Gamma_R = 0.5\text{cm}^{-1}$, $\Omega_D = 50\text{cm}^{-1}$, $T = 300K$.

with other formalisms valid in the regime of strong system-bath coupling. For instance, the polaron model [85, 74] is perturbative in the electronic tunnelling coupling such that the system-bath interaction is described exactly.

3.2.2 Underdamped Brownian Oscillator Spectral Density

Coupling to discrete vibrational modes is also an important feature of electron transfer in molecular systems. The full counting statistics has previously been calculated for such systems coupled to discrete vibrations utilising other methods [36, 86, 37, 74]. We now carry out calculations considering the effect of an underdamped Brownian oscillator spectral density on the current and Fano factor. For the non-perturbative method the spectral density has the form $J_{BO}(\omega) = \Theta(\omega)\frac{2\Lambda\gamma\omega_0^2\omega}{(\omega^2-\omega_0^2)^2+\gamma^2\omega^2}$ where ω_0 is the frequency of the mode, γ is the damping constant and $\Lambda = S\omega_0$ is the reorganisation energy associated with the mode, with S being the Huang-Rhys factor [43]. With this spectral density the hierarchical equations of motion take a slightly different form to those for a Drude spectral density [59] (see Section 2.1.3). Rather than comparing the non-perturbative theory to the weak coupling approximation, we use a model in which an independent damped mode is coherently coupled to each site. This is in an attempt to keep the model

consistent with the non-perturbative method where a phonon bath is independently coupled to each site.

In the coherent mode model the system Hamiltonian is

$$\begin{aligned} H_S = \; & \tfrac{\varepsilon}{2} \quad (|L\rangle\langle L| - |R\rangle\langle R|) + T_c(|L\rangle\langle R| + |R\rangle\langle L|) \\ & + \sum_{\alpha=L,R} \omega_\alpha b_\alpha^\dagger b_\alpha + \sum_{\alpha=L,R} g_\alpha V_\alpha (b_\alpha^\dagger + b_\alpha) \end{aligned} \tag{3.19}$$

The coupling between the electronic and vibrational systems is given by $g_\alpha = \sqrt{S_\alpha}\omega_\alpha$ where we use the same values for the Huang-Rhys factor S and frequency ω as in the spectral density of the non-perturbative method. The mode is damped using a Lindblad dissipator of the form

$$\begin{aligned} \mathcal{D}_{mode}(\rho(t)) = \; & \textstyle\sum_{\alpha=L,R} \quad \Big[\gamma_\alpha(n(\omega_\alpha)+1)\Big(b_\alpha \rho(t) b_\alpha^\dagger - \frac{1}{2}\{b_\alpha^\dagger b_\alpha, \rho(t)\}\Big) \\ & + \quad \gamma_\alpha n(\omega_\alpha)\Big(b_\alpha^\dagger \rho(t) b_\alpha - \frac{1}{2}\{b_\alpha b_\alpha^\dagger, \rho(t)\}\Big)\Big] \end{aligned} \tag{3.20}$$

where the quantities γ_α are temperature independent damping rates and $n(\omega_\alpha) = (e^{\beta\omega_\alpha} - 1)^{-1}$ gives the occupation number of mode α at inverse temperature β. Coupling with the leads is included in the same way in both models, through the dissipator $\mathcal{D}_L\Big(\rho(t)\Big)$. The current and Fano factor are obtained using Eqs. (2.50), (2.51) and (2.52) (the Markovian analogues of Eqs. (3.14) and (3.15) derived earlier) with the same bath parameters used for both frameworks: $\omega_0 = \omega_L = \omega_R$, $S = S_L = S_R$ and $\gamma = \gamma_L = \gamma_R$.

A comparison for these two models is shown for inverse temperature $\beta = 0.1$ in Fig. 3.6. The current and Fano factor have the same qualitative features, with a peak at zero bias and enhancements in both quantities at resonance with the mode frequency. Asymmetry around zero bias is also present due to differences between phonon emission and absorption processes. The main qualitative difference however appears in the position of the peaks around the mode resonances. In the non-perturbative theory the peaks are shifted towards larger energies due to renormalisation of the electronic energy levels which is not fully captured in the coherent mode

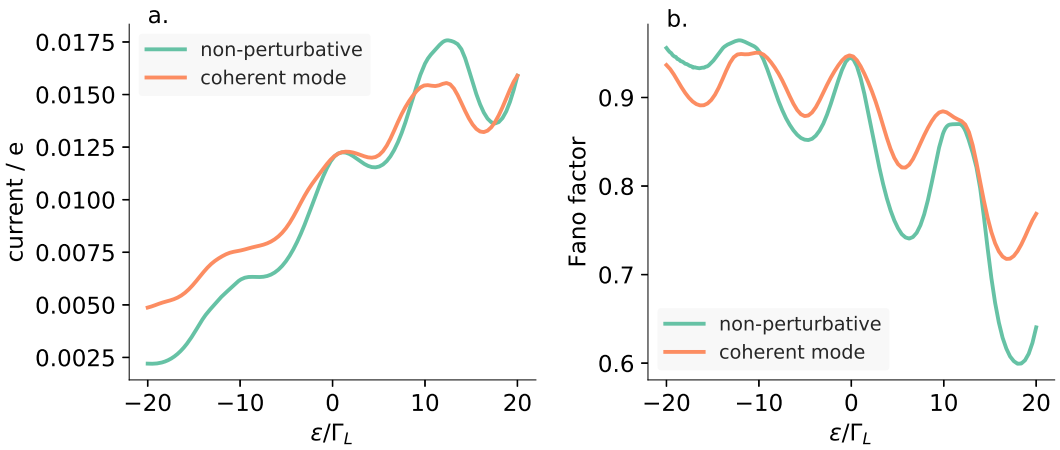

Figure 3.6: Mean current and Fano as a function of energy bias for dimer system coupled to an underdamped Brownian oscillator. (a) Mean current and (b) Fano factor as a function of electronic energy bias comparing Markovian electron counting statistics for a coherent mode model with the non-perturbative method. Parameters used are $\beta = 0.1$, $T_c = 1, \Gamma_L = 1, \Gamma_R = 0.025$, $\omega_0 = \omega_L = \omega_R = 10$, $S = S_L = S_R = 0.5$, $\gamma = \gamma_L = \gamma_R = 0.5$.

model.

3.3 Summary and Conclusions

We presented a new method to calculate the electron counting statistics in molecular systems. We combined the non-perturbative hierarchical equations of motion with a recursive scheme to calculate the cumulants of the current to arbitrary order. Calculations using this method were compared with a perturbative weak system-bath coupling approximation as well as a system containing coherent modes. The counting statistics generated by this new method contains some of the same qualitative features as that from the approximate models. It does however show a departure in the quantitative behaviour due to the exact treatment of the system-bath coupling. Comparison with other theories, in particular for a strong system-bath coupling, is still needed in order to fully evaluate the broad applicability of this method.

Chapter 4

On the Performance of a Photosystem II Reaction Centre Inspired Photocell

In this chapter we study a hypothetical photocell device inspired by the photosystem II reaction centre. This model is used to put forward several design principles for the use of pigment-protein complexes in nano-electronic devices. It is also used as a prototype system to investigate the possibility of accessing dynamical information about charge separation from the fluctuations of the output current. By comparing a structured spectral density to a smooth low energy background, we show the current and power output of the photocell decrease as the reorganisation energy of the chromophores increases. However at the same time there is a related reduction in the current fluctuations. The relevance of these findings for biological function is also discussed.

Some of the work in this chapter is taken from: *On the performance of a photosystem II reaction centre-based photocell*, R. Stones, H. Hossein-Nejad, R. van Grondelle, A. Olaya-Castro, Chemical Science (2017) doi:10.1039/C7SC02983G

4.1 Photosystem II Reaction Centre

The photosystem II reaction centre (PSIIRC) is part of the much larger photosystem II pigment-protein complex found in higher plants and green algae. Photosystem II

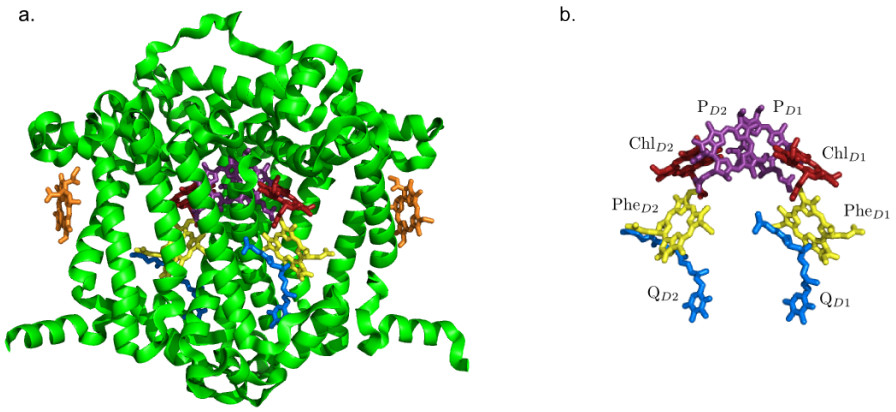

Figure 4.1: Photosystem II reaction centre structure. (a) The full photosystem II reaction centre with protein shown in green, along with the chromophores involved in charge separation. The chlorophylls of the special pair are shown in violet, the accessory chlorophylls in red, the pheophytins in yellow, the quinones in blue and the peripheral chlorophylls in orange. (b) The double branched structure of the core PSIIRC chromophores is shown with labels indicating their association with either the D1 or D2 branch.

consists of antennae complexes that deliver excitations to the reaction centre where a charge separation process is initiated. This in turn creates an electrochemical gradient across a membrane that is used to drive ATP production. This process ultimately sustains almost all life on Earth.

The structure of PSIIRC is shown in Fig. 4.1. The complex consists of a strongly coupled chlorophyll dimer called the special pair, flanked by two branches (labelled D1 and D2) containing an accessory chlorophyll, a pheophytin and a quinone each. There are two further chlorophylls spatially separated from the core chromophores which are shown only in Fig. 4.1 (a). Charge separation occurs only down the D1 branch and it remains an open question as to the origin of the asymmetry of this process [1]. Furthermore, charge separation may originate from either the special pair (P_{D1} pathway) or the accessory chlorophyll (Chl_{D1} pathway) depending on the realisation of static disorder, allowing the complex to be robust to slow fluctuations of the chromophore energies [87, 47]. The primary electron transfer step occurs on sub-picosecond time scales, with the electron reaching the Phe_{D1} in around 20ps [47].

The importance of PSIIRC in Nature is due to its water splitting functionality. It is the large electrochemical potential generated at the special pair that provides

the driving force required to oxidise water and produce oxygen [1]. PSIIRC has been the focus of intensive experimental and theoretical investigation for several decades. Its existence was first hinted at by the early experiments of Emerson and Arnold [88, 89, 1] though it was not isolated and its structure determined until much later. Since the excitation energies of the chromophores in PSIIRC are very similar, spectroscopic investigations have been somewhat difficult. However, in recent years as non-linear spectroscopy became more advanced, detailed information about the structure and function of the complex has been uncovered. The existence of the two transfer pathways was proposed by Novoderezhkin et al [47] while the first evidence for the role of quantum coherence in primary electron transfer emerged soon after [7, 8].

4.2 Photocell Model

A recent experiment demonstrated that individual photosynthetic protein units can be isolated and incorporated into electronic circuits such that the photocurrent through them may be measured [26]. The experiment involved covalent bonding of a photosystem I unit to a gold substrate and a scanning near-field optical microscopy tip using cysteine residue mutations. The photocurrent between the tip and the substrate was then measured, with electrons being transferred along the reaction centre electron transport chain. An earlier experiment also managed to measure the photocurrent through photosystem II units in a scanning tunnelling microscopy setup [27]. Inspired by this, we will study the mean current and current fluctuations of a hypothetical photocell based on the photosystem II reaction centre from the point of view of the device performance as well as biological function. We compare different vibrational environments to look at their effect on the current through the photocell.

The model we use for the theoretical photocell device consists of an individual PSIIRC unit placed between two electrodes as shown schematically in Fig. 4.2 (a). We propose using a silicon-field effect transistor positioned at the drain lead to detect the counting statistics [90, 91]. Only electron transfer along the Chl_{D1}

pathway is considered as the average protein configuration results in the lowest energy exciton state quasi-localised at the Chl_{D1} chromophore. There is no experimental evidence of coherent electron transfer along this pathway [47, 7] which is consistent with the weak coupling between the sites and primary charge transfer (CT) state. We therefore consider only incoherent charge transfer rates. Unidirectional electron flow through the system is assumed, such that coupling to the source and drain leads is described by the phenomenological rates Γ_L and Γ_R respectively. The Coulomb blockade is implemented by restricting the state space to ensure only occupation of the system by a single excess electron is allowed. The system is incoherently photo-excited at a rate γ_{ex} which is also assumed weak enough that the probability of double excitation states being present is negligible. The state space of the system is then: the ground state $|g\rangle$, six exciton states $|X_1\rangle$ to $|X_6\rangle$ formed from diagonalisation of the site part of the system Hamiltonian H_{el}, the initial CT state $|\mathrm{Chl}^+_{D1}\mathrm{Phe}^-_{D1}\rangle \equiv |I\rangle$, the secondary CT state $|\mathrm{P}^+_{D1}\mathrm{Phe}^-_{D1}\rangle \equiv |\alpha\rangle$ and the positively charged state $|\mathrm{P}^+_{D1}\mathrm{Phe}_{D1}\rangle \equiv |\beta\rangle$ which represents the 'empty' state of the system for counting statistics calculations. A schematic diagram of the state space of the system and the indicated dynamics is shown in Fig. 4.2 (b).

The energies of the site Hamiltonian H_{el}, the two charge transfer (CT) states as well as the ground and 'empty' state are shown in Table A.1. The excited state energies have been obtained by fitting model parameters to spectroscopic data [47] while the 'empty' state energy is taken from Ref. [17]. The inter-site couplings are shown in Table A.2 which can be calculated from high resolution X-ray crystallography data [92, 47].

A crucial aspect of modelling electron transfer in PSIIRC is the description of the vibrational environment interacting with the electronic part of the system. The photocell performance is compared for four cases of this vibrational environment with the spectral densities displayed in Fig. 4.3. These four cases are: (i) the full structured spectral density $J(\omega) = J_D(\omega) + J_M(\omega)$. The cases where, besides the low-energy background $J_D(\omega)$, spectral densities with either one or two well-resolved modes are included (ii) $J_1(\omega) = J_D(\omega) + G_1(\omega)$ and (iii) $J_2(\omega) = J_1(\omega) +$

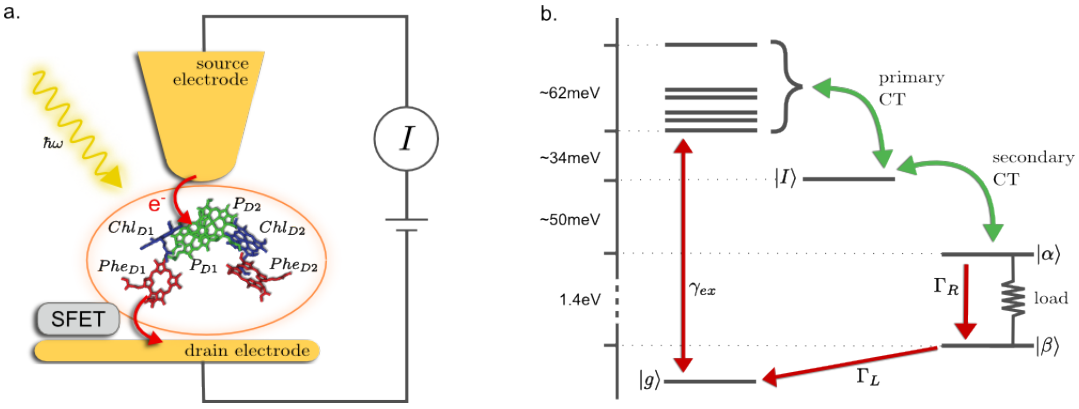

Figure 4.2: Photosystem II reaction centre photocell model. (a) Schematic diagram of a proposed experimental setup for the photocell. The isolated core chromophores of PSI-IRC are positioned between a gold substrate and a gold coated scanning near-field optical microscopy tip which act as electrodes. A silicon field-effect transistor (SFET) placed near the drain electrode could be used to measure the current statistics. (b) Energy level diagram showing the electronic state space of the model. Γ_L and Γ_R connect the system to the source and drain leads respectively while γ_{ex} represents coupling to an optical field which excites the system from the ground state to the lowest energy exciton state. Green arrows represent Förster rates for primary and secondary charge separation. The load between states α and β indicates the transition across which the output current of the photocell is calculated.

$G_2(\omega)$. Finally, (iv) the case where only the smooth low energy component $J_D(\omega)$ is coupled to the electronic system. The expressions for the different components are given by [46]:

$$J_D(\omega) = \frac{2\lambda_D\Omega_D\omega}{\omega^2+\Omega_D^2}, \tag{4.1}$$

$$G_j(\omega) = \frac{2\lambda_j\omega_j^2\gamma_j\omega}{(\omega^2-\omega_j^2)^2+\gamma_j^2\omega^2}. \tag{4.2}$$

$J_D(\omega)$ is the Drude form of a spectral density describing an overdamped Brownian oscillator where $\lambda_D = 35\text{cm}^{-1}$ and $\Omega_D = 40\text{cm}^{-1}$ are the reorganisation energy and cut off frequency, respectively. $G_j(\omega)$ describes the spectral density of an underdamped mode coupled to an excited pigment, with λ_j, ω_j and γ_j being the reorganisation energy, frequency and damping rate of mode j respectively. The reorganisation energy associated with an individual mode is given by $\lambda_j = s_j\omega_j$ where s_j is the Huang-Rhys factor of mode j [93]. $J_M(\omega) = \sum_j G_j(\omega)$ has been measured experimentally [94] and includes 48 underdamped modes, the frequen-

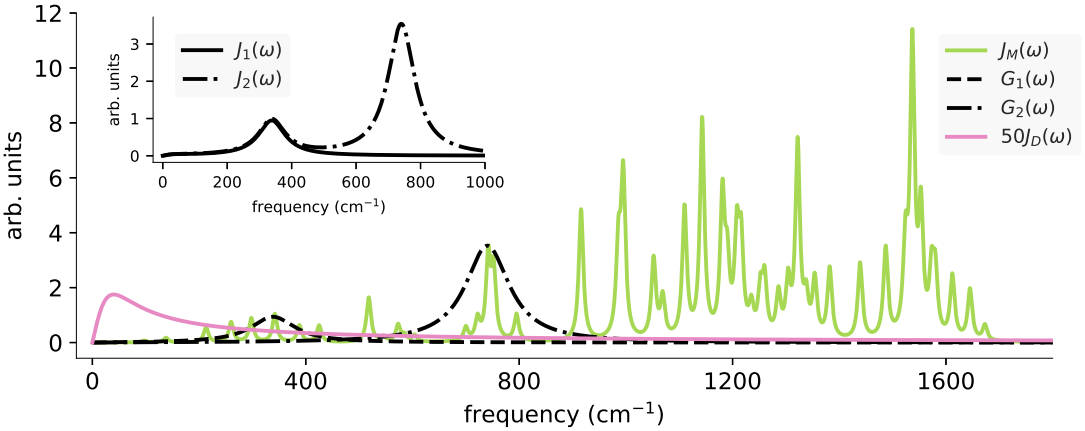

Figure 4.3: Photosystem II reaction centre spectral densities. The different components of the spectral densities used in the PSIIRC photocell model are shown. The Drude part $J_D(\omega)$ is scaled relative to the high energy parts for clarity. The inset shows the spectral densities $J_1(\omega)$ and $J_2(\omega)$ which are used to approximate the full spectral density.

cies and Huang-Rhys factors of which are shown in Table A.3. Each mode has the same damping $\gamma = 10\text{cm}^{-1}$. For case (ii) described by $J_1(\omega)$, we consider $\omega_1 = 342\text{cm}^{-1}$, $s_1 = 0.4$, $\gamma_1 = 100cm^{-1}$ and for case (iii) corresponding to $J_2(\omega)$, we consider the additional parameters $\omega_2 = 742\text{cm}^{-1}$, $s_2 = 0.32$, $\gamma_2 = 100cm^{-1}$. Modes with these frequencies have been observed to participate in electron transfer along the alternative P_{D1} charge separation pathway [7] and in this photocell model we increase the broadening so that they cover frequencies spanning all the energy gaps of the excited state manifold. Hence, $J_2(\omega)$ provides a good approximation to the full spectral density. To capture the stronger coupling of the CT states to the vibrational environment the factors $c_I = 3$ and $c_\alpha = 4$ are used to scale the reorganisation energy of these states.

4.3 Excited State Dynamics

In order to calculate the electron counting statistics through the PSIIRC photocell later on, we need to determine the steady state of the system from some set of dynamical equations of motion. The exciton dynamics is described by the Hamiltonian $H_{el} = \sum_i e_i|i\rangle\langle i| + \sum_{ij} T_{ij}(|i\rangle\langle j| + |j\rangle\langle i|)$ where i corresponds to the basis of single-excitation states of the six core chromophores i.e. $\{|\text{P}_{D1}\rangle, |\text{P}_{D2}\rangle, |\text{Chl}_{D1}\rangle, |\text{Chl}_{D2}\rangle, |\text{Phe}_{D1}\rangle, |\text{Phe}_{D2}\rangle\}$ and e_i are onsite energies given in Table A.1. The six eigenstates of H_{el} are denoted as $|X_1\rangle$ to $|X_6\rangle$ with corre-

sponding eigenenergies E_{X_1} to E_{X_6} in ascending order. The electronic operators $|i\rangle\langle i|$ couple linearly, with coupling constant $g_{i,q}$, to identical baths of harmonic oscillators $H_I = \sum_{i,q} g_{i,q}|i\rangle\langle i|(b_q^\dagger + b_q)$. The strength of the system-bath interaction is quantified by the spectral density that will be of the form $J(\omega)$, $J_D(\omega)$, $J_1(\omega)$ or $J_2(\omega)$.

A non-perturbative description of the excited state dynamics is extremely challenging using the full spectral density $J(\omega)$ including 48 underdamped modes, so we compare two models: (i) A hybrid approach using the non-perturbative hierarchical equations of motion (see Section 2.1.3) for the exciton dynamics while incoherent rates for charge transfer, photo-excitation and coupling to the leads are included through a Lindblad dissipator [83, 74]. This model is used with the spectral densities $J_D(\omega)$, $J_1(\omega)$ and $J_2(\omega)$. (ii) A Pauli master equation approach replacing the exact exciton dynamics with modified Redfield rates (see Section 2.1.2.2), leaving all other rates the same as in model (i). The Pauli rate equations have the form $|\dot{P}\rangle\rangle = M|P\rangle\rangle$, where $|P\rangle\rangle$ is a vector of state populations in the basis $\{|g\rangle, |X_1\rangle, \cdots |X_6\rangle, |I\rangle, |\alpha\rangle, |\beta\rangle\}$ and M is a stochastic matrix containing the rates for transfer between these electronic states. This model has previously been used to fit the results of transient spectroscopy experiments [47].

In both frameworks, weak electronic coupling between the excitons and the primary CT state as well as between the primary and secondary CT states is used to justify a description of charge transfer using Förster theory (see Section 2.1.2.3). Generalised Förster rates are used for primary charge transfer and Förster rates for the secondary CT step. Coupling to the leads and photo-excitation are included through further phenomenological rates. For clarity, this is illustrated in Fig. 4.2 (b).

A comparison of the population dynamics for these two models is shown in Fig. 4.4. There is a good agreement between the two frameworks for the spectral densities $J_D(\omega)$ and $J_1(\omega)$ which indicates that the Pauli model is accurate enough to gain some insight into the behaviour of the system. The dynamics of the Pauli model with the full spectral density $J(\omega)$ is also shown. An important difference

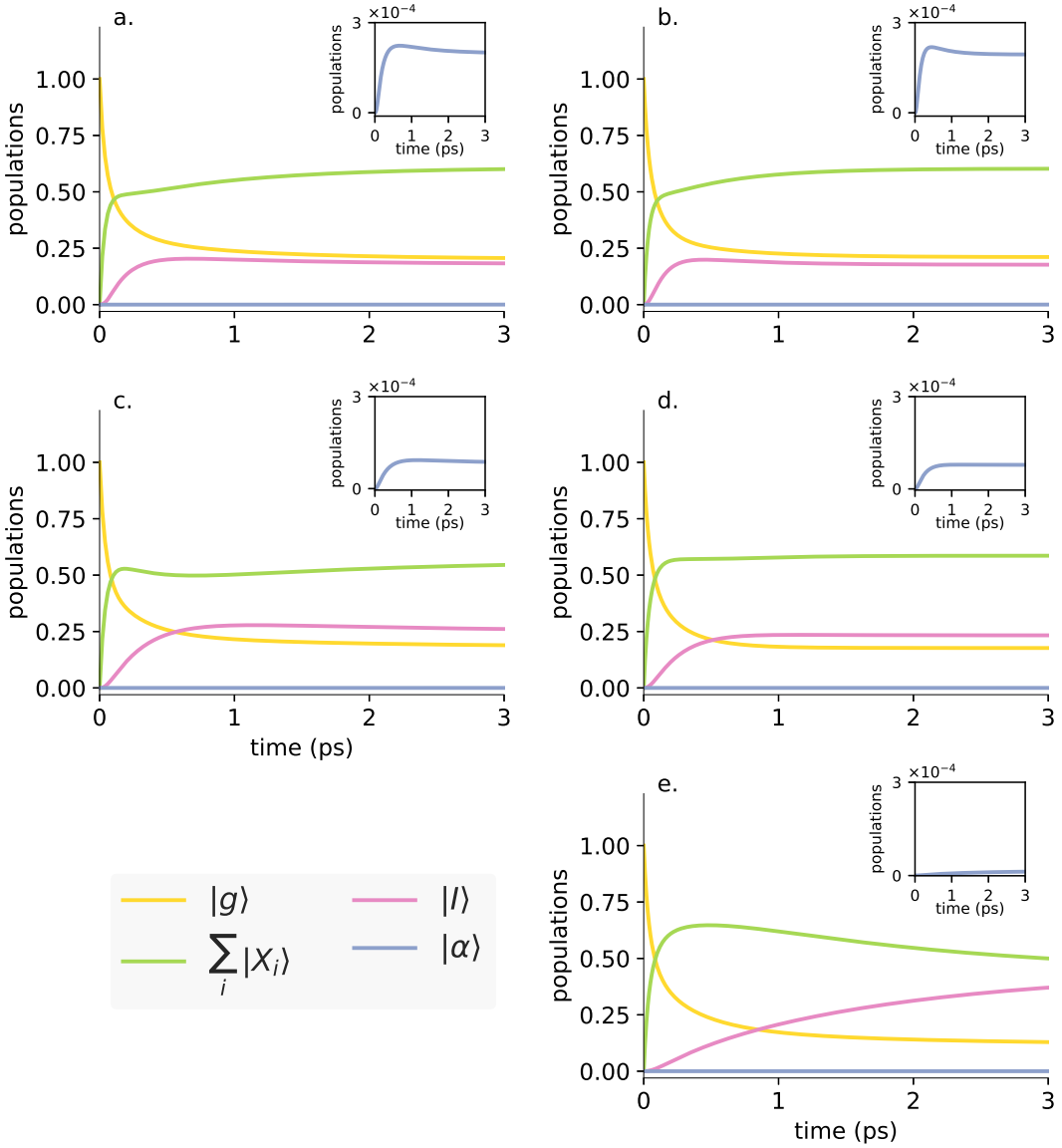

Figure 4.4: Photosystem II reaction centre transient population dynamics. A comparison of the PSIIRC photocell transient population dynamics for the hybrid model and Pauli master equation model using different spectral densities. (a) Drude spectral density $J_D(\omega)$ for the hybrid model, (b) Drude spectral density $J_D(\omega)$ for the Pauli model. (c) Single mode spectral density $J_1(\omega)$ for the hybrid model, (d) Single mode spectral density $J_1(\omega)$ for the Pauli model. (e) Full spectral density $J(\omega)$ for the Pauli model. The inset in each plot shows the population of the secondary charge transfer state $|\alpha\rangle$. The populations of the exciton states are summed to simplify the presentation. The calculations were carried out at temperature $T = 300K$ and excitation rate $\gamma_{ex} = 75cm^{-1}$.

between these two models is the role played by coherences between excitons. Coherences are not accounted for in the Pauli model using modified Redfield theory, while they are in the hybrid model. The coherence dynamics of the hybrid model for spectral densities $J_D(\omega)$ and $J_1(\omega)$ is shown in Fig. 4.5. This figure demonstrates

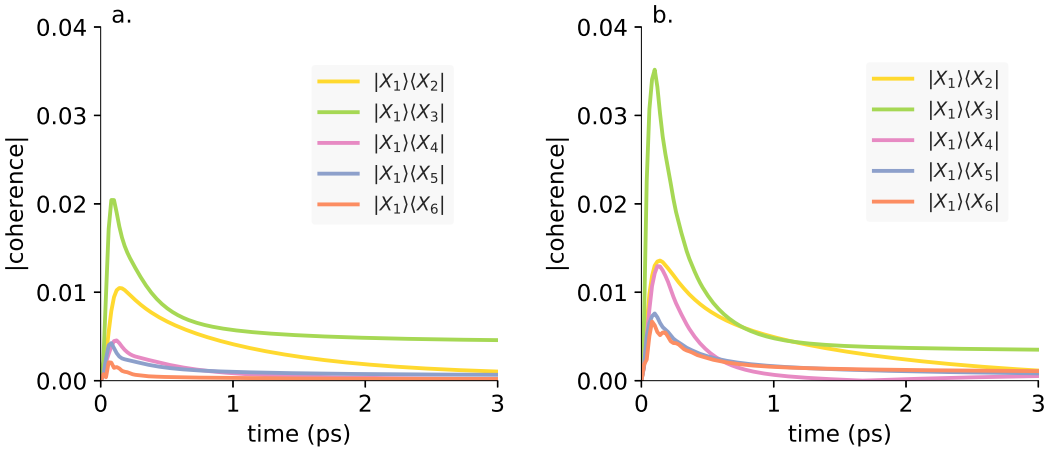

Figure 4.5: Photosystem II reaction centre transient coherence dynamics. The transient dynamics for a selection of the coherences within the exciton manifold of the PSIIRC photocell are shown for the hybrid model using spectral densities (a) $J_D(\omega)$ and (b) $J_1(\omega)$. The calculations were carried out at temperature $T = 300K$ and excitation rate $\gamma_{ex} = 75cm^{-1}$.

that the coherences decay to their steady state within 3ps and are small enough that the Pauli model can be used with confidence that it will capture the important features of the steady state with the full spectral density $J(\omega)$.

For the incoherent rates of electron tunnelling between the source lead of the system a value of $\Gamma_L = 201.6\text{cm}^{-1}$ was fixed for all calculations. The rate to tunnel from the system into the drain lead (Γ_R) was varied for the current and Fano factor calculations as a function of voltage. For calculations varying voltage with a constant excitation rate, the value $\gamma_{ex} = \gamma n = 75\text{cm}^{-1}$ where $\gamma = 0.00125\text{cm}^{-1}$ and $n = 60000$ were used to simulate excitation by concentrated solar radiation [16, 17]. Satisfying detailed balance the deexcitation rate $\gamma_{deex} = \gamma(n+1)$.

4.4 Current and Power

We first characterise the performance of the photocell by calculating the mean current and power output of the device. The generated steady-state current passing between the system and drain electrode is equivalent to the current flowing across a hypothetical load connecting the final states $|\alpha\rangle$ and $|\beta\rangle$, which have an associated energy gap $E_{\alpha\beta} = E_\alpha - E_\beta$. The voltage V across such a load quantifies the extractable energy from the photocell with energy gap $E_{\alpha\beta}$. An expression for V can be derived following standard thermodynamic considerations of photocells [95] and photochemical systems [96]. Denoting the steady state population of the secondary

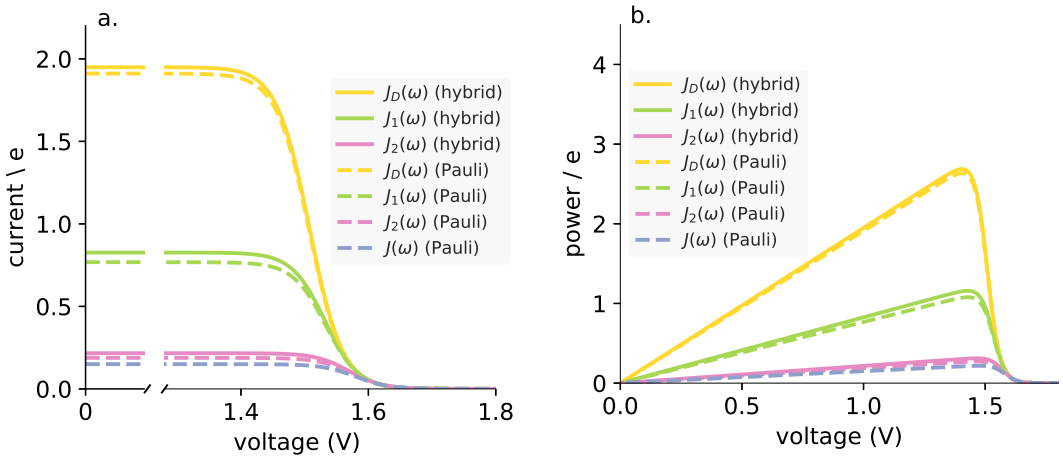

Figure 4.6: Photocell mean current and power versus voltage for different spectral densities. (a) Current. (b) Power. Solid lines are calculated using hybrid model while dashed lines are calculated using the Pauli master equation model. Calculations were carried out at $T = 300K$ with excitation rate $\gamma_{ex} = 75\text{cm}^{-1}$.

CT state $\rho_{\alpha\alpha}$ and the 'empty' state $\rho_{\beta\beta}$, the load voltage V is

$$eV = E_{\alpha\beta} + k_B T \ln\left[\frac{\rho_{\alpha\alpha}}{\rho_{\beta\beta}}\right], \tag{4.3}$$

where k_B is the Boltzmann constant, T the temperature of the photocell and e the electric charge. The average current $\langle I \rangle$ and the power output P delivered by the photocell are given by $\langle I \rangle = e\Gamma_R \rho_{\alpha\alpha}$ and $P = \langle I \rangle V$. By fixing all parameters except the rate Γ_R at which electrons leave the system, the characteristic $\langle I \rangle - V$ and $P - V$ curves which define the photovoltaic performance of a photocell can be investigated.

The current and power curves for the hybrid and Pauli frameworks are shown in Fig. 4.6. For the spectral densities $J_D(\omega)$, $J_1(\omega)$ and $J_2(\omega)$ the results are presented for both frameworks. The close agreement between the models is consistent with the population dynamics shown in Fig. 4.4 and further demonstrates the suitability of Pauli model in describing charge transfer along the Chl_{D1} pathway. The current and power for the Pauli model including the full spectral density $J(\omega)$ is also shown. In the limit $\Gamma_R \to 0$ the current goes to zero and the maximum voltage obtainable in the open circuit limit is reached. In the opposite limit the voltage tends to zero as $\Gamma_R \to \infty$. In these two extremes the photocell delivers no power. For all

spectral densities the current is constant at low voltages and drops off at a characteristic voltage V. When the spectral density is $J_D(\omega)$ this characteristic voltage is comparable to $E_{\alpha\beta}$.

The main feature to notice in Fig. 4.6 is the reduction of the current as discrete modes are added to the spectral density. This arises because of the difference in the coupling of the excitons and CT states to the vibrational environment. The reorganisation energies of the CT states are much larger than for the excitons due to the scaling factors c_I and c_α. In combination with the weak coupling between the excitons and CT states, this means charge transfer is well described using second order perturbation theory in the electronic coupling to obtain incoherent Förster rates (see Section 2.1.2.3). These rates depend on the overlap between the donor "fluorescence" and acceptor "absorption" line shapes. The expressions for these line shapes arise during the derivation of Förster theory (see Section 2.1.2.3) even for charge transfer states which have a zero transition dipole moment. Hence we use the terms "absorption" and "fluorescence" in the remainder of this chapter to indicate that the line shapes have the mathematical form of absorption and fluorescence spectra though there is no photon absorption or emission involved in the transfer process. Changing the reorganisation energy of the donor or acceptor changes the relative position and the broadening of the line shape peaks. Taking the primary charge transfer step from the exciton manifold to the primary CT state as an example, as more modes are added to the spectral density the reorganisation energy of the primary CT state increases at a faster rate relative to the excitons due to the scaling factor c_I. For forward transfer this shifts the peak of the CT "absorption" line shape away from the exciton "fluorescence" peak and in spite of the increased broadening of the line shapes, the overlap and consequently the transfer rate decrease. This is illustrated for both primary and secondary charge transfer steps in Fig. 4.7. The line shapes are not individually normalised in order to show the relative amplitudes at which they enter overlap integral.

We can also see the similarity of the current and power predictions for the spectral densities $J_2(\omega)$ and $J(\omega)$. Since the two modes in $J_2(\omega)$ span a wide range

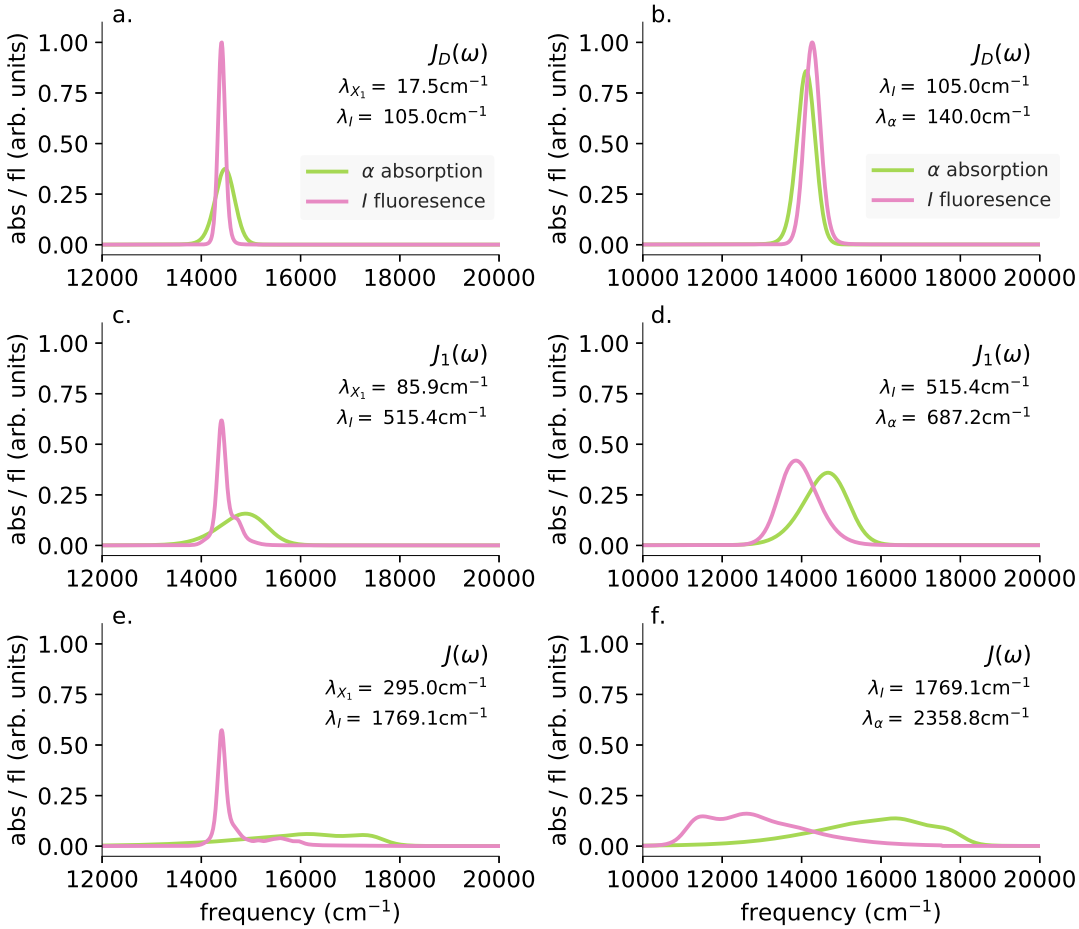

Figure 4.7: Spectral overlap of donor and acceptor lineshapes. The donor "fluorescence" and acceptor "absorption" lineshapes for chromophores involved in primary and secondary charge transfer are shown using spectral densities $J_D(\omega)$, $J_1(\omega)$ and $J(\omega)$. (a,c,e) "Fluorescence" lineshape of exciton $|X_1\rangle$ and "absorption" lineshape of the intermediate charge transfer state $|I\rangle$. (b,d,f) "Fluorescence" lineshape of the intermediate charge transfer state $|I\rangle$ and "absorption" lineshape of the secondary charge transfer state $|\alpha\rangle$.

of frequencies of the electronic system and overlap with many modes from the full spectral density it should not be surprising that $J_2(\omega)$ provides a good approximation of $J(\omega)$ for the current and power calculations.

From these current and power results we can see that the PSIIRC photocell is not necessarily well suited to maximising its power output as a result of coupling to discrete underdamped vibrations. We may therefore put forward a design principle for the development of an ideal pigment-protein based photocell: decoupling electronic degrees of freedom from underdamped modes may reduce the difference in reorganisation energy between exciton and charge transfer states, therefore increasing the charge transfer rates and consequently the current output of the photocell.

Electron-vibrational decoupling has recently been achieved for specific vibrational frequencies of organic molecules embedded in an optical cavity [97, 98]. In terms of biological function the reduction of power output of this theoretical device on increasing reorganisation energy does not present an inconsistency with the observed high quantum yield of charge separation *in vivo*. The important thing for efficient charge separation in PSIIRC is inhibiting charge recombination. Increasing the reorganisation energy of the CT states more than the excitons may lead to a type of Zeno effect where electron transfer is slowed down but once the system is localised in the CT states, backward transfer is inhibited.

4.5 Current Fluctuations

Full characterisation of the performance of a nano-electronic device cannot be limited to the mean current alone. Higher order cumulants of the current also contain information on the dynamical behaviour of electron transfer. In particular the second order cumulant quantifying the current fluctuations can carry signatures of the electronic energy level structure of the system [99], the vibrational environment [64] and quantum coherent effects [62].

The current fluctuations for the photocell are investigated for both the hybrid and Pauli frameworks. For the hybrid approach the non-perturbative counting statistics method developed in Chapter 3 is used, while the Markovian theory of counting statistics (see Section 2.2.1) is used with the Pauli model. Electron transfer between the system and the leads can be described using a Lindblad dissipator in both cases where the assumptions of weak system-lead coupling and constant density of states of the lead are used [76, 75]. There are questions over the validity of assuming that the leads only couple to the electronic system in the hybrid model. Due to the potentially strong electron-phonon coupling we may need to take into account that the leads couple to mixed vibronic states. The consequences of this are still to be investigated for the photocell model presented here, though meaningful insights have been drawn when this assumption has been applied in similar situations [74, 100]. In the following, the second order Fano factor $F^{(2)}$ from Eq. (2.52) is used to quantify

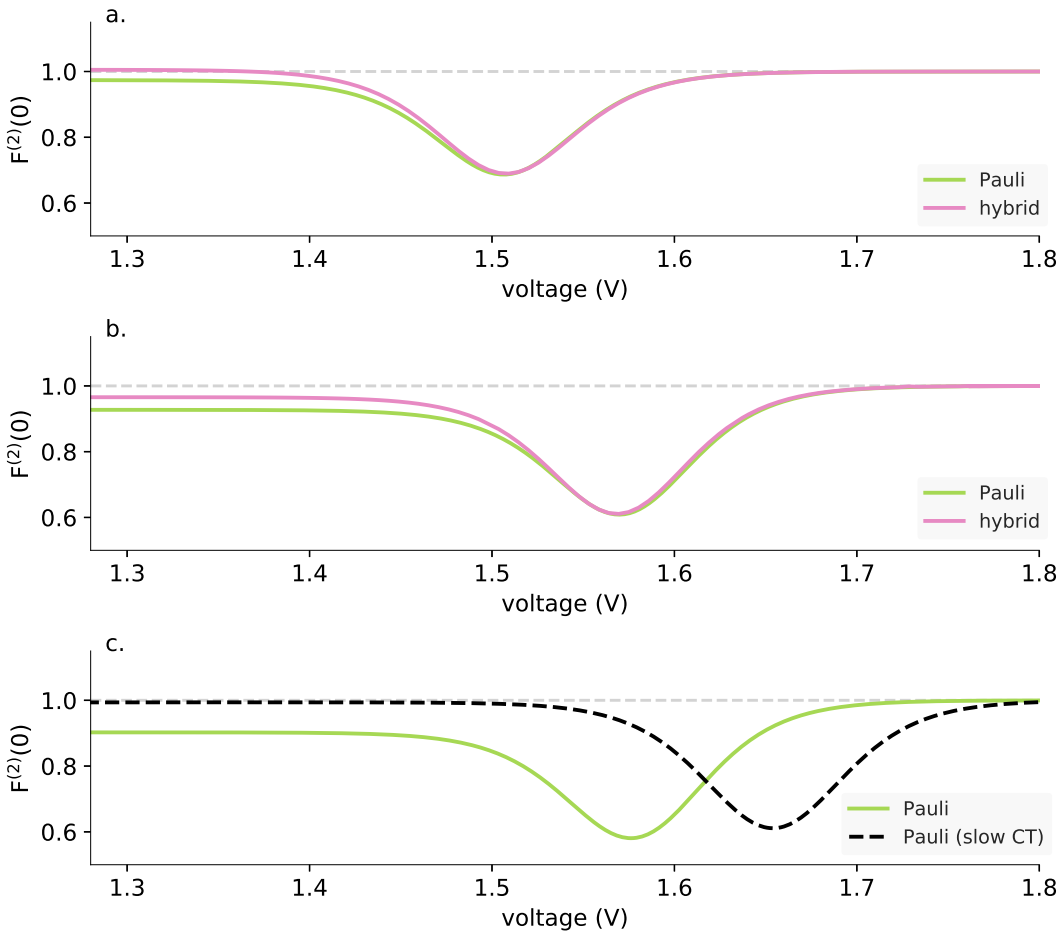

Figure 4.8: Fano factor versus voltage for PSIIRC photocell model. (a) Fano factor for the PSIIRC photocell with spectral density $J_D(\omega)$. (b) Fano factor for the PSIIRC photocell with spectral density $J_2(\omega)$. (c) Fano factor for the PSIIRC photocell with the structured spectral density $J(\omega)$ for the measured (solid line) secondary charge transfer rate and a reduced (dotted line) secondary charge transfer rate. All calculations were carried out at $T = 300K$ with excitation rate $\gamma_{ex} = 75\text{cm}^{-1}$.

the current fluctuations. Deviations from one indicate correlated electron transport, with $F^{(2)} > 1$ a sign of super-Poissonian statistics or 'unordered' electron transport, and $F^{(2)} < 1$ giving sub-Poissonian statistics or 'ordered' transport.

The Fano factor is shown as a function of voltage in Fig. 4.8 for the spectral densities $J_D(\omega)$, $J_2(\omega)$ and $J(\omega)$ at room temperature. The Fano factor for spectral density $J_1(\omega)$ is omitted to simplify the presentation. The similarity of the $F^{(2)}$ curves for the hybrid and Pauli frameworks with spectral densities $J_D(\omega)$ and $J_2(\omega)$ indicates that the current fluctuations are dominated by the populations, similar to the behaviour of the current and power. The coherences decay on a time scale much faster than steady state is reached so would not be expected to play much of a role

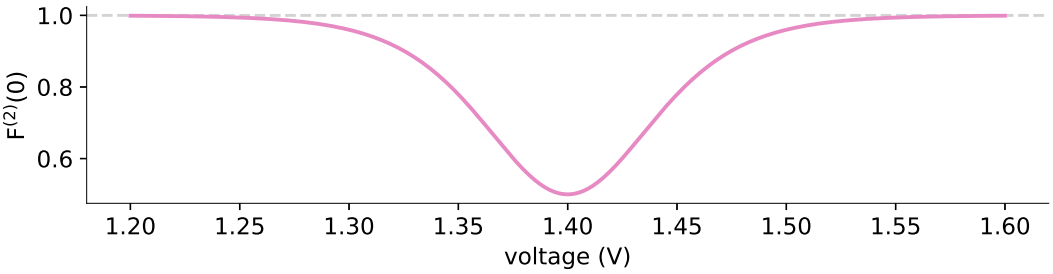

Figure 4.9: Fano factor versus voltage for a single resonant level. Calculations were carried out with an energy gap between the empty and occupied states of $1.4eV$ and a temperature of $300K$.

in the hybrid model results. This is further evidence that the photocell dynamics is well captured by the Pauli framework. For each spectral density the Fano factor is asymmetric around a minimum. At large voltages the Fano factor increases to 1 as the current drops to zero, demonstrating that as the waiting time between electron tunnelling events into the drain lead increases, subsequent electron tunnelling events become uncorrelated. The asymmetry in the Fano factor arises from the multi-state energy level structure of the photocell meaning that an electron always spends a finite amount of time in the system, no matter how fast the rate Γ_R to leave the system becomes. For comparison, the $F^{(2)} - V$ curve for a single resonant level is shown in Fig. 4.9 which is symmetric about a minimum. Similarly to the photocell, for a large voltage (small Γ_R) the Fano factor of the single resonant level tends to one. However, in contrast, for small voltages (large Γ_R) the Fano factor also tends to one as the length of time electrons spend in the system becomes infinitesimal. With multiple energy levels in the photocell, an electron always occupies the system for a finite amount of time providing an opportunity for correlations to appear between subsequent electrons even when Γ_R is large.

The most important feature to notice in Fig. 4.8 is the reduction in the Fano factor as more modes are added to the spectral density. This is associated with the decrease in the current as the reorganisation energy of the electronic states increases. The more 'ordered' transport observed for spectral densities with discrete modes relies on the rapid population of higher energy excitons induced by these structured vibrational environments. The rates of transport to CT states, while reduced, are

still comparable to the transfer among excitons such that the statistics of transition from states $|\alpha\rangle$ to $|\beta\rangle$ samples the manifold of exciton states donating population to the primary CT state. This hypothesis is supported by an analysis of the energy scale determining the voltage at which $F^{(2)}$ is minimum for each spectral density used in Fig. 4.8.

The analytic form of the Fano factor for the photocell model is too complicated to give any insight into the conditions determining the minima Fano factor for the photocell model. In order to understand the minimum in each curve it is again useful to consider the case of a single resonant level (SRL) in the infinite bias limit [33]. The dynamics of this system in the basis $\{|\text{occupied}\rangle, |\text{empty}\rangle\}$ is governed by a Liouvillian with matrix elements $\mathcal{L}_{11} = -\mathcal{L}_{21} = \Gamma_R$ and $\mathcal{L}_{22} = -\mathcal{L}_{12} = \Gamma_L$ where Γ_R is the rate for transfer between the SRL and the drain lead, and Γ_L is the rate for transfer between the source lead and the SRL. The Fano factor as a function of the voltage across a load linking the occupied and empty states takes the form

$$F^{(2)}(V) = \frac{1+\exp[-2(eV-E_0)/k_BT]}{(1+\exp[-(eV-E_0)/k_BT])^2}, \tag{4.4}$$

where E_0 is the energy gap between the occupied and empty states. This expression is equivalent to writing the well known form of the SRL Fano factor in terms of Γ_L and Γ_R as $F^{(2)} = \frac{\Gamma_L^2+\Gamma_R^2}{(\Gamma_L+\Gamma_R)^2}$. Figure 4.9 shows that $F^{(2)}(V)$ for the SRL exhibits a single minimum, just as in the PSIIRC photocell. The minimum occurs when $V_{min} = E_0$ which is equivalent to the condition of $\Gamma_L/\Gamma_R = \rho_{\text{occupied}}/\rho_{\text{empty}} = 1$. In this case, however, the function is symmetric about V_{min} approaching 1 at both large and small voltages and indicating that electron transfer events in these extremes are uncorrelated. Based on this, it is reasonable to propose that near V_{min} the Fano factor of the photocell is approximately equal to that of an effective SRL with occupied level $|\alpha^*\rangle$, empty level $|\beta\rangle$ and renormalised energy gap $E^*_{\alpha\beta}$ that determines V_{min}. Denoting as E_{jk} the energy gap between states $|j\rangle$ and $|k\rangle$ of our photocell, for the case of $J_D(\omega)$ the Fano factor has a minimum for $V_{min} \approx E_{I\beta} \approx 1.50$eV while for the full spectral density $V_{min} \approx E_{X_6\beta} \approx 1.56$eV and for the two mode spectral density $J_2(\omega)$ it takes a value in between. This indicates that in the photocell with the full

spectral density, the minimum Fano factor samples the largest energy gap between $|\beta\rangle$ and the exciton manifold while for $J_D(\omega)$ the Fano factor only witnesses the energy gap up to the intermediate CT state. This is consistent with the fact that the rate of transfer among excitons in the $D1$ branch are larger for $J(\omega)$ than for the other two spectral densities.

As mentioned above, one of the most important features of Fig. 4.8 is the asymmetry of the Fano factor around V_{min}. The rate limiting this asymmetric behaviour is the secondary charge transfer rate. To emphasise this, the secondary CT rate $k_{I,\alpha}$ is set to a very low value compared to relaxation rates within the exciton manifold and the rates between the excitons and primary CT state for the full spectral density. In this case, the population of $|\alpha\rangle$ is so slow that all the internal transfers from the exciton manifold to the primary CT can be described as a single step process i.e. there is no sampling of the exciton manifold and the Fano factor tends to 1 for small and larger voltages as shown by the dotted line in Fig. 4.8 (a). This means that the system behaves as a SRL for all values of V with renormalised Γ_L^* (compare Fig. 4.8 (a) and (d)).

Though there has been no experimental observation of coherent primary charge transfer along the Chl_{D1} pathway, it would be interesting to see if the general trend of decreasing current and Fano factor with increasing reorganisation energy observed for the photocell model remains when the primary charge transfer process is included into the non-perturbative part of the hybrid model. To test this, the primary CT state $|I\rangle$ was included into the system Hamiltonian H_{el} described by the hierarchical equations of motion, with incoherent Förster rates describing charge transfer to the secondary CT state $|\alpha\rangle$. Figure 4.10 (a) and (b) shows the current and Fano factor respectively as a function of voltage for a photocell described by the coherent CT hybrid model. The structureless Drude ($J_D(\omega)$) and the single mode ($J_1(\omega)$) spectral densities are compared and the trend for decreasing current and Fano factor as a discrete mode is added to the spectral density is indeed observed. Interestingly the Fano factor is clearly super-Poissonian for low voltages which is likely due to the existence of competing trajectories for a state to take through the

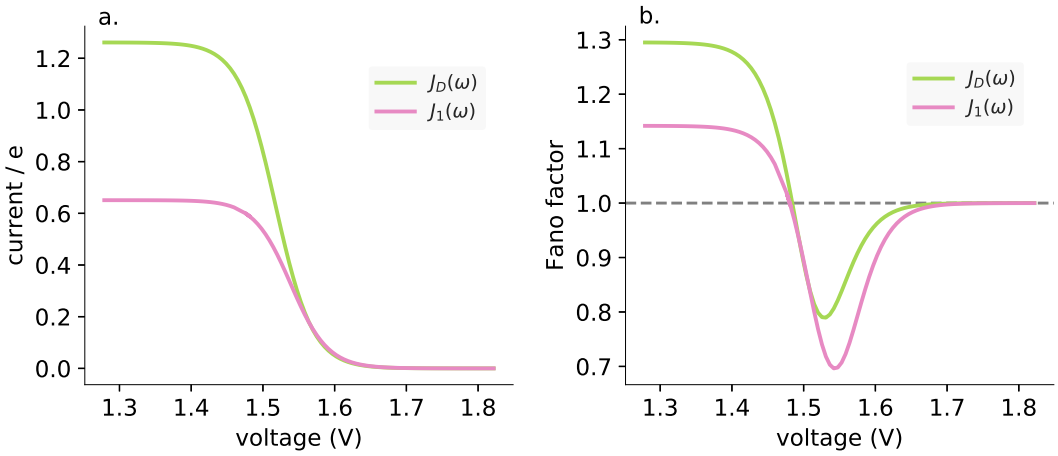

Figure 4.10: Photocell current and Fano factor for coherent primary charge transfer. (a) Current and (b) Fano factor as a function of voltage for the hybrid model comparing spectral densities $J_D(\omega)$ and $J_1(\omega)$. The calculations were carried out at temperature $T = 300K$ and excitation rate $\gamma_{ex} = 75cm^{-1}$.

system. If there is a large difference in the time scales for different trajectories then this super-Poissonian behaviour may be a manifestation of the dynamical channel blockade [63].

From the perspective of nano-electronics, a reduction in the fluctuations of the output current would be a desirable feature. For the case of the photocell model, the reduction of the Fano factor as underdamped modes are added to the spectral density delivers the function of an improved precision of the current. But does this reduction in current fluctuations have any advantage in a biological setting? Noise and its control is crucial across all scales in biology [101, 102]. For instance, biochemical processes that are inherently stochastic include mechanisms to control intrinsic noise and in particular to reduce it for regulatory processes [102]. Electron transfer events in photosynthetic reaction centres belong to a larger family of stochastic transport processes in biology, some of which have already been predicted to exhibit mechanisms suppressing fluctuations below the Poissonian level [103]. Furthermore, increased complexity in biological networks has been linked to intrinsic noise reduction [104]. We can therefore make the argument that coupling to well-resolved vibrations and the predicted noise reduction may have a regulatory function for the biological function of PRCs. In these systems, the final stable CT state $|\alpha\rangle$ donates an electron to quinone B and once this reduction happens, the PRC

is unable to handle an excitation for a finite 'blocking' time. Having single electrons delivered at regular (ordered) time intervals (with narrower fluctuations of waiting times) could avoid wasting excitations that may arrive at the reaction centre during an overly long blocking period where the time intervals fluctuate greatly around the mean.

4.6 Summary and Conclusions

We have constructed a theoretical photocell model inspired by the photosystem II reaction centre. We calculated the current and power output of this device for different vibrational environments and a reduction in the current output was observed as more discrete modes were added to the spectral density. This current reduction was accompanied by a reduction in the Fano factor which signals a decrease in the current fluctuations. We then discussed the relevance of these findings for the design of artificial photocells constructed using bio-molecular components, and for the *in vivo* biological function of the reaction centre.

Realistically, it is unlikely that photosynthetic reaction centres will be used as components in photocell devices, though the study presented here has highlighted some desirable features of artificial photocells we might want to engineer. Photosynthetic proteins are susceptible to irreversible photodamage when isolated from the repair processes occurring *in vivo*. In PSIIRC this damage occurs in the D1 protein resulting in a lifetime as short as tens of minutes [22, 105]. Emerging organic alternatives, such as the synthesis of protein maquettes [106] has opened the possibility of building artificial units mimicking the structure of photosynthetic systems but with enhanced photostability.

Chapter 5

Reorganisation Energy Asymmetry in Photosynthetic Reaction Centres

Charge separation in photosynthetic reaction centres has been widely studied in recent years. Advances in non-linear spectroscopy have allowed for a detailed picture of the primary charge transfer dynamics to emerge which seems to involve quantum coherent charge transfer along at least one of the charge separation pathways in the photosystem II reaction centre. The photosynthetic reaction centre has also been an inspiration for the study of theoretical photocell devices, where the effect of certain features of this system on the photocell performance are investigated. In this chapter we look at the difference in electron-phonon coupling for charge transfer states and excitation states by studying the dynamics of a dimer system as well as a bio-inspired photocell model. In particular we investigate parameter regimes having certain characteristics of the two charge separation pathways in the photosystem II reaction centre.

5.1 Exciton and Charge Transfer States in Photosynthetic Reaction Centres

The first stage of photosynthesis involves capture of energy from solar radiation by specialised light-harvesting antenna complexes. Photons are absorbed by chromophores to form collective excited states called excitons. The energy is then transferred to a photosynthetic reaction centre (PRC) where coupling to charge transfer

(CT) states initiates a charge separation process. Ultimately the energy is stored as an electrochemical gradient across a membrane.

Though PRCs are often comprised of the same chromophores as light-harvesting antennae, their different biological function requires a radically different structure. The coupling between exciton and CT states is achieved by the tight packing of the core PRC chromophores since the exciton-CT coupling depends strongly on wavefunction overlap [107, 15]. The 6 core chromophores in the photosystem II reaction centre (PSIIRC) are packed into a volume of $\sim 30^3 \text{Å}^3$ [44].

Chromophores can be simply modelled as two level systems when considering only single excitation states. In the ground state a chromophore has an electron in the highest occupied molecular orbital (HOMO) while the lowest unoccupied molecular orbital (LUMO) is empty. Single excited states are reached by a transition of the electron from the HOMO to the higher energy LUMO leaving a positively charged hole in the HOMO [44, 45]. Exciton states involve superpositions of these individual excited states across several chromophores. Charge transfer states on the other hand form when an electron in the excited state moves onto an adjacent chromophore leaving a hole on the donor and an excess electron on the acceptor where both the HOMO and LUMO are occupied [44, 45]. The equivalent state could also be formed through movement of the hole. A schematic representation of excitation and charge transfer states is shown in Fig. 2.2.

There are several features of CT states that differentiate them from exciton states. Firstly, CT states are optically dark unless there is some coherent mixing with exciton states [15, 108, 7]. CT states also have a permanent dipole moment which introduces a strong Stark effect into the linear spectra of PRC complexes [15, 108, 109]. This permanent dipole leads to a larger reorganisation energy of the CT states relative to exciton states due to a stronger coupling with fluctuations of the phonon bath.

In the modelling of the linear and non-linear spectra of PSIIRC, this increased system-bath coupling of CT states is generally introduced through a scaling of the CT state reorganisation energy [46, 109, 47, 7, 8]. These models assume the CT

states to be localised electronic states coupled to local, independent phonon baths. There have been PSIIRC models proposed that explicitly model the CT states by including the electrostatic interaction between electrons and holes [44, 45]. Some of these models also consider correlations between the CT state phonon bath and those of the exciton states occupying chromophores across which the charge is separated [45]. However in this chapter we will take the approach of Ref. [47] and treat CT states as localised electronic states coupled to a local phonon environment.

5.2 Asymmetric Coupling to Coherent Modes

To gain some insight into the physics of the increased system-bath coupling of CT states, we look at a simple dimer system where each site is coupled to an independent coherent mode. The electron-mode coupling of the sites will be asymmetric while the mode frequencies will be identical. The Hamiltonian of the total system is

$$\begin{aligned} H = \varepsilon_1^{(0)}|1\rangle\langle 1| + \varepsilon_2^{(0)}|2\rangle\langle 2| + J(|1\rangle\langle 2| + |2\rangle\langle 1|) \\ + \frac{1}{2}\omega_1^2(\hat{q}_1 - d_1)^2|1\rangle\langle 1| + \frac{1}{2}\omega_2^2(\hat{q}_2 - d_2)^2|2\rangle\langle 2| + \frac{1}{2}\hat{p}_1^2 + \frac{1}{2}\hat{p}_2^2 \end{aligned} \quad (5.1)$$

where the unshifted energy splitting in the site basis is $\Delta\varepsilon = \varepsilon_1^{(0)} - \varepsilon_2^{(0)}$, the position operator of the mode coupled to state $|n\rangle$ is $\hat{q}_n$ while the momentum operator is $\hat{p}_n$ and the displacement of mode n relative to the ground state configuration is d_n. In the following we set $\hbar = 1$ to simplify the presentation.

We introduce the increased coupling of site $|2\rangle$ to its mode through a scaling factor c such that $d_2 = \sqrt{c}d_1$. Assuming the mode frequencies are the same $\omega_1 = \omega_2 = \omega$ the Hamiltonian can be rewritten

$$\begin{aligned} H = \varepsilon_1^{(0)}|1\rangle\langle 1| + \varepsilon_2^{(0)}|2\rangle\langle 2| + J(|1\rangle\langle 2| + |2\rangle\langle 1|) \\ + \frac{1}{2}\omega^2 d_1^2|1\rangle\langle 1| + c\frac{1}{2}\omega^2 d_1^2|2\rangle\langle 2| \\ + \frac{1}{2}\omega^2\hat{q}_1^2|1\rangle\langle 1| + \frac{1}{2}\omega^2\hat{q}_2^2|2\rangle\langle 2| \\ - \omega^2\hat{q}_1 d_1|1\rangle\langle 1| - \sqrt{c}\omega^2\hat{q}_2 d_1|2\rangle\langle 2| + \frac{1}{2}\hat{p}_1^2 + \frac{1}{2}\hat{p}_2^2 \end{aligned} \quad (5.2)$$

The site reorganisation energy due to interaction with the mode is $\lambda = \frac{1}{2}\omega^2 d_1^2$ which is now scaled by the factor c for site $|2\rangle$. By introducing the dimensionless displacement $D_1 = -\sqrt{\frac{\omega}{2}}d_1$ we can rewrite the reorganisation energy in terms of the Huang-Rhys factor of the mode $S = \frac{D_1^2}{2}$ obtaining $\lambda = \omega S$. The Huang-Rhys factor is related to the displacement of the equilibrium position of a potential energy surface relative to the ground state and is experimentally accessible through measurements of the Stokes shift [43]. Now incorporating the reorganisation energy into the site energies we get

$$\begin{aligned} H = &\left(\varepsilon_1^{(0)}+\lambda\right)|1\rangle\langle 1| + \left(\varepsilon_2^{(0)}+c\lambda\right)|2\rangle\langle 2| + J(|1\rangle\langle 2| + |2\rangle\langle 1|) \\ &+\frac{1}{2}\omega^2\hat{q}_1^2|1\rangle\langle 1| + \frac{1}{2}\omega^2\hat{q}_2^2|2\rangle\langle 2| \\ &-\omega^2\hat{q}_1 d_1|1\rangle\langle 1| - \sqrt{c}\omega^2\hat{q}_2 d_1|2\rangle\langle 2| + \frac{1}{2}\hat{p}_1^2 + \frac{1}{2}\hat{p}_2^2 \end{aligned} \tag{5.3}$$

We can now see that when $c \neq 1$ the energy splitting of the sites will be different from the unshifted splitting $\Delta\varepsilon$. Writing the position and momentum operators in terms of the bosonic creation and annhilation operators $\hat{q}_n = \frac{1}{\sqrt{2\omega}}(b_n + b_n^\dagger)$ and $\hat{p}_n = -i\sqrt{\frac{\omega}{2}}(b_n - b_n^\dagger)$ [43] the Hamiltonian takes the well known form

$$\begin{aligned} H = &\left(\varepsilon_1^{(0)}+\lambda\right)|1\rangle\langle 1| + \left(\varepsilon_2^{(0)}+c\lambda\right)|2\rangle\langle 2| + J(|1\rangle\langle 2| + |2\rangle\langle 1|) \\ &+\omega\left(b_1^\dagger b_1 + \frac{1}{2}\right) + \omega\left(b_2^\dagger b_2 + \frac{1}{2}\right) \\ &+g|1\rangle\langle 1|(b_1^\dagger + b_1) + \sqrt{c}g|2\rangle\langle 2|(b_2^\dagger + b_2) \end{aligned} \tag{5.4}$$

where the mode coupling strength is $g = -\frac{\omega^2}{\sqrt{2\omega}}d_1 = \omega D_1 = \omega\sqrt{S}$ and is scaled by the factor $\sqrt{c}$ for site $|2\rangle$.

Now diagonalising the electronic part of the Hamiltonian using $|1\rangle = \alpha|X_1\rangle + \beta|X_2\rangle$ and $|2\rangle = \beta|X_1\rangle + \alpha|X_2\rangle$ the part of the Hamiltonian containing interaction

terms between the electronic and vibrational subsystems becomes

$$H_I = g\Big[|X_1\rangle\langle X_1|(\alpha^2 B_1+\sqrt{c}\beta^2 B_2)+|X_2\rangle\langle X_2|(\beta^2 B_1+\sqrt{c}\alpha^2 B_2) \\ +\alpha\beta(|X_1\rangle\langle X_2|-|X_2\rangle\langle X_1|)(B_1-\sqrt{c}B_2)\Big] \tag{5.5}$$

where $B_n = b_n^\dagger + b_n$. Transforming the coherent modes to the centre of mass (CM) and relative displacement (RD) basis such that

$$b_{CM}^{(\dagger)} = \frac{b_1^{(\dagger)}+\sqrt{c}b_2^{(\dagger)}}{\sqrt{1+c}} \qquad b_{RD}^{(\dagger)} = \frac{b_1^{(\dagger)}-\sqrt{c}b_2^{(\dagger)}}{\sqrt{1+c}} \tag{5.6}$$

which obey the usual bosonic commutation relations $[b_{CM}, b_{CM}^\dagger] = [b_{RD}, b_{RD}^\dagger] = 1$ and $[b_{CM}, b_{RD}^\dagger] = [b_{RD}, b_{CM}^\dagger] = 0$, the interaction Hamiltonian can be written

$$H_I = \frac{g\sqrt{1+c}}{2}\Big\{|X_1\rangle\langle X_1|[\alpha^2(B_{CM}+B_{RD})+\beta^2(B_{CM}-B_{RD})] \\ +|X_2\rangle\langle X_2|[\beta^2(B_{CM}+B_{RD})+\alpha^2(B_{CM}-B_{RD})] \\ +2\alpha\beta(|X_1\rangle\langle X_2|+|X_2\rangle\langle X_1|)B_{RD}\Big\} \tag{5.7}$$

where we used $B_1 = \frac{\sqrt{1+c}}{2}(B_{CM}+B_{RD})$ and $B_2 = \frac{\sqrt{1+c}}{2\sqrt{c}}(B_{CM}-B_{RD})$.

For a two level system the coefficients $\alpha = \cos\theta$ and $\beta = \sin\theta$ where the mixing angle θ is a measure of the delocalisation of the electronic system. We will use the delocalisation parameter $\eta = \tan 2\theta = |\frac{2J}{\Delta\varepsilon}|$ later on to quantify the coherent mixing of the electronic states. The interaction Hamiltonian can now be simplified to

$$H_I = \frac{g\sqrt{1+c}}{2}\Big\{(|X_1\rangle\langle X_1|+|X_2\rangle\langle X_2|)B_{CM}+\cos 2\theta(|X_1\rangle\langle X_1|-|X_2\rangle\langle X_2|)B_{RD} \\ +\sin 2\theta(|X_1\rangle\langle X_2|+|X_2\rangle\langle X_1|)B_{RD}\Big\} \tag{5.8}$$

Notice that the centre of mass motion becomes decoupled from the electronic system since the term involving B_{CM} acts only the electronic identity operator. This term becomes part of the mode Hamiltonian H_M which we will discuss shortly.

Now writing terms involving θ in terms of the delocalisation parameter η we get

$$H_I = \frac{g}{2}\frac{\sqrt{1+c}}{\sqrt{1+\eta^2}}\Big\{(|X_1\rangle\langle X_1| - |X_2\rangle\langle X_2|)B_{RD} + \eta(|X_1\rangle\langle X_2| + |X_2\rangle\langle X_1|)B_{RD}\Big\} \quad (5.9)$$

This expression shows explicitly that the electronic system only directly interacts with the shared relative displacement mode. The nature of this interaction depends strongly on the delocalisation of the system. For a fully delocalised system where $\eta \gg 1$, the behaviour is dominated by off-diagonal coupling where the mode modulates the coherences in the eigenstate basis. Conversely in the localised regime where $\eta \ll 1$, the mode causes fluctuations of the eigenstate energy gap. The effect of the asymmetric coupling on the interaction Hamiltonian in the transformed mode basis is a scaling of the interaction with the shared relative displacement mode.

We still need to consider the effect of the asymmetric coupling on the part of the total Hamiltonian in Eq. (5.4) containing terms involving only mode operators. Writing the mode Hamiltonian in the CM/RD basis we get

$$\begin{aligned} H_M = \omega\frac{(1+c)^2}{4c}\left(b_{CM}^\dagger b_{CM} + \frac{1}{2}\right) + \omega\frac{(1+c)^2}{4c}\left(b_{RD}^\dagger b_{RD} + \frac{1}{2}\right) \\ + \frac{g\sqrt{c+1}}{2}\left(b_{CM}^\dagger + b_{CM}\right) + \omega\frac{c^2-1}{4c}\left(b_{CM}^\dagger b_{RD} + b_{RD}^\dagger b_{CM}\right) \end{aligned} \quad (5.10)$$

The first two terms simply give the energies of the modes in the new basis with their frequencies shifted depending on the amount of asymmetry in the coupling. The third term displaces the centre of mass mode with a coupling strength also depending on the asymmetry. There is however an additional term only taking effect when $c \neq 1$ which couples the centre of mass mode to the relative displacement mode. The interaction between the modes takes the form of a phonon exchange providing an opportunity for coherences to appear between the three subsystems. Due to the monogamy of entanglement [110], coherence between the relative displacement and centre of mass modes restricts other coherences in the system. Importantly for electronic transfer, coherence between electronic eigenstates, which is driven by the relative displacement mode, will be restricted. Electronic transfer will therefore be sensitive to the scaling factor c which controls the strength of the coupling to the

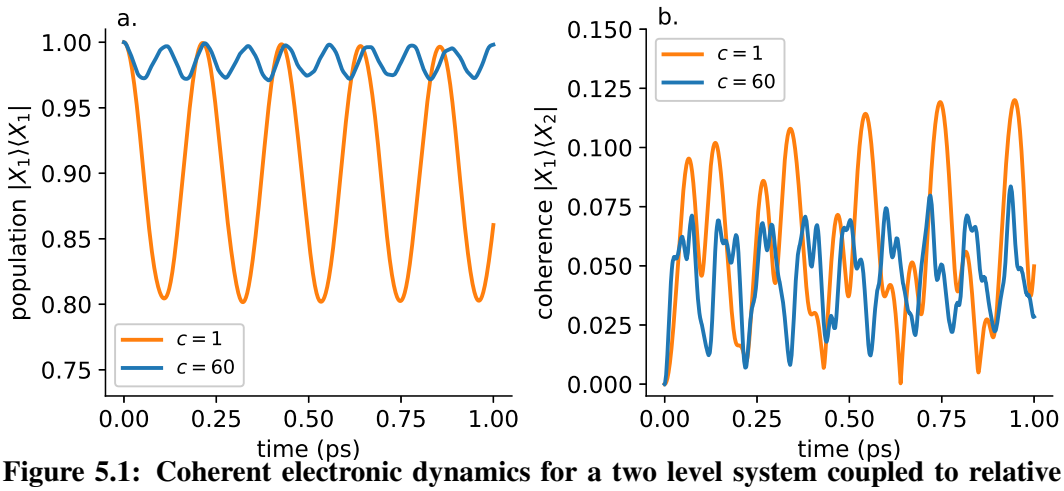

Figure 5.1: Coherent electronic dynamics for a two level system coupled to relative displacement and centre of mass modes. The parameters used are $\Delta\varepsilon = 140\text{cm}^{-1}$, $J = 70\text{cm}^{-1}$, $\omega = 342\text{cm}^{-1}$ and $g = 71.58\text{cm}^{-1}$.

centre of mass mode. In Fig. 5.1 we compare the population and coherence dynamics of the electronic eigenstates under the influence of the total Hamiltonian (5.4) when $c = 1$ and $c > 1$. We can see that when $c > 1$ the coherent electronic transfer from the initial state $|X_1\rangle$ is inhibited due to the restrictions on the electronic coherence.

5.3 Dynamics of a Dimer System With Asymmetric Reorganisation Energy

We now investigate the effect of asymmetric system-bath coupling on the excited state dynamics of a dimer system using the non-perturbative hierarchical equations of motion (see Section 2.1.3). This theoretical framework treats the system-bath dynamics exactly allowing interpolation between different parameter regimes without the need for perturbative approximations.

Similarly to the analysis presented in the previous section, the model we use consists of a pair of two level systems with the electronic Hamiltonian

$$H_{el}^{(0)} = \varepsilon_1^{(0)}|1\rangle\langle 1| + \varepsilon_2^{(0)}|2\rangle\langle 2| + J(|1\rangle\langle 2| + |2\rangle\langle 1|) \tag{5.11}$$

The delocalisation of the electronic levels is quantified by the parameter $\eta = |\frac{2J}{\Delta\varepsilon}|$ where $\Delta\varepsilon = \varepsilon_1^{(0)} - \varepsilon_2^{(0)}$. Generalising the system-bath coupling in Eq. (5.1), each

site is linearly coupled to a sum of normal modes described by the Hamiltonian

$$H_M = \sum_k \frac{1}{2}\omega_{1k}^2(\hat{q}_{1k} - d_{1k})^2|1\rangle\langle 1| + \sum_k \frac{\hat{p}_{1k}^2}{2} + \sum_k \frac{1}{2}\omega_{2k}^2(\hat{q}_{2k} - d_{2k})^2|2\rangle\langle 2| + \sum_k \frac{\hat{p}_{2k}^2}{2} \tag{5.12}$$

As in the previous section we introduce the scaling of the mode displacement for site $|2\rangle$ such that $d_{2k} = \sqrt{c}d_{1k} = \sqrt{c}d_k$. Rewriting H_M in terms of this scaling factor and assuming that vibrational frequencies on each site are equal, ie. $\omega_{1k} = \omega_{2k} = \omega_k$, we obtain

$$\begin{aligned} H_M = \sum_k \frac{1}{2}\omega_k^2 d_k^2|1\rangle\langle 1| + c\sum_k \frac{1}{2}\omega_k^2 d_k^2|2\rangle\langle 2| \\ + \sum_k \frac{1}{2}\omega_k^2 \hat{q}_{1k}^2|1\rangle\langle 1| + \sum_k \frac{1}{2}\omega_k^2 \hat{q}_{2k}^2|2\rangle\langle 2| \\ - \sum_k \omega_k^2 \hat{q}_{1k} d_k|1\rangle\langle 1| - \sqrt{c}\sum_k \omega_k^2 \hat{q}_2 d_k|2\rangle\langle 2| + \sum_k \frac{\hat{p}_{1k}^2}{2} + \sum_k \frac{\hat{p}_{2k}^2}{2} \end{aligned} \tag{5.13}$$

The reorganisation energy of the electronic states due to the phonon bath is defined $\lambda = \sum_k \frac{1}{2}\omega_k^2 d_k^2 = \sum_k \omega_k S_k$ where the dimensionless displacement $D_k = -\sqrt{\frac{\omega}{2}}d_k = \sqrt{S_k}$ has been introduced in terms of the Huang-Rhys factor S_k [43, 93]. The electronic part of the system then becomes

$$H_{el} = (\varepsilon_1^{(0)} + \lambda)|1\rangle\langle 1| + (\varepsilon_2^{(0)} + c\lambda)|2\rangle\langle 2| + J(|1\rangle\langle 2| + |2\rangle\langle 1|) \tag{5.14}$$

The reorganisation energy is the amount of energy that must be dissipated to the bath after a vertical transition between two electronic states in order to relax to the equilibrium configuration of the new electronic state. It is related to the strength of the interaction between an electronic state and its phonon bath. In the present situation we define the reorganisation energy of each excited state relative to the equilibrium configuration of the ground state.

Writing the position and momentum operators in terms of the bosonic creation and annhilation operators $\hat{q}_{nk} = \frac{1}{\sqrt{2\omega_k}}(b_{nk}^\dagger + b_{nk})$ and $\hat{p}_{nk} = -i\sqrt{\frac{\omega_k}{2}}(b_{nk}an - b_{nk}^\dagger)$

[43] the total Hamiltonian takes the well known form

$$\begin{aligned} H = &\Big(\varepsilon_1+\lambda\Big)|1\rangle\langle 1| + \Big(\varepsilon_2 + c\lambda\Big)|2\rangle\langle 2| + J(|1\rangle\langle 2| + |2\rangle\langle 1|) \\ &+ \sum_k \omega_k \Big(b_{1k}^\dagger b_{1k} + \frac{1}{2}\Big) + \sum_k \omega_k \Big(b_{2k}^\dagger b_{2k} + \frac{1}{2}\Big) \\ &+ \sum_k g_k |1\rangle\langle 1|(b_{1k}^\dagger + b_{1k}) + \sqrt{c}\sum_k g_k |2\rangle\langle 2|(b_{2k}^\dagger + b_{2k}) \end{aligned} \tag{5.15}$$

where the mode coupling strength is $g_k = -\frac{\omega_k^2}{\sqrt{2\omega_k}} d_k = \omega_k D_k = \omega_k \sqrt{S_k}$.

The form of the electron-phonon interaction for site $|n\rangle$ can conveniently be expressed in terms of the following function

$$J_n(\omega) = \pi \sum_k g_k^2 \delta(\omega - \omega_k) \tag{5.16}$$

which is known as the spectral density. It quantifies the system-bath interaction over a continuous range of frequencies. We can express the reorganisation energy in terms of $J_n(\omega)$ as $\lambda_n = \pi^{-1} \int_0^\infty d\omega J_n(\omega)/\omega$.

Specific forms of the spectral density can be used depending on the microscopic details of the system-bath interaction. Inspired by primary charge separation in the photosystem II reaction centre we use the sum of a Drude spectral density $J_D(\omega)$ describing low energy fluctuations of the bath, and an underdamped mode $J_M(\omega)$. Though the full PSIIRC spectral density includes 48 underdamped modes, we use this simplified spectral density due to the scaling of the computational requirements of the hierarchical equations of motion as the number of modes increases. The Drude spectral density has the form

$$J_D(\omega) = \frac{2\lambda_D \Omega_D \omega}{\omega^2 + \Omega_D^2} \tag{5.17}$$

where λ_D is the reorganisation energy and Ω_D is the cutoff frequency. The spectral density for the underdamped mode is

$$J_M(\omega) = \frac{2\lambda_M \omega_0^2 \gamma \omega}{(\omega^2 - \omega_0^2)^2 + \gamma^2 \omega^2} \tag{5.18}$$

where ω_0 is the mode frequency, γ is the mode damping constant and $\lambda_M = \omega_0 S$ is the reorganisation energy due to the mode. The asymmetry with respect to the system-bath coupling is introduced by scaling the reorganisation energy of the bath coupled to site $|2\rangle$ by the factor c. Taking parameters from previous PSIIRC models, we use $\lambda_D = 35\text{cm}^{-1}$ and $\Omega_D = 40\text{cm}^{-1}$ for the Drude spectral density [46, 47, 7] and $\omega_0 = 342\text{cm}^{-1}$, $S = 0.0438$ and $\gamma = 10\text{cm}^{-1}$ for the underdamped mode [94, 7] which has been observed to influence charge separation along the P_{D1} pathway [7]. The delocalisation of the electronic states is varied by changing the parameter η while fixing the energy splitting in the unshifted eigenstate basis $\Delta E = \sqrt{\Delta\varepsilon^2 + 4J^2}$. Additionally we consider the cases where ΔE is either resonant ($\Delta E \approx 340\text{cm}^{-1}$) or off-resonant ($\Delta E \approx 200\text{cm}^{-1}$) with the underdamped mode for a fixed delocalisation. This is motivated by the presence of static disorder in photosynthetic pigment-protein complexes [46, 47]. Static disorder varies the energy gaps between electronic states over time scales much longer than for electron transport so different realisations of disorder may have different resonance conditions. It is also easier to control the energy gaps and inter-site couplings rather than mode frequencies in artificial chromophore complexes constructed using techniques such as protein maquettes [106, 111] and DNA origami [112, 113, 114].

Even in its simplicity, this model still allows investigation of a wide range of parameter regimes by varying only the electronic delocalisation η and the reorganisation energy scaling factor c. In particular, we choose parameter regimes having certain characteristics of the two different charge separation pathways in PSIIRC. The existence of two pathways has been proposed as a mechanism to ensure PSIIRC is robust against the effects of static disorder of chromophore energies [87, 47]. These pathways are shown in Fig. 5.2. The P_{D1} pathway starts from the special pair with the primary charge transfer state $P_{D2}^{+}P_{D1}^{-}$. This CT state has significant coherent mixing with the exciton states such that it gains a small transition dipole moment [7]. This makes it possible to investigate the charge transfer dynamics using 2D electronic spectroscopy, a technique which was used to observe quantum coherent charge transfer along the P_{D1} pathway [7, 8]. The Chl_{D1} pathway starts from the ac-

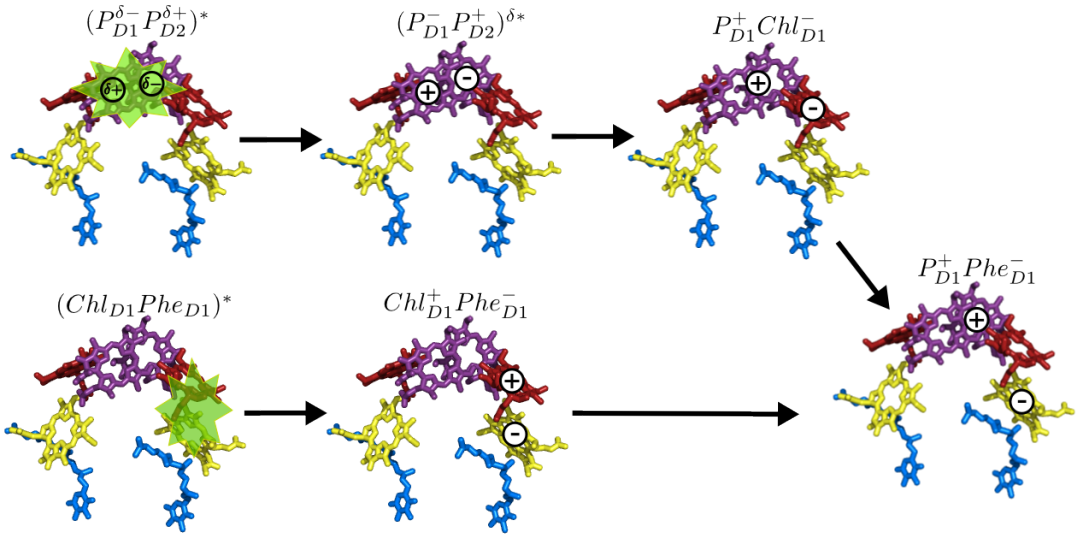

Figure 5.2: Charge transfer pathways in the photosystem II reaction centre. Charge separation is initiated from an exciton quasi-localised on either the special pair or the accessory chlorophyll on the D1 branch.

cessory chlorophyll on the D1 branch with the primary CT state $\mathrm{Chl}_{D1}^{+}\mathrm{Phe}_{D1}^{-}$. This CT state is only weakly coupled to the exciton states so it is essentially optically dark and is treated as a localised state. The electronic parameters used in the dimer model are shown in Table 5.1.

	$\eta = 0.05$	$\eta = 1$
$\Delta E = 200\mathrm{cm}^{-1}$	$\Delta\varepsilon = 200\mathrm{cm}^{-1}, J = 5\mathrm{cm}^{-1}$	$\Delta\varepsilon = 140\mathrm{cm}^{-1}, J = 70\mathrm{cm}^{-1}$
$\Delta E = 340\mathrm{cm}^{-1}$	$\Delta\varepsilon = 340\mathrm{cm}^{-1}, J = 8.5\mathrm{cm}^{-1}$	$\Delta\varepsilon = 240\mathrm{cm}^{-1}, J = 120\mathrm{cm}^{-1}$

Table 5.1: Electronic parameters of resonant/off-resonant and delocalised/localised regimes for a dimer system.

5.3.1 Quasi-Localised Eigenstates

Figure 5.3 shows the population dynamics of the dimer system for quasi-localised electronic eigenstates with a delocalisation parameter $\eta = 0.05$. The dynamics are compared for reorganisation energy scaling $c = 1$ and $c > 1$ such that the condition $\Delta\varepsilon < \lambda(c-1)$ holds. These parameters are representative of those for charge separation along the Chl_{D1} pathway [47]. In order to compare the cases with a resonant and off-resonant mode the parameter $\kappa = \frac{\Delta\varepsilon}{\lambda(c-1)}$ is kept fixed. Since the unscaled reorganisation energy λ is also held constant, the factor c is varied with

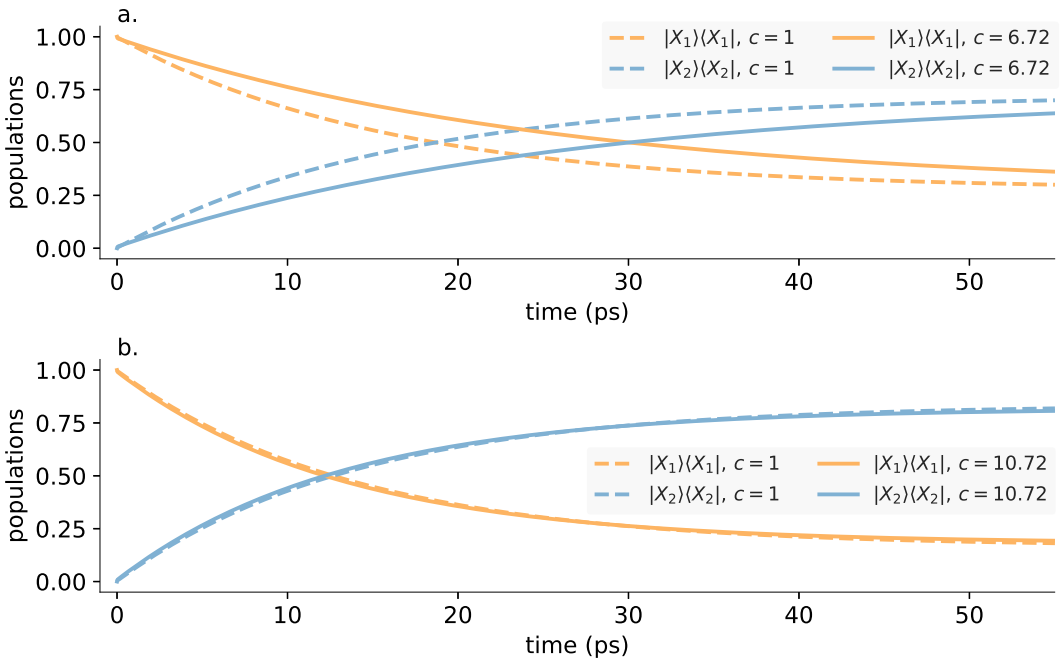

Figure 5.3: Population dynamics for quasi-localised electronic eigenstates. The delocalisation parameter is $\eta = 0.05$. (a) Off-resonant eigenstate energy splitting $\Delta E \approx 200\text{cm}^{-1}$. (b) Resonant eigenstate energy splitting $\Delta E \approx 340\text{cm}^{-1}$. HEOM parameters: truncation level $N = 10$ and Markovian truncation included.

the unshifted energy splitting $\Delta\varepsilon$ to maintain the ratio $\kappa = 0.7$.

In Fig. 5.3 (a) the dynamics are shown for an unshifted eigenstate splitting off-resonant with the underdamped mode, $\Delta E \approx 200\text{cm}^{-1}$. and scaling factor $c = 6.72$. On the introduction of this reorganisation energy scaling the effective charge transfer rate is reduced. In this regime of weak electronic coupling and off-resonant mode the charge transfer can be understood in the Marcus type picture [43] since quantum features of the bath contribute very little to the dynamics. In contrast, the dynamics for an eigenstate splitting resonant with the mode $\Delta E \approx 340\text{cm}^{-1}$ are shown in Fig. 5.3 (b) using a scaling factor $c = 10.72$. With a resonant energy gap the effective transfer rate is observed to increase with the reorganisation scaling. The quantised nature of the mode now has an effect on the transfer dynamics causing the Marcus picture to break down. From the interaction Hamiltonian of a dimer asymmetrically coupled to a single mode in Eq. (5.9), we can see that for $\eta = 0.05$ the dominant effect of the relative displacement mode on the electronic system is to cause fluctuations of the eigenstate energy gap.

5.3.2 Delocalised Eigenstates

The dynamics for delocalised electronic eigenstates where $\eta = 1$ are shown in Fig. 5.4. The reorganisation energy scaling is constrained by the condition $\Delta\varepsilon > \lambda(c-1)$ to give a parameter regime similar to that found for charge separation along the P_{D1} pathway [47]. To make a comparison between the resonant and off-resonant case the ratio $\kappa = \frac{\Delta\varepsilon}{\lambda(c-1)} = 1.3$ is fixed. Figure 5.4 (a) shows the dynamics for an off-resonant energy splitting $\Delta E \approx 200\text{cm}^{-1}$. For the reorganisation energy scaling $c = 3.16$ the effective transfer rate increases slightly but the steady state population of the CT state $|X_2\rangle\langle X_2|$ is reduced. For the resonant case $\Delta E \approx 340\text{cm}^{-1}$ in Fig. 5.4 (b) the steady state CT populations are reduced even more than in the off-resonant case. With more delocalisation we can see from Eq. (5.9) that there is now a greater contribution to the dynamics from the off-diagonal coupling between the mode and electronic eigenstates. This is exhibited in the population oscillations present in the dynamics. As we discussed earlier the introduction of $c > 1$ inhibits coherent electron transfer due to the way coherence is shared between the electronic system, the relative displacement mode and the centre of mass mode. However in our more complete numerical model we also have thermal relaxation and dephasing processes that contribute to the dynamics the strength of which are also scaled asymmetrically.

5.4 Controlling the Performance of a Bio-Inspired Photocell

Charge separation in photosynthetic reaction centres has inspired the study of several theoretical photocell models that try to capture some of the features of these systems in order to propose design principles for bio-inspired artificial photocell devices [16, 17, 18, 19, 115]. Most of these models aim to demonstrate an enhancement of the photocell power output in the presence of quantum mechanical effects such as delocalisation or coupling to quantised modes [16, 17, 18, 19]. While most of these photocell models don't explicitly consider properties of charge transfer states, Ref. [19] does investigate the effect of an asymmetric coupling to a shared mode on the photocell performance. The shared mode is an attempt to capture some

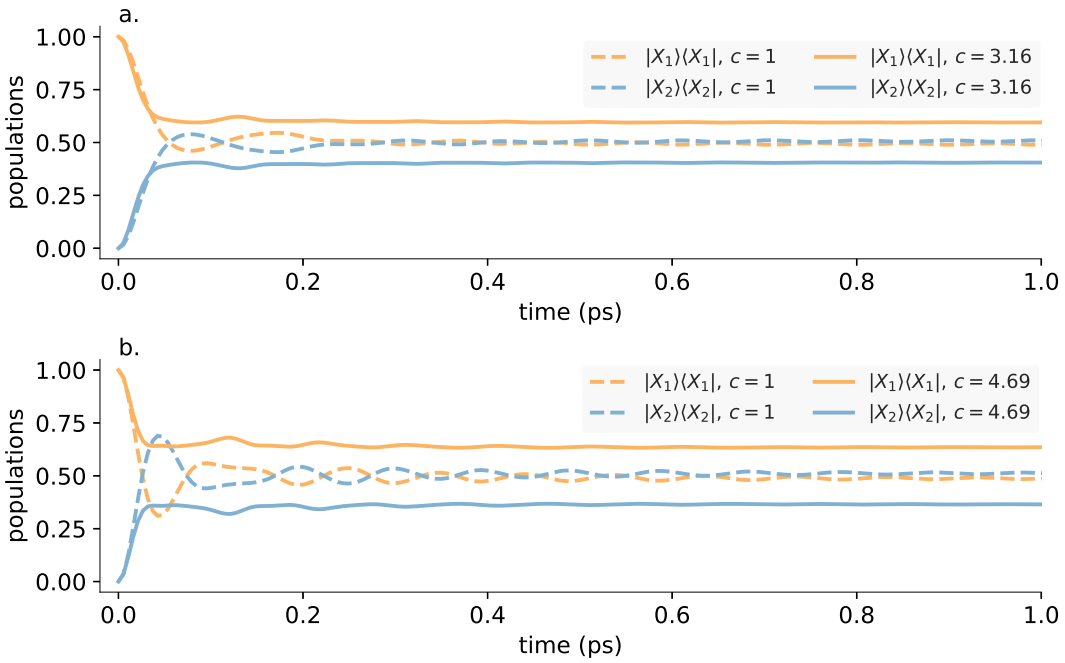

Figure 5.4: Population dynamics for delocalised electronic eigenstates. The delocalisation parameter is $\eta = 1$. (a) Off-resonant eigenstate energy splitting $\Delta E \approx 200\text{cm}^{-1}$. (b) Resonant eigenstate energy splitting $\Delta E \approx 340\text{cm}^{-1}$. HEOM parameters: truncation level $N = 10$ and Markovian truncation included.

correlations of the phonons on the excitation and charge transfer states but it is introduced in a rather ad hoc way. Instead we propose a photocell model in which primary charge separation occurs between an excited state and a CT state coupled to independent phonon baths with asymmetry in the system-bath coupling. The hierarchical equations of motion are used to obtain an exact description of the system-bath interaction in a wide range of parameter regimes. Specifically, we consider the effect of delocalisation and asymmetric reorganisation energy on the current output and current fluctuations using the same spectral density as for the dimer model in the previous section.

A schematic representation of the photocell model is shown in Fig. 5.5. The dimer system used earlier (see Eq. (5.11)) is coupled to a ground state $|g\rangle$ by the electromagnetic field with rate γ_{ex} which excites the eigenstate with greatest amplitude on state $|1\rangle$ (the excitation state). The primary CT state $|2\rangle$ is coupled to a secondary CT state $|\alpha\rangle$ through a phenomenological rate γ_{CT}. Both excitation and secondary charge transfer processes obey detailed balance through contact with thermal baths. Coupling to leads is introduced through the unidirectional rates Γ_R

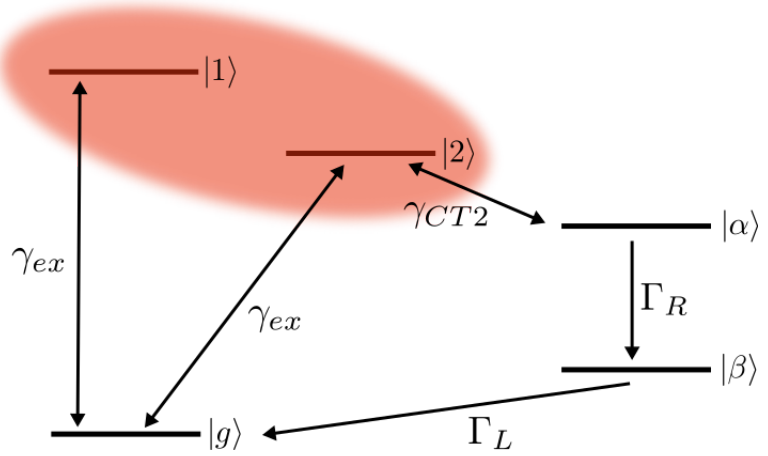

Figure 5.5: Photocell model. Incoherent rates link states as indicated by arrows while the non-perturbative hierarchical equations of motion govern the dissipative coherent dynamics between states $|1\rangle$ and $|2\rangle$.

which connects state $|\alpha\rangle$ with the positively charged 'empty' state of the photocell $|\beta\rangle$, effectively removing an electron from the system, and Γ_L which connects $|\beta\rangle$ to the ground state, emitting an electron into the system. As before the sites $|1\rangle$ and $|2\rangle$ are coupled to independent phonon baths described by the spectral densities Eqs. (5.17) and (5.18) with the reorganisation energy of site $|2\rangle$ (the charge transfer state) scaled by the factor c. The delocalisation of the eigenstates across sites $|1\rangle$ and $|2\rangle$ is quantified by the parameter $\eta = |\frac{2J}{\Delta\varepsilon}|$. The parameters used are shown in Table 5.2.

γ_{ex}	0.001cm^{-1}
n_{ex}	60000
γ_{CT2}	1cm^{-1}
$\Delta\varepsilon_{CT2}$	300cm^{-1}
Γ_L	1cm^{-1}
Γ_R	1cm^{-1}
$\Delta\varepsilon_{\alpha\beta}$	11291.7cm^{-1}
T	$300K$

Table 5.2: Photocell parameters for incoherent transitions.

The current and Fano factor are calculated using a non-perturbative counting statistics method [116] based on the hierarchical equations of motion (see Section

2.1.3). By including a Lindblad dissipator in the diagonal part of the equations of motion for the auxiliary density matrices [83], coupling of the dimer to the rest of the photocell can be described. The counting statistics of the transition between state $|\alpha\rangle$ and the 'empty' state $|\beta\rangle$ is calculated in analogy with the Markovian theory of electron counting statistics (see Section 2.2) but where the operator generating the dynamics of the system is the hierarchy matrix $\mathcal{H}$ containing the coupled equations of motion for the system density matrix and a finite number of auxiliary density matrices depending on the truncation level required for convergence. The jump matrix $\mathcal{H}_J$ describing the tunnelling of an electron from the system to the drain lead consists of the part of the Lindblad dissipator describing this transition in the top level of the hierarchy only. The first and second order cumulants are then

$$\langle\langle I^1\rangle\rangle = \langle\langle\tilde{0}|\mathcal{H}_J|0\rangle\rangle, \tag{5.19}$$

$$\langle\langle I^2\rangle\rangle = \langle\langle\tilde{0}|\mathcal{H}_J - 2\mathcal{H}_J\mathcal{R}\mathcal{H}_J|0\rangle\rangle \tag{5.20}$$

where the first order cumulant corresponds to the mean current and the Fano factor is defined as $F^{(2)}(0) = \frac{\langle\langle I^2\rangle\rangle}{\langle\langle I^1\rangle\rangle}$. The quantities $|0\rangle\rangle$ and $\langle\langle\tilde{0}|$ are the right and left stationary state eigenvectors of the hierarchy matrix and the operator $\mathcal{R} = \mathcal{Q}\mathcal{H}^{-1}\mathcal{Q}$ is the Drazin pseudo-inverse [77]. $\mathcal{Q}$ projects onto the subspace of the hierarchy matrix not spanned by the stationary state eigenvectors. We calculate the current-voltage and $F^{(2)}$-voltage curves by imagining the current between the system and drain lead passing across a hypothetical load connecting states $|\alpha\rangle$ and $|\beta\rangle$. The voltage across the load can be calculated using $eV = \Delta\varepsilon_{\alpha\beta} + k_B T \ln\frac{\rho_{\alpha\alpha}}{\rho_{\beta\beta}}$ [16, 17] where $\Delta\varepsilon_{\alpha\beta}$ is the energy gap between states $|\alpha\rangle$ and $|\beta\rangle$ and the $\rho_{\alpha\alpha(\beta\beta)}$ is the stationary state population of state $|\alpha\rangle$ ($|\beta\rangle$).

5.4.1 Optimising Photocell Performance

The output current of the photocell as a function of the delocalisation parameter η and the scaling factor c is shown in Fig. 5.6 at a fixed voltage of 1.1V. Figure 5.6 (a) shows the photocell current for an unshifted eigenstate energy splitting $\Delta E =$

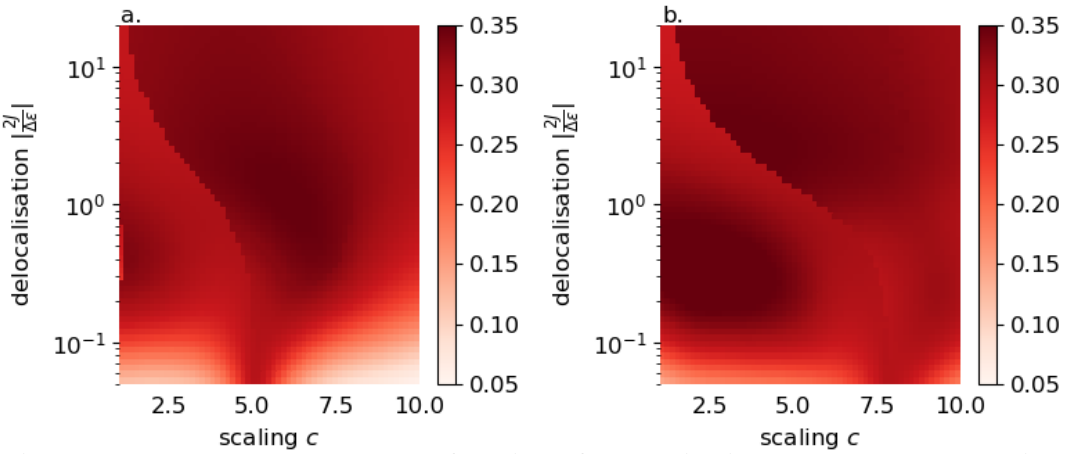

Figure 5.6: Photocell current as a function of delocalisation parameter and scaling asymmetry. The voltage is fixed at a value $1.1V$. (a) The energy splitting in the eigenstate basis $\Delta E \approx 200\text{cm}^{-1}$ is off-resonant with the mode. (b) The energy splitting in the eigenstate basis $\Delta E \approx 340\text{cm}^{-1}$ is resonant with the mode. HEOM parameters: truncation level $N = 5$ and Markovian truncation.

200cm^{-1}, which is off-resonant with the underdamped mode, while the current for a resonant unshifted energy gap $\Delta E = 340\text{cm}^{-1}$ is shown in Fig. 5.6 (b). The rich behaviour of the photocell is evident with several peaks in the current. The features are very similar for eigenstate energy splittings both off-resonant and resonant with the mode. We will discuss the general trends for both resonance conditions below.

For localised eigenstates ($\eta \ll 1$) we can see a low current output of the photocell inhibited by the small electronic coupling between sites $|1\rangle$ and $|2\rangle$. There is however a peak in the current at $c \approx 5$ for the off-resonant case and $c \approx 8$ for the resonant case. This is due to the relative shift of electronic energy levels as c is varied. The values of c at these peaks correspond with the resonance condition of the shifted eigenstate energies at which electron transfer is enhanced.

For intermediate delocalised eigenstates ($\eta \approx 1$) the current is high for $c = 1$ then there is an initial reduction in the current as the reorganisation energy scaling increases. This is due to the onset of the coherent interaction with the centre of mass mode inhibiting coherent electronic transfer. As the scaling increases further, the current peaks again before a gradual decline. As in the localised case, this second peak is likely due to the transition to a regime where dissipative processes which localise the system on site $|2\rangle$ become dominant.

Finally, for very delocalised eigenstates ($\eta > 10$) there is a rapid increase in

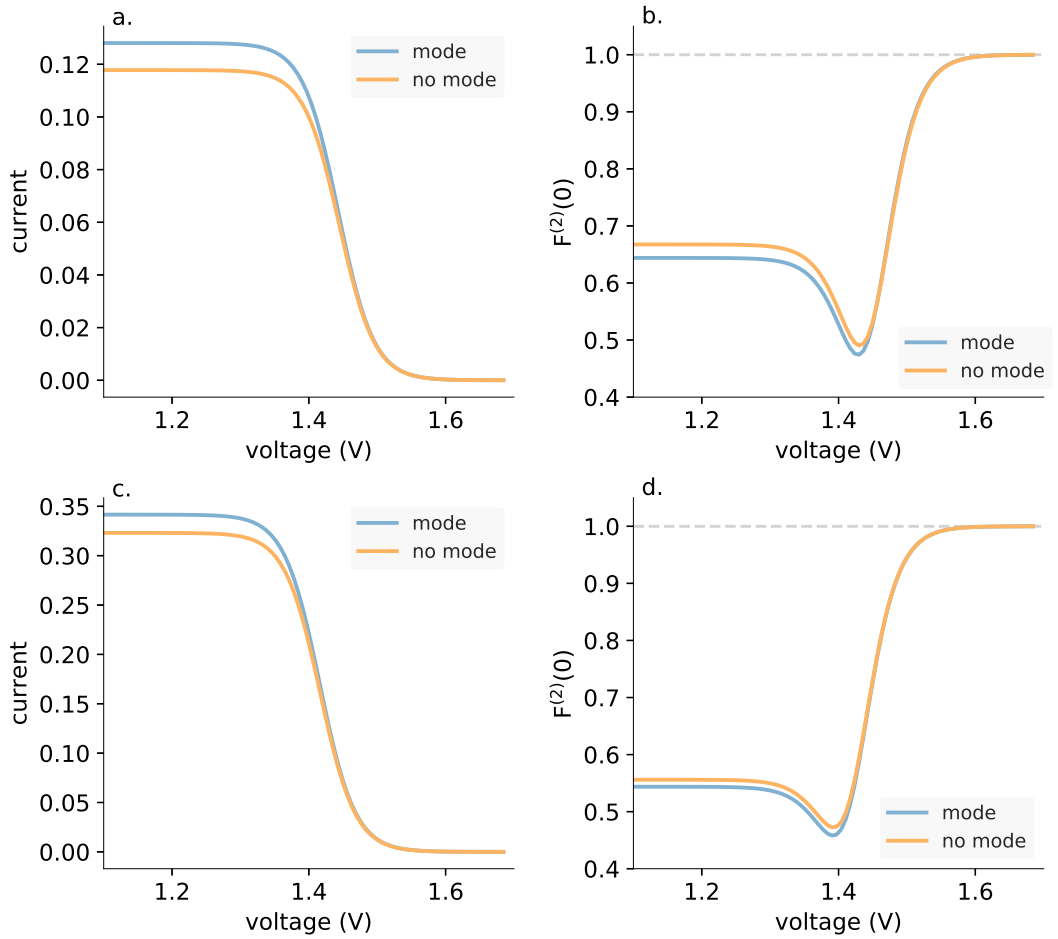

Figure 5.7: Comparing photocell current with and without coupling to an underdamped mode for symmetric site reorganisation energy. (a) Current for delocalisation parameter $\eta = 0.05$, $\Delta E \approx 340\text{cm}^{-1}$ resonant with the mode and reorganisation energy scaling $c = 1$. (b) Fano factor for delocalisation parameter $\eta = 0.05$, $\Delta E \approx 340\text{cm}^{-1}$ resonant with the mode and reorganisation energy scaling $c = 1$. (c) Current for delocalisation parameter $\eta = 1$, $\Delta E \approx 340\text{cm}^{-1}$ resonant with the mode and reorganisation energy scaling $c = 1$. (d) Fano factor for delocalisation parameter $\eta = 1$, $\Delta E \approx 340\text{cm}^{-1}$ resonant with the mode and reorganisation energy scaling $c = 1$. HEOM parameters: truncation level $N = 5$ and Markovian truncation included.

the current as the scaling parameter increases from $c = 1$ to $c = 2.5$. This is due to preferential localisation of the system on site $|2\rangle$ counteracting the reversible coherent transfer between the sites.

5.4.2 Photocell Uncoupled From the Underdamped Mode

We now compare the performance of the photocell with and without coupling to the underdamped mode by considering the spectral densities $J(\omega) = J_D(\omega) + J_M(\omega)$ and $J(\omega) = J_D(\omega)$. We now fix the eigenstate energy gap at $\Delta E \approx 340\text{cm}^{-1}$ which is

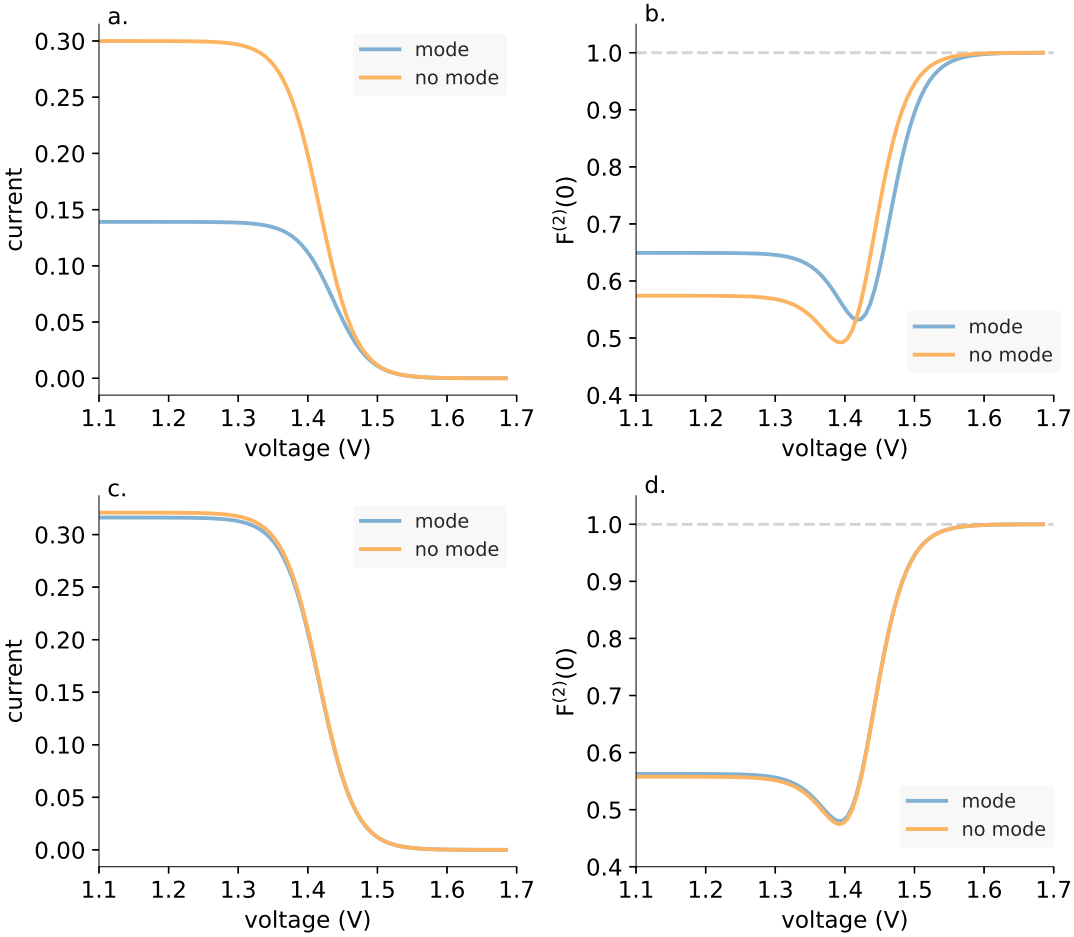

Figure 5.8: Comparing photocell current with and without coupling to an underdamped mode for asymmetric site reorganisation energy. (a) Current for delocalisation parameter $\eta = 0.05$, $\Delta E \approx 340\text{cm}^{-1}$ resonant with the mode and reorganisation energy scaling $c = 10.72$. (b) Fano factor for delocalisation parameter $\eta = 0.05$, $\Delta E \approx 340\text{cm}^{-1}$ resonant with the mode and reorganisation energy scaling $c = 10.72$. (c) Current for delocalisation parameter $\eta = 1$, $\Delta E \approx 340\text{cm}^{-1}$ resonant with the mode and reorganisation energy scaling $c = 4.69$. (d) Fano factor for delocalisation parameter $\eta = 1$, $\Delta E \approx 340\text{cm}^{-1}$ resonant with the mode and reorganisation energy scaling $c = 4.69$. HEOM parameters: truncation level $N = 5$ and Markovian truncation included.

resonant with the underdamped mode. In this parameter regime we would expect the greatest enhancement in the photocell performance due to the mode as it promotes transfer between electronic eigenstates. The current and Fano factor as a function of voltage is shown in Fig. 5.7 for symmetric reorganisation energies ($c = 1$) of sites $|1\rangle$ and $|2\rangle$. The current in the cases of both localised (Fig. 5.7 (a)) and delocalised (Fig. 5.7 (c)) eigenstates shows an increase in the presence of the mode. There is also a corresponding decrease in the Fano factor in both these parameter regimes.

Now looking at the case of asymmetric reorganisation energy of the sites in Fig. 5.8 we see the opposite behaviour. The current for localised eigenstates in Fig. 5.8 (a) shows a significant decrease in the presence of the mode, while for delocalised eigenstates (Fig. 5.8 (c)) the current shows a slight decrease but is largely unaffected by the mode. The Fano factor shows a corresponding increase with the drop in current for the asymmetric reorganisation energy.

The reduction in current is a similar result to that observed in Ref. [115] where the performance of a PSIIRC inspired photocell decreases as more modes are added to the spectral density. While the enhancement of photocell performance due to coupling with a mode has already been shown in Ref. [18] for symmetric coupling, the results presented here emphasise that this is not a general phenomenon. In some cases of asymmetric reorganisation energies, the mode actually reduces the photocell performance. This may be understood by considering the role played by relative displacement and centre of mass modes for $c > 1$. As discussed earlier, asymmetric reorganisation energies lead to coupling between the relative displacement and centre of mass modes, inhibiting coherent transfer between electronic eigenstates. Coupling to a mode also increases the total reorganisation energy of the sites, shifting the site energies into a configuration which may reduce transfer by dissipative processes. For symmetric coupling to a mode it is likely the enhancement due to coherent transfer dominates over the reduction in dissipative transfer after the site energies are shifted. However for asymmetric coupling to the mode, the increase in transfer due to coherence induced by the mode is so slight that it cannot overcome the reduction in transfer due to the increased reorganisation energy shift.

5.5 Summary and Conclusions

In this chapter we investigated the effect of the asymmetry of reorganisation energy between excitation and charge transfer states for charge separation in pigment-protein complexes. First a purely coherent system was considered and the reduction in coherent electronic transfer with reorganisation energy scaling $c > 1$ explained due to the distribution of coherence between the electronic system, relative displace-

ment and centre of mass modes. The dynamics of a dimer system was then studied using parameter regimes inspired by the charge separation pathways in the photosystem II reaction centre. Finally we looked at the performance of a bio-inspired photocell where we varied the delocalisation and the reorganisation energy scaling of the central dimer of chromophores across which primary charge separation occurs. We also demonstrated the enhancement in performance of the photocell when the electronic system was uncoupled from the underdamped mode in the case of asymmetric reorganisation energy.

In terms of the prospects for experimental investigation of these theoretical results, recent advances in the design of artificial photosynthetic systems may soon make this possible. Techniques such as protein maquettes [106, 111] and DNA origami [112, 113, 114] that allow precise spatial arrangement of chromophores relative to one another may soon lead to the study of simple photocell devices built on principles inspired by Nature. In these systems the delocalisation would be relatively simple to control. The inter-chromophore coupling depending on the relative position and orientation of chromophores due to dipole-dipole interactions. Engineering the reorganisation energy scaling would be a balance between positioning chromophores close enough for wavefunction overlap to allow coupling between excitation and CT states and controlling the separation distance of electron and hole in the CT state where a larger permanent dipole moment increases interaction with the bath.

Chapter 6

Final Remarks and Outlook

In this final chapter, the work presented earlier will be briefly summarised. We will also discuss open questions along with possible avenues for future research.

The theoretical frameworks of open quantum systems and Markovian electron counting statistics were discussed in Chapter 2. The general model used to describe the system-bath interaction was presented and a distinction was made between perturbative and non-perturbative approaches to calculating the open quantum system dynamics. Specific theories used throughout the thesis were presented in more detail. A recursive scheme was also presented to obtain the full counting statistics of electron transport through a mesoscopic system . This approach relied on the assumption of Markovian leads weakly coupled to the system.

In the Chapter 3 this Markovian theory of electron counting statistics was applied to a double quantum dot. Super-Poissonian statistics was shown to be a signature of quantum coherence appearing in the current fluctuations. This prepared the way for an extension of the Markovian theory with a new non-perturbative method for the calculation of the current statistics. This was achieved by incorporating the hierarchical equations of motion with a recursive scheme to generate the current cumulants. This method was then applied to study the statistics of the current passing through a dimer molecule. For coupling to a low frequency Drude bath, the non-perturbative method was compared with a perturbative approach with respect to the system-bath coupling. Further work would involve comparison with a theory using a perturbative expansion with respect to the inter-molecule electronic coupling such

as the polaron transformation [85, 74]. It may also be worthwhile to compare the theory with other non-Markovian results [66, 67]. The current statistics for a dimer coupled to an underdamped Brownian oscillator were also compared with a coherent mode model. An extension to the method itself may be to calculate the finite-frequency counting statistics [69, 33]. Analytically this would be straightforward but the main challenge would be from the numerical side. The frequency dependent pseudo-inverse may be difficult to calculate using the sparse data structures required to deal with the large memory overhead of the numerical implementation.

This non-perturbative counting statistics method was applied to a photocell model based on the photosystem II reaction centre (PSIIRC) in Chapter 4. The mean current and current fluctuations were studied while comparing different vibrational environments of the chromophores. Since the hierarchical equations of motion become computationally intractable for even moderately sized systems, a model incorporating modified Redfield rates in a set of Pauli rate equations was presented to look at the effect of the full spectral density on the current statistics. It was found that for experimentally determined PSIIRC parameters, the output current will reduce as the reorganisation energy increases due to coupling with more discrete vibrational modes. The key feature of the system that leads to the reduction in current is the asymmetry in the reorganisation energy between excitation and charge transfer states. This behaviour occurred with a related reduction in the Fano factor. While the current fluctuations are a useful quantity to measure in terms of characterising the device performance, they are difficult to interpret for a complex system such as the PSIIRC photocell. It is not entirely clear how the Fano factor relates to the electronic system structure or the vibrational interaction. However it may be possible to gain a more quantitative understanding of these relationships using tools from graph theory. For a system described by a set of Pauli rate equations, the stochastic matrix generating the time dynamics is equivalent to the negative of the Laplacian for a weighted directed graph [117]. Since there are certain relationships between a graph's structure and the coefficents of the characteristic polynomial of its Laplacian [118] and the Fano factor for Markovian dynamics can also be

derived from the characteristic polynomial of the Liouvillian [68], it is possible a link could be drawn between the two.

Finally in Chapter 5 the effect of reorganisation energy asymmetry on electron transfer was investigated through the dynamics of a simple dimer system as well as through the performance of a prototype photocell. The reduction in coherent electron transfer when the reorganisation energy becomes asymmetric was demonstrated in a coherent model. This is explained due to the distribution of coherence between the electronic system, relative displacement and centre of mass modes. The dynamics of a dimer system was also studied using parameter regimes inspired by the two charge separation pathways in the photosystem II reaction centre. Finally, we looked at the performance of a bio-inspired photocell and demonstrated the increase in performance when the electronic system was uncoupled from the underdamped mode and the coupling to the phonon bath was asymmetric.

Appendix A

PSIIRC Photocell Parameters

The following tables show the parameters used in the PSIIRC photocell model in Chapter 4. The chromophore excitation energies in Table A.1 and the inter-site couplings in Table A.2 are taken from Ref. [47], while the mode couplings in Table A.3 are taken from Refs. [94, 46].

g	P_{D1}	P_{D2}	Chl_{D1}	Chl_{D2}	Phe_{D1}	Phe_{D2}	$Chl^{+}_{D1}Phe^{-}_{D1}$	$P^{+}_{D1}Phe^{-}_{D1}$	β
0	14720	14650	14460	14560	14490	14480	14372	13972	2681

Table A.1: State energies in wavenumbers for PSIIRC photocell, reorganisation energy is not included.

	P_{D1}	P_{D2}	Chl_{D1}	Chl_{D2}	Phe_{D1}	Phe_{D2}	$Chl^{+}_{D1}Phe^{-}_{D1}$	$P^{+}_{D1}Phe^{-}_{D1}$
P_{D1}	-	150	-42	-55	-6	17	0	0
P_{D2}		-	-56	-36	20	-2	0	0
Chl_{D1}			-	7	46	-4	70	0
Chl_{D2}				-	-5	37	0	0
Phe_{D1}					-	-3	70	0
Phe_{D2}						-	0	0
$Chl^{+}_{D1}Phe^{-}_{D1}$							-	40
$P^{+}_{D1}Phe^{-}_{D1}$								-

Table A.2: Electronic couplings between PSIIRC core chromphores and CT states in wavenumbers.

ω_j	s_j	ω_j	s_j	ω_j	s_j	ω_j	s_j
97	0.0371	604	0.0034	1143	0.0303	1354	0.0057
138	0.0455	700	0.005	1181	0.0179	1382	0.0067
213	0.0606	722	0.0074	1190	0.0084	1439	0.0067
260	0.0539	742	0.0269	1208	0.0121	1487	0.0074
298	0.0488	752	0.0219	1216	0.0111	1524	0.0067
342	0.0438	795	0.0077	1235	0.0034	1537	0.0222
388	0.0202	916	0.0286	1252	0.0051	1553	0.0091
425	0.0168	986	0.0162	1260	0.0064	1573	0.0044
518	0.0303	995	0.0293	1286	0.0047	1580	0.0044
546	0.0030	1052	0.0131	1304	0.0057	1612	0.0044
573	0.0094	1069	0.0064	1322	0.0202	1645	0.0034
585	0.0034	1110	0.0192	1338	0.0037	1673	0.001

Table A.3: Frequencies (cm^{-1}) and Huang-Rhys factors for 48 modes of PSIIRC.

Appendix B

Numerical Implementation of Non-Perturbative Counting Statistics Method

Calculation of the mean current and current noise for the hierarchical equations of motion is carried out using Eqs. (3.14) and (3.15), which are shown again here for clarity

$$\langle\langle I^1 \rangle\rangle = \langle\langle \tilde{0}|\mathcal{H}_J|0\rangle\rangle \tag{B.1}$$

$$\langle\langle I^2 \rangle\rangle = \langle\langle \tilde{0}|\mathcal{H}_J - 2\mathcal{H}_J\mathcal{R}\mathcal{H}_J|0\rangle\rangle \tag{B.2}$$

The quantities $|0\rangle\rangle$ and $\langle\langle\tilde{0}|$ are the right and left stationary states eigenvectors of the hierarchy matrix $\mathcal{H}$ respectively. $\mathcal{H}_J$ is the jump operator describing the tunnelling of an electron between the system and the drain lead while $\mathcal{R}$ is the pseudo-inverse of $\mathcal{H}$.

The form of the equations shown above allows efficient calculation of the cumulants using matrix multiplication operations rather than the numerical differentiation method which can be unstable. In general $\mathcal{H}$ is an extremely large matrix so we use sparse data structures to fit the equations into available memory. However, the cumulants depend on the pseudo-inverse of $\mathcal{H}$ which will most likely be dense and therefore direct calculation of this quantity will be unachievable on most avail-

able modern hardware. To avoid this we use a trick from Baiesi et al [77] which casts the problem of calculating the pseudo-inverse to one of the solution of a set of linear equations. We write the result of applying the pseudo-inverse $\mathcal{R}$ to a vector $|y\rangle$ as

$$|z\rangle = \mathcal{R}|y\rangle \tag{B.3}$$

Using $\mathcal{H}\mathcal{R} = \mathcal{R}\mathcal{H} = \mathcal{Q}$ (where $\mathcal{Q}$ is the operator which projects on to the subspace not spanned by the system steady state) we get

$$\mathcal{H}|z\rangle = \mathcal{Q}|y\rangle \tag{B.4}$$

This equation can then be solved for $|z\rangle$ using standard solvers that come with linear algebra software packages.

The python class for a full counting statistics solver for a large system requiring sparse data structures is shown below. The full package can be found at www.github.com/rstones/counting_statistics.

```
import numpy as np
import scipy.sparse as sp
import scipy.sparse.linalg as spla

class FCSSolver(object):

    def __init__(self, H, HJ, pops):
        '''Instantiate an FCSSolver object.

        Arguments:
        H -- time-local generator of system dynamics.
        HJ -- jump operator.
        pops -- vector containing 1's in elements corresponding
        to populations.'''
        if not sp.issparse(H) or not sp.issparse(HJ):
            raise ValueError("This is the sparse package so " \
            "pass me some sparse matrices!")
        self.H = H
```

```
19          self.HJ = HJ
20          self.pops = pops
21
22          self.__watch_variables = ['H', 'HJ', 'pops']
23          self.__cache_is_stale = True
24
25      def __setattr__(self, name, value):
26          '''Overridden to watch selected variables which trigger
27          a cache refresh when they change.'''
28          try:
29              if name in self.__watch_variables:
30                  self.__cache_is_stale = True
31          except AttributeError:
32              pass
33          object.__setattr__(self, name, value)
34
35      def refresh_cache(self):
36          '''Refresh necessary quantities for counting statistics
37          calculations.'''
38          self.ss = self.stationary_state(self.H, self.pops)
39          self.__cache_is_stale = False
40
41      @staticmethod
42      def stationary_state(H, pops):
43          '''Calculate the stationary state.'''
44          ss = spla.eigs(H.tocsc(), k=1, sigma=None, which='SM', \
45          v0=pops/np.sum(pops))[1]
46          return ss / pops.dot(ss)
47
48      def mean(self):
49          '''Calculate the mean.'''
50          if self.__cache_is_stale:
51              self.refresh_cache()
52          return np.real(self.pops.dot(self.jump_op.dot(self.ss)))
53
54      @staticmethod
55      def pseudoinverse(H, Q, y):
```

```
56          '''Effective calculation of pseudoinverse without need
57          for direct calculation.
58
59          Arguments:
60          H -- time-local generator of system dynamics.
61          Q -- operator projecting onto space orthogonal to steady
62          state.
63          y -- vector or matrix being operated on by pseudoinverse.'''
64          result = spla.lgmres(H, Q.dot(y), tol=1.e-5, maxiter=10000)
65          return result[0]
66
67      @staticmethod
68      def Q(H, steady_state, pops):
69          '''Generate the operator projecting onto the system subspace
70          not spanned by the steady state.
71
72          Arguments:
73          H -- time-local generator of system dynamics
74          steady_state -- stationary state of H
75          pops -- vector containing 1's in elements corresponding
76          to populations.'''
77          return sp.eye(H.shape[0]) \
78                  - sp.csr_matrix(steady_state) * sp.csr_matrix(pops.T)
79
80      def zero_frequency_noise(self):
81          '''Calculate the current noise.'''
82          if self.__cache_is_stale:
83              self.refresh_cache()
84          Q = self.Q(self.H, self.ss, self.pops)
85          noise = self.pops.dot(self.jump_op.dot(self.ss)) \
86                  -2.*self.pops.dot(self.jump_op.dot(\
87                      self.pseudoinverse(self.L, Q, self.jump_op.dot(self.ss))))
88          return np.real(noise)
89
90      def second_order_fano_factor(self):
91          '''Calculate the second order Fano factor.'''
92          return self.zero_frequency_noise() / self.mean()
```

Bibliography

[1] R. Blankenship. *Molecular Mechanisms of Photosynthesis*. Wiley-Blackwell, 2001.

[2] G.S. Engel, T.R. Calhoun, E.L. Read, T. Ahn, T. Mancal, Y. Cheng, R.E. Blankenship, and G.R. Fleming. Evidence for wavelike energy transfer through quantum coherence in photosynthetic systems. *Nature*, 446(7137):782–6, 2007.

[3] G. Panitchayangkoon, D. Hayes, K.A. Fransted, J.R. Caram, E. Harel, and J. Wen. Long-lived quantum coherence in photosynthetic complexes at physiological temperature. *Proceedings of the National Academy of Sciences of the United States of America*, 107(29):12766–12770, 2010.

[4] E. Collini, C.Y. Wong, K.E. Wilk, P.M.G. Curmi, P. Brumer, and G.D. Scholes. Coherently wired light-harvesting in photosynthetic marine algae at ambient temperature. *Nature*, 463(7281):644–647, 2010.

[5] C.Y. Wong, R.M. Alvey, D.B. Turner, K.E. Wilk, D.A. Bryant, P.M.G. Curmi, R.J. Silbey, and G.D. Scholes. Electronic coherence lineshapes reveal hidden excitonic correlations in photosynthetic light harvesting. *Nature Chemistry*, 4:396–404, 2012.

[6] F. Fassioli, R. Dinshaw, P.C. Arpin, and G.D. Scholes. Photosynthetic light harvesting: excitons and coherence. *Journal of the Royal Society*, 11(92):20130901, 2014.

[7] E. Romero, R. Augulis, V.I. Novoderezhkin, M. Ferretti, J. Thieme, D. Zigmantas, and R. van Grondelle. Quantum coherence in photosynthesis for efficient solar-energy conversion. *Nature Physics*, 10(9):676–682, 2014.

[8] F.D. Fuller, J. Pan, A. Gelzinis, V. Butkus, S.S. Senlik, D.E. Wilcox, C.F. Yocum, L. Valkunas, D. Abramavicius, and J.P. Ogilvie. Vibronic coherence in oxygenic photosynthesis. *Nature Chemistry*, 6(8):706–711, 2014.

[9] A. Kolli, E.J. O'Reilly, G.D. Scholes, and A. Olaya-Castro. The fundamental role of quantized vibrations in coherent light harvesting by cryptophyte algae. *The Journal of Chemical Physics*, 137(17):174109, 2012.

[10] N. Christensson, H.F. Kauffmann, T. Pullerits, and T. Mančal. Origin of long-lived coherences in light-harvesting complexes. *The Journal of Physical Chemistry B*, 116(25):7449–7454, 2012.

[11] A.W. Chin, J. Prior, R. Rosenbach, F. Caycedo-Soler, S.F. Huelga, and M.B. Plenio. The role of non-equilibrium vibrational structures in electronic coherence and recoherence in pigmentprotein complexes. *Nature Physics*, 9(2):113–118, 2013.

[12] E.J. O'Reilly and A. Olaya-Castro. Non-classicality of the molecular vibrations assisting exciton energy transfer at room temperature. *Nature communications*, 5:3012, 2014.

[13] R. Stones and A. Olaya-Castro. Vibronic Coupling as a Design Principle to Optimize Photosynthetic Energy Transfer. *Chem*, 1(6):822–824, 2016.

[14] J.C. Dean, T. Mirkovic, Z.S.D. Toa, D.G. Oblinsky, and G.D. Scholes. Vibronic Enhancement of Algae Light Harvesting. *Chem*, 1(6):858–872, 2016.

[15] T. Renger. Theory of Optical Spectra Involving Charge Transfer States : Dynamic Localization Predicts a Temperature Dependent Optical Band Shift. *Physical Review Letters*, 93(18), 2004.

[16] K.E. Dorfman, D.V. Voronine, S. Mukamel, and M.O. Scully. Photosynthetic reaction center as a quantum heat engine. *Proceedings of the National Academy of Sciences of the United States of America*, 110(8), 2013.

[17] C. Creatore, M.A. Parker, S. Emmott, and A.W. Chin. Efficient biologically inspired photocell enhanced by delocalized quantum states. *Physical Review Letters*, 111:253601, 2013.

[18] N. Killoran, S. F. Huelga, and M. B. Plenio. Enhancing light-harvesting power with coherent vibrational interactions: A quantum heat engine picture. *Journal of Chemical Physics*, 143(15), 2015.

[19] H. Chen, P. Chiu, and Y. Chen. Vibration-induced coherence enhancement of the performance of a biological quantum heat engine. *Physical Review E*, 94:052101, 2016.

[20] G. Leblanc, E. Gizzie, S. Yang, D.E. Cliffel, and G.K. Jennings. Photosystem I protein films at electrode surfaces for solar energy conversion. *Langmuir*, 30:10990–11001, 2014.

[21] M. Kato, T. Cardona, A.W. Rutherford, and E. Reisner. Photoelectrochemical water oxidation with photosystem II integrated in a mesoporous indium tin oxide electrode. *Journal of American Chemical Society*, 134:8332–8335, 2012.

[22] K. Brinkert, F. Le, X. Li, J. Durrant, A.W. Rutherford, and A. Fantuzzi. Photocurrents from photosystem II in a metal oxide hybrid system : Electron transfer pathways. *Biochimica et Biophysica Acta*, 1857:1497–1505, 2016.

[23] M. Miyachi, S. Ikehira, D. Nishiori, Y. Yamanoi, M. Yamada, M. Iwai, T. Tomo, S.I. Allakhverdiev, and H. Nishihara. Photocurrent generation of reconstituted photosystem II on a self-assembled gold film. *Langmuir*, 33:1351–1358, 2017.

[24] M. Kamran, V.M. Friebe, J.D. Delgado, T.J. Aartsma, R.N. Frese, and M.R. Jones. Demonstration of asymmetric electron conduction in pseudosymmetrical photosynthetic reaction centre proteins in an electrical circuit. *Nature Communications*, 6:1–9, 2015.

[25] I. Lee, J.W. Lee, R.J. Warmack, D.P. Allison, and E. Greenbaum. Molecular electronics of a single photosystem I reaction center: Studies with scanning tunneling microscopy and spectroscopy. *Proceedings of the National Academy of Sciences of the United States of America*, 92:1965–1969, 1995.

[26] D. Gerster, J. Reichert, H. Bi, J.V. Barth, S.M. Kaniber, A.W. Holleitner, I. Visoly-Fisher, S. Sergani, and I. Carmeli. Photocurrent of a single photosynthetic protein. *Nature Nanotechnology*, 7(10):673–6, 2012.

[27] P.B. Lukins and T. Oates. Single-molecule high-resolution structure and electron conduction of photosystem II from scanning tunneling microscopy and spectroscopy. *Biochimica et Biophysica Acta*, 1409:1–11, 1998.

[28] N.J. Tao. Electron transport in molecular junctions. *Nature nanotechnology*, 1(3):173–181, 2006.

[29] Y. Selzer and D.L. Allara. Single-Molecule Electrical Junctions. *Annual Review of Physical Chemistry*, 57(1):593–623, 2006.

[30] L.S. Levitov and G.B. Lesovik. Charge distribution in quantum shot noise. *JETP Letters*, 58(3), 1993.

[31] Y.M. Blanter and M. Büttiker. Shot noise in mesoscopic conductors. *Physics Reports*, 336:1–166, 2000.

[32] D. Bagrets and Y. Nazarov. Full counting statistics of charge transfer in Coulomb blockade systems. *Physical Review B*, 67(8):085316, 2003.

[33] D. Marcos, C. Emary, T. Brandes, and R. Aguado. Finite-frequency counting statistics of electron transport : Markovian theory. *New Journal of Physics*, 12, 2010.

[34] L. Mandel. Fluctuations of photon beams: The distribution of the photo-electrons. *Proc. Phys. Soc.*, 74(3):233–243, 1959.

[35] C. Flindt, T. Novotný, and A.-P. Jauho. Full counting statistics of nano-electromechanical systems. *Europhysics Letters*, 69(3):475–481, feb 2005.

[36] R. Avriller and A.L. Yeyati. Electron-phonon interaction and full counting statistics in molecular junctions. *Physical Review B*, 80(041309), 2009.

[37] L. Simine and D. Segal. Vibrational cooling , heating , and instability in molecular conducting junctions : full counting statistics analysis. *Phys. Chem. Chem. Phys.*, 14:13820–13834, 2012.

[38] Y. Utsumi, A. Ueda, and A. Aharony. Full-counting statistics for molecular junctions : Fluctuation theorem and singularities. *Physical Review B*, 87(115407), 2013.

[39] H.P. Breuer and F. Petruccione. *The Theory of Open Quantum Systems*. Oxford University Press, 2006.

[40] Y. Tanimura. Stochastic Liouville, Langevin, FokkerPlanck, and master equation approaches to quantum dissipative systems. *Journal of the Physical Society of Japan*, 75(8):082001, 2006.

[41] A. Ishizaki and G.R. Fleming. Unified treatment of quantum coherent and incoherent hopping dynamics in electronic energy transfer: reduced hierarchy equation approach. *Journal of Chemical Physics*, 130(23):234111, 2009.

[42] J. Prior, A.W. Chin, S.F. Huelga, and M.B. Plenio. Efficient Simulation of Strong System-Environment Interactions. *Physical Review Letters*, 050404, 2010.

[43] V. May and O. Kuhn. *Charge and Energy Transfer Dynamics in Molecular Systems*. Wiley-VCH, Berlin, 2000.

[44] D. Abramavicius and S. Mukamel. Energy-transfer and charge-separation pathways in the reaction center of photosystem II revealed by coherent two-dimensional optical spectroscopy. *Journal of Chemical Physics*, 133(184501), 2010.

[45] A. Gelzinis, L. Valkunas, F.D. Fuller, J.P. Ogilvie, S. Mukamel, and D. Abramavicius. Tight-binding model of the photosystem II reaction center: application to two-dimensional electronic spectroscopy. *New Journal of Physics*, 15(7):075013, 2013.

[46] V.I. Novoderezhkin, E.G. Andrizhiyevskaya, J.P. Dekker, and R. van Grondelle. Pathways and timescales of primary charge separation in the photosystem II reaction center as revealed by a simultaneous fit of time-resolved fluorescence and transient absorption. *Biophysical Journal*, 89(3):1464–81, 2005.

[47] V.I. Novoderezhkin, E. Romero, J.P. Dekker, and R. van Grondelle. Multiple charge-separation pathways in photosystem II: modeling of transient absorption kinetics. *ChemPhysChem*, 12:681–688, 2011.

[48] A. Nitzan. *Chemical Dynamics in Condensed Phases : Relaxation, Transfer and Reactions in Condensed Molecular Systems: Relaxation, Transfer and Reactions in Condensed Molecular Systems*. Oxford University Press, 2006.

[49] S. Mukamel. *Principles of Nonlinear Optical Spectroscopy*. Oxford University Press, 1995.

[50] W.M. Zhang, T. Meier, V.Y. Chernyak, and S. Mukamel. Exciton-migration and three-pulse femtosecond optical spectroscopies of photosynthetic antenna complexes. *Journal of Chemical Physics*, 108(18):7763 –7775, 1998.

[51] M. Yang and G.R. Fleming. Influence of phonons on exciton transfer dynamics: comparison of the Redfield, Forster and modified Redfield equations. *Chemical Physics*, 275:355–372, 2002.

[52] T. Forster. Delocalized excitation and excitation transfer. In O Sinanoglu, editor, *Part II.B.1 in Modern Quantum Chemistry: Istanbul Lectures. Part III, Action of Light and Organic Crystals*, pages 93–137. Academic Press Inc., New York, 1965.

[53] V.I. Novoderezhkin and R. van Grondelle. Physical origins and models of energy transfer in photosynthetic light-harvesting. *Phys Chem Chem Phys*, 12:7352–7365, 2010.

[54] V. Stehr, R.F. Fink, M. Tafipolski, C. Deibel, and B. Engels. Comparison of different rate constant expressions for the prediction of charge and energy transport in oligoacenes. *Computational Molecular Science*, 6(6), 2016.

[55] J. Strümpfer and K. Schulten. Light harvesting complex II B850 excitation dynamics. *The Journal of chemical physics*, 131(22):225101, 2009.

[56] Q. Shi, L. Chen, G. Nan, R. Xu, and Y. Yan. Electron transfer dynamics: Zusman equation versus exact theory. *Journal of Chemical Physics*, 130(16):164518, 2009.

[57] M. Tanaka and Y. Tanimura. Quantum dissipative dynamics of electron transfer reaction system: Nonperturbative hierarchy equations approach. *Journal of the Physical Society of Japan*, 78(7):073802, 2009.

[58] R.P. Feynman and F.L. Vernon. The theory of a general quantum system interacting with a linear dissipative system. *Annals of Physics*, 24:118–173, 1963.

[59] Y. Tanimura. Reduced hierarchy equations of motion approach with Drude plus Brownian spectral distribution : Probing electron transfer processes by means of two-dimensional correlation spectroscopy. *Journal of Chemical Physics*, 137(22A550), 2012.

[60] Q. Shi, L. Chen, G. Nan, R. Xu, Y. Yan, Q. Shi, G. Nan, R. Xu, and Y Yan. Efficient hierarchical Liouville space propagator to quantum dissipative dynamics. *Journal of Chemical Physics*, 130:084105, 2009.

[61] A. Ishizaki and Y. Tanimura. Quantum dynamics of system strongly coupled to low-temperature colored noise bath: Reduced hierarchy equations approach. *Journal of the Physical Society of Japan*, 74(12):3131–3134, 2005.

[62] G. Kiesslich, E. Schöll, T. Brandes, F. Hohls, and R. Haug. Noise enhancement due to quantum coherence in coupled quantum dots. *Physical Review Letters*, 99(20):206602, 2007.

[63] W. Belzig. Full counting statistics of super-Poissonian shot noise in multilevel quantum dots. *Physical Review B*, 71:161301, 2005.

[64] F. Haupt, F. Cavaliere, R. Fazio, and M. Sassetti. Anomalous suppression of the shot noise in a nanoelectromechanical system. *Physical Review B*, 74:205328, 2006.

[65] H. Carmichael. *An Open Systems Approach to Quantum Optics, Lecture Notes in Physics*. Springer, Berlin, 1991.

[66] C. Flindt, T. Novotný, A. Braggio, M. Sassetti, and A. Jauho. Counting statistics of non-Markovian quantum stochastic processes. *Physical Review Letters*, 100(15):150601, 2008.

[67] C. Flindt, T. Novotný, A. Braggio, and A-P. Jauho. Counting statistics of transport through Coulomb blockade nanostructures: High-order cumulants and non-Markovian effects. *Physical Review B*, 82(15):155407, 2010.

[68] M. Bruderer, L.D. Contreras-Pulido, M. Thaller, L. Sironi, D. Obreschkow, and M.B. Plenio. Inverse counting statistics for stochastic and open quantum systems: the characteristic polynomial approach. *New Journal of Physics*, 16:033030, 2014.

[69] C. Emary, D. Marcos, R. Aguado, and T. Brandes. Frequency-dependent counting statistics in interacting nanoscale conductors. *Physical Review B*, 76(16):161404, 2007.

[70] S. Gustavsson, R. Leturcq, B. Simovic, R. Schleser, T. Ihn, P. Studerus, K. Ensslin, D.C. Driscoll, and A.C. Gossard. Counting statistics of single electron transport in a quantum dot. *Physical Review Letters*, 96:076605, 2006.

[71] F. Hohls, N. Maire, C. Fricke, M.C. Rogge, and R.J. Haug. Shot noise and electron counting measurements on coupled quantum dot. *Journal of Physics: Condensed Matter*, 20:454204, 2008.

[72] C. Fricke, F. Hohls, N. Sethubalasubramanian, L. Fricke, and R.J. Haug. High-order cumulants in the counting statistics of asymmetric quantum dots. *Applied Physics Letters*, 96(202103), 2010.

[73] N. Ubbelohde, C. Fricke, C. Flindt, F. Hohls, and R.J. Haug. Measurement of finite-frequency current statistics in a single-electron transistor. *Nature Communications*, 3:612, 2012.

[74] D.H. Santamore, N. Lambert, and F. Nori. Vibrationally mediated transport in molecular transistors. *Physical Review B*, 87:075422, 2013.

[75] U. Harbola, M. Esposito, and S. Mukamel. Quantum master equation for electron transport through quantum dots and single molecules. *Physical Review B*, 74(23):235309, 2006.

[76] S. Gurvitz and Y. Prager. Microscopic derivation of rate equations for quantum transport. *Physical Review B*, 53(23):15932–15943, 1996.

[77] M. Baiesi, C. Maes, and K. Netocny. Computation of current cumulants for small nonequilibrium systems. *Journal of Statistical Physics*, 135:57–75, 2009.

[78] U. Fano. Ionization yield of radiations. II. The fluctuations of the number of ions. *Physics Reports*, 72(1):26–29, 1947.

[79] C. Emary, C. Pöltl, A. Carmele, J. Kabuss, A. Knorr, and T. Brandes. Bunching and antibunching in electronic transport. *Physical Review B*, 85(16):1–7, 2012.

[80] Z. Li, C. Lam, T. Yu, and J.Q. You. Detector-induced backaction on the counting statistics of a double quantum dot. *Scientific Reports*, 3:3026, 2013.

[81] J. Cerrillo, M. Buser, and T. Brandes. Nonequilibrium quantum transport coefficients and transient dynamics of full counting statistics in the strong-coupling and non-Markovian regimes. *Physical Review B*, 94(214308), 2016.

[82] M. Kindermann and Y.V. Nazarov. Interaction effects on counting statistics and the transmission distribution. *Physical Review Letters*, 91(136802), 2003.

[83] C. Kreisbeck, T. Kramer, M. Rodríguez, and B. Hein. High-performance solution of hierarchical equations of motion for studying energy transfer in light-harvesting complexes. *Journal of Chemical Theory and Computation*, 7(7):2166–2174, 2011.

[84] D. Wang, L. Chen, R. Zheng, L. Wang, and Q. Shi. Communications: A non-perturbative quantum master equation approach to charge carrier transport in organic molecular crystals. *Journal of Chemical Physics*, 132(8):081101, 2010.

[85] T. Brandes. Coherent and collective quantum optical effects in mesoscopic systems. *Physics Reports*, 408(5-6):315–474, 2005.

[86] T. Park and M. Galperin. Self-consistent full counting statistics of inelastic transport. *Physical Review B*, 84(205450), 2011.

[87] E. Romero, I.H.M. van Stokkum, V.I. Novoderezhkin, and J.P. Dekker. Two Different Charge Separation Pathways in Photosystem II. *Biochemistry*, 49:4300–4307, 2010.

[88] R. Emerson and W. Arnold. The photochemical reaction in photosynthesis. *Journal of General Physiology*, 16:191–205, 1932.

[89] R. Emerson and W. Arnold. A separation of the reactions in photosynthesis by means of intermittent light. *Journal of General Physiology*, 15:391–420, 1932.

[90] K. Nishiguchi and A. Fujiwara. Single-electron counting statistics and its circuit application in nanoscale field-effect transistors at room temperature. *Nanotechnology*, 20(175201), 2009.

[91] K. Nishiguchi, Y. Ono, and A. Fujiwara. Single-electron counting statistics of shot noise in nanowire Si metal-oxide- semiconductor field-effect transistors Single-electron counting statistics of shot noise in nanowire Si metal-oxide-semiconductor field-effect transistors. *Applied Physics Letters*, 98(193502), 2011.

[92] B. Loll, J. Kern, W. Saenger, A. Zouni, and J. Biesiadka. Towards complete cofactor arrangement in the 3.0 angstrom resolution structure of photosystem II. *Nature*, 438:1040–1044, 2005.

[93] V.I. Novoderezhkin, A.G. Yakovlev, R. van Grondelle, and V.A. Shuvalov. Coherent Nuclear and Electronic Dynamics in Primary Charge Separation in Photosynthetic Reaction Centers: A Redfield Theory Approach. *The Journal of Physical Chemistry B*, 108(22):7445–7457, 2004.

[94] E.J.G. Peterman, H. van Amerongen, R. van Grondelle, and J.P. Dekker. The nature of the excited state of the reaction center of photosystem II of green plants : A high-resolution fluorescence spectroscopy study. *Proceedings of the National Academy of Sciences of the United States of America*, 95:6128–6133, 1998.

[95] W. Shockley and H.J. Queisser. Detailed balance limit of efficiency of pn junction solar cells. *Journal of Applied Physics*, 32(3):510–519, 1961.

[96] R.T. Ross and M. Calvin. Thermodynamics of light emission and free-energy storage in photosynthesis. *Biophysical Journal*, 7(5):595–614, 1967.

[97] D.M. Coles, Y. Yang, Y. Wang, R.T. Grant, R.A. Taylor, S.K. Saikin, A. Aspuru-Guzik, D.G. Lidzey, J.K. Tang, and J.M. Smith. Strong coupling between chlorosomes of photosynthetic bacteria and a confined optical cavity mode. *Nature Communications*, 5, 2014.

[98] F. Herrera and F.C. Spano. Cavity-controlled chemistry in molecular ensembles. *Physical Review Letters*, 116:238301, 2016.

[99] J.C. Egues, S. Hershfield, and J.W. Wilkins. Zero-frequency shot noise for tunneling through a system with internal scattering. *Physical Review B*, 49(19):517–527, 1994.

[100] A. Braggio, C. Flindt, and T. Novotný. The influence of charge detection on counting statistics. *Journal of Statistical Mechanics*, P01048, 2009.

[101] L.S. Tsimring. Noise in biology. *Reports on Progress in Physics*, 77:026601, 2014.

[102] J.M. Raser and E.K. O'Shea. Noise in gene expression: Origins, consequences and control. *Science*, 309:2010–2013, 2005.

[103] R. Brunetti, F. Affinito, C. Jacoboni, E. Piccinini, and M. Rudan. Shot noise in single open ion channels: A computational approach based on atomistic simulations. *Journal of Computational Electronics*, 6:391–394, 2007.

[104] L. Cardelli, A. Csikász-nagy, N. Dalchau, and M. Tribastone. Noise reduction in complex biological switches. *Scientific Reports*, 6:1–12, 2016.

[105] M. Edelman and A.K. Mattoo. D1-protein dynamics in photosystem II : the lingering enigma. *Photosynthesis Research*, 98:609–620, 2008.

[106] B.R. Lichtenstein, C. Bialas, J.F. Cerda, B.A. Fry, P.L. Dutton, and C.C. Moser. Designing light-activated charge-separating proteins with a naphthoquinone amino acid. *Angew Chem Int Ed English*, 54(46):13626–13629, 2015.

[107] A. Warshel and W.W. Parson. Spectroscopic properties of photosynthetic reaction centers. 1. Theory. *Journal of American Chemical Society*, 109:6143–6152, 1987.

[108] T. Mancal, L. Valkunas, and G.R. Fleming. Theory of exciton charge transfer state coupled systems. *Chemical Physics Letters*, 432:301–305, 2006.

[109] V.I. Novoderezhkin, J.P. Dekker, and R. van Grondelle. Mixing of Exciton and Charge-Transfer States in Photosystem II Reaction Centers: Modeling of Stark Spectra with Modified Redfield Theory. *Biophysical Journal*, 93(4):1293–1311, 2007.

[110] V. Coffman, J. Kundu, and W.K. Wootters. Distributed entanglement. *Physical Review A*, 61:52306, 2000.

[111] G. Kodali, J.A. Mancini, L.A. Solomon, T.V. Episova, N. Roach, C.J. Hobbs, P. Wagner, O.A. Mass, K. Aravindu, J.E. Barnsley, K.C. Gordon, D.L. Officer, P.L. Dutton, and C.C. Moser. Design and engineering of water-soluble light-harvesting protein maquettes. *Chemical Science*, 8:316–324, 2017.

[112] P.W.K. Rothemund. Folding DNA to create nanoscale shapes and patterns. *Nature*, 440:297–302, 2006.

[113] A. Kuzyk, K.T. Laitinen, and P. Torma. DNA origami as a nanoscale template for protein assembly. *Nanotechnology*, 20:235305, 2009.

[114] E.A. Hemmig, C. Creatore, B. Wu, L. Hecker, P. Mair, M.A. Parker, S. Emmott, P. Tinnefeld, U.F. Keyser, and A.W. Chin. Programming Light-Harvesting Efficiency Using DNA Origami. *Nano Letters*, 16:2369–2374, 2016.

[115] R. Stones, H. Hossein-Nejad, R. van Grondelle, and A. Olaya-Castro. On the performance of a photosystem II reaction centre-based photocell. *Chemical Science*, 8:6871–6880, 2017.

[116] R. Stones and A. Olaya-Castro. Non-Perturbative Electron Counting Statistics. *arXiv:1705.02320v2*, 2017.

[117] R. Agaev and P. Chebotarev. On the spectra of nonsymmetric Laplacian matrices. *Linear Algebra and its Applications*, 399:157–168, 2005.

[118] J. Torre-Mayo, M.R. Abril-Raymundo, E. Alarcia-Estévez, C. Marijuan, and M. Pisonero. The nonnegative inverse eigenvalue problem from the coefficients of the characteristic polynomial. EBL digraphs. *Linear Algebra and its Applications*, 426:729–773, 2007.